Synthesis and Characterization of Perovskite Structured Mixed Oxide Compounds

THESIS

Submitted to

Saurashtra University, Rajkot, India

For the Degree of

Doctor of Philosophy

in Science

in the subject of Physics

By

Jaysukh Hansarajbhai Markna

Under the supervision of

Dr. D. G. Kuberkar
Associate Professor
Department of Physics
Saurashtra University
Rajkot, India

December 2006

This thesis is dedicated to

My beloved Parents and Family

STATEMENT UNDER O. Pd.D. 7 OF THE SAURASHTRA UNIVERSITY

This is certified that the work presented in the thesis is my own work, carried out under the supervision of ***Dr. D. G. Kuberkar*** *and leads to some important contributions in Physics supported by necessary references.*

Jaysukh H. Markna
(Research Scholar)

This is to certify that the work submitted for Ph.D. degree in Physics to Saurashtra University, Rajkot by ***Mr. Jaysukh H. Markna*** *has been the result of more than three years of work under my supervision and is a good contribution in the field of Solid State Physics and Materials Science.*

Dr. D. G. Kuberkar
(Research Guide)
Associate Professor
Department of Physics
Saurashtra University
Rajkot

Acknowledgements

"The morality of art consists in the perfect use of an imperfect medium"

Oscar Wilde.

First and foremost, I wish thank my Ph.D supervisor Dr. Deelip G. Kuberkar, for giving me the opportunity to work under his guidance on interesting and fascinating subject of the manganites and for showing me that, research is a privilege, which deserves passion and devotion. My intellectual debt to him goes beyond the physics, I have learned from him.

I am deeply grateful to Prof. S.K. Malik, TIFR, Mumbai for his precious guidance for explaining to me about the subject and fruitful advice. He has provided me an opportunity to work in his laboratory of Magnetism. I fall short of words to express my gratitude to him. I also acknowledge the help extended by other colleagues, Dr. R. Nirmala and Mr. D. Budhikot of the same lab and also Mr. Nilesh Kulkarni during the course of this work

I am thankful to Dr. Pratap Raychaudhuri, TIFR, Mumbai for many useful discussions and allowing me to use his PLD set up at TIFR. I also extend my heartfelt thanks to Mr. J. John and Mr. Vivas for their help in thin films deposition and other related experiments.

I would also like to thank Dr. L. M. Kukreja, RRCAT, Indore for his interest in my work and encouragement. Many thanks also to Dr. B.N. Singh and Mr. Pankaj Misra of CAT for helping me in the thin film deposition and discussions related to PLD technique.

Thanks to Dr. Ravi Kumar, IUAC, New Delhi for extending the SHI facility at IUAC, New Delhi. It has been a nice experience to visit his laboratory for a couple of times and get useful suggestions. Also I would like to thank to Dr. Ram J. Choudhary and Dr. Anjana Dogra for the help during the SHI irradiation experiments.

I am thankful to Dr. V. Ganesan, UGC-DAE CSR Indore for AFM measurements in his Lab.

I would like to thank, Dr. J. A. Bhalodia and Dr. Nikesh Shah for the moral support during this work.

I thank to Mr. Rajesh Desai and Mr. M.J. Meghpara for the administrative and technical help during the course of my doctoral work.

I am thankful to the Prof & Head of Physics Department and teaching faculty members of the department who have helped me in learning Physics.

My sincere thanks are due for senior colleagues and friends Dr. Chetan M. Thaker, Dr. S. Rayaprol, Dr. Krushna Mavani and Dr. Dhanvir Rana for their help during the course of this work. I also thank my lab.friends Ms. Rohini Parmar, Mr. Prashant, Mr. Piyush, Ms. Rujuta, Mr. Dalsania and Mr. Dhiren Pandya for their friendly cooperation and help in this endeavor.

It is a moment to remember my friends Mr. Atul, Mr. Chetan, Mr. Vinay, Mr. Narendra, Dr. Samip, Mr. Nilesh and Mr. Shailesh for providing a friendly and relaxing environment during my stay at Rajkot.

Thanks to Mrs. Preeti D. Kuberkar and Ms. Madhura D. Kuberkar for a nice hospitality and homely treatment during the course of this work.

I thank my father- and mother-in-law Shri. S. G. Nandaniya and Smt. Parvatiben Nandaniya and brother-in-law Mr. Darmesh for their moral support during the course of work.

It is a great moment to remember my family for their unrelenting efforts for my education since my childhood. My father Shri. Hansarajbhai H. Markna and Mother Smt. Leeben H. Markna have always supported endlessly for my higher education. I am indebted to my parents for their unquestioning support and love. It is time to acknowledge My brother Mr. Rajnit H. Markna, who has edify me many real life aspects. .

Finally, I would like to thank my wife, Mrs. Kajal J. Markna for her endless love and support.

December, 2006 **Jaysukh H. Markna**

Rajkot

I thankfully acknowledge **Department of Atomic Energy- Board of Research in Nuclear Sciences (DAE-BRNS), Mumbai,** India for providing me financial assistance as Junior Research Fellow (JRF) during July 2004 – March 2007 under the Major Research Project (MRP) No. 2003/34/20/BRNS/1944 of **Dr. D.G. Kuberkar**.

December, 2006 **Jaysukh H. Markna**

Preface

The discovery of high-temperature superconductivity in cuprates has strongly renewed the interest in manganite which exhibit the field dependent resistivity knows as the magnetoresistance. These materials display a wide variety of magnetic phases arising from structural, spin, orbital and charge correlation, which attract scientific community for basic research purposes. Further, mixed valent manganites exhibiting colossal magnetoresistance are potential candidates for technological applications such as magnetic memory devices, bolometers, electric field switches, etc. For that, it is necessary to master the growth of high quality thin films with the well controlled tailored properties. In the present investigation, studies on manganite thin films and heterostructures shows that, these materials have potential in applications in the field and temperature sensors and as well as they exhibit interesting phenomenon from basic physics point of view. Various types of structural, electronic and magnetic investigations have been made on the bulk and thin film samples in order to understand various mechanisms and properties. The unique contribution of this work is devoted to the thickness dependent irradiation effect on the thin films and to know, how controlled defect tailors the physical properties of these films. All the bulk materials in the present work were synthesized using solid state reaction route at Department of Physics, Saurashtra University, Rajkot, India. Thin films and heterostructures were deposited using the Pulsed Laser Deposition technique. Most of the experimental work has been performed in collaboration with Tata Institute of Fundamental Research (TIFR), Mumbai, Raja Ramana Centre for Advance Technology (RRCAT), Indore and Inter-University Accelerate Centre (IUAC), New Delhi, India.

Index

Chapter – 1

Chapter – 2

Chapter – 3

Studies on $La_{0.5}Pr_{0.2}Sr_{0.3}MnO_3$ (LPSMO)/LAO, STO manganites

Chapter – 4

Thickness dependent irradiation studies on $La_{0.5}Pr_{0.2}Ba_{0.3}MnO_3$ (LPBMO) films on the $LaAlO_3$ substrate.

Chapter – 5

Chapter - 1

1.1 Introduction to manganites: CMR behavior in bulk and thin films

The last decade has experienced the emergence of mixed oxide materials as one of the most attractive research subjects for the condensed matter physicists. The research on these materials was initially stimulated by the discovery of high-temperature superconductivity (HTSC) in the late eighties which provided the platform for rethinking about the use of mixed oxides for variety of applications involving many interesting properties exhibited by them. Amongst several mixed oxide compounds studied so far, the mixed valence perovskite manganites, $Re_{1-x}A_xMnO_3$ (where Re= rare earth, A= alkaline earth) provide a unique opportunity to study the structure-property correlation due to the interplay among change carriers, magnetic coupling, orbital ordering and structural distortion.

The manganites are interesting compounds having exciting properties from both the basic research as well as from technological point of view. As the technology pursued with this material requires film growth, extensive studies have been made on material synthesis, structural and physical characterization and device fabrication.

The mixed valent manganese oxides possess rich and complex physics related to the importance of electron-lattice and electron-electron interactions. The structural, magnetic and transport properties of these compounds are intricately related. In addition, the Colossal Magneto Resistance (CMR) effect exhibited by manganites and the occurrence of metallic phases with a fully spin-polarized conduction band are promising for potential applications. Various technologically important applications of manganites require their high quality thin films having well-controlled & tailored properties. Progress in the growth of epitaxial thin films opens a way to all oxide or oxide-metal devices.

1.1. CMR (colossal magnetoresistance) materials

1.1.1 Physics of the CMR materials

MR phenomenon

Magnetoresistance (MR) is the change in electrical resistance of material on application of external magnetic filed. It is defined as

$$MR(\%) = \frac{\rho_0 - \rho_H}{\rho_0} \times 100$$

where ρ_H and ρ_0 are the resistivities at a given temperature in the presence and absence of the magnetic field (H), respectively. MR may be negative or positive depending upon fall or rise in the resistivity, respectively, on the application of magnetic field. The positive MR% is commonly referred as ordinary magnetoresistance (OMR). Classically, the cause of such MR is attributed to the effect of the Lorentz force (due to applied field) on the itinerant electrons causing extra deflection, which increases the resistance. Such type of MR is dependent on the angle between current direction and orientation of magnetization.

The reason for very high negative MR (~50%) in artificially grown multilayers of antiferromagnetically coupled metallic layers of Fe/Cr and Cu/Co by Baibich et al resulted in boosting of the research on synthesizing new materials with higher negative MR having applications in magnetic read heads, bolometer, etc.[1, 2].

Types of the magnetoresistance

Depending on the nature and origin of the MR exhibited by different types of materials, it can be classified as follows

A. Anisotropic Magnetoresistance (AMR)

In this type of magnetoresistance, change in the resistance is related to the variation in the magnetization of the ferromagnetic film. The AMR can be expresses as

$$AMR = \frac{R_{\prod} - R_{\perp}}{R_{\perp}}$$

where, $R_{\prod}$ and $R_{\perp}$ are resistances with the field applied parallel and perpendicular to the sample, respectively. In the case of AMR, the resistance is anisotropic and depends on the orientation of the magnetization with respect to the current. The origin of the AMR effect lies in the spin-orbit coupling and the splitting of the d-bands in ferromagnetic metals.

B. Tunneling Magnetoresistance (TMR)

Tunneling magnetoresistance phenomenon is observed in the tunneling junction of the two ferromagnetic layers which are separated by an insulating barrier.

Similar to other MR effect, in the TMR, considerable change in resistance is observed when the relative orientation of the two magnetic layers changes from anti parallel to parallel. The relative change in the resistance, TMR, is quantified by the equation

$$TMR = \frac{I_P - I_{AP}}{I_{AP}}$$

where, I_P is the current when both the ferromagnetic layers have parallel magnetizations while I_{AP} is the current when one ferromagnetic layer has a parallel magnetization and another layer has anti-parallel magnetization.

C. Giant magnetoresistance (GMR)

Large magnetoresistance, referred to as giant magnetoresistance (GMR), was first observed, on the application of magnetic field to atomically engineered magnetic superlattices. This form of magnetoresistance was observed in metallic multilayers such as Fe/Cr, Co/Cu [1, 3]. The magnetic field enhances the conduction of electrons resulting in MR ~ 50%. Owing to large amount of MR, name giant magnetoresistance was given to emphasize the strength of MR in these materials. In the case of GMR, resistance is dependent on the direction of the magnetization because electrons have different scattering probabilities in the presence of parallel and anti- parallel magnetization directions. The GMR is usually defined as

$$GMR = \frac{R_P - R_{AP}}{R_{AP}}$$

where, R_{AP} and R_P the resistances of the stack of layers with anti-parallel (AP) and parallel (P) state of the magnetizations, respectively.

D. Colossal magnetoresistance (CMR)

Recently, the MR as large as ~100% was observed in manganites. This was an extraordinarily large magnetoresistance as compared to previously observed GMR. Therefore, to emphasize the strength of MR in these compounds, a new term called "colossal magnetoresistance (CMR)" was coined [4]. The origin of MR in manganites is quite different than the origin of other forms of MR discussed above. The CMR is an intrinsic property related to crystal structure and has its origin in the spin disorder of conduction electrons, which can be suppressed by the application of the magnetic field

resulting in large magnetoresistance [4-6]. The CMR can be determined from the ratio of a change in the resistivity under the magnetic field, which is expressed as,

$$CMR = \frac{\rho_0 - \rho_H}{\rho_0} \times 100$$

The discovery of CMR in manganites and its relation to various electronic and magnetic properties rejuvenated the research interest in similar compounds. Since manganites appear promising candidates, both from basic research and applications point of view, a major fraction of materials scientists have contributed to the better understanding of these materials. This thesis is devoted to the understanding of various physical properties of complex manganite systems and some efforts to evaluate the application potentiality of these compounds.

1.1.2 Structural, Electronic transport, Magnetic and Magnetotransport Properties

1.1.2. (A) Crystallographic and Electronic Structure

The structure of the $Re_{1-X}M_XMnO_3$ oxides is close to that of the cubic perovskite (Fig.1.1). The large sized Re-trivalent ions and M-divalent ions occupy the A site with 12 - fold oxygen coordination. The smaller Mn ions in the Mn^{+3} – Mn^{+4} mixed valent state are located at the centre of an oxygen octahedron i.e. at the B-site with 6-fold coordination. For the stoichiometric oxide, the proportions of Mn ions in the +3 & +4 valence states are respectively, 1-x and x.

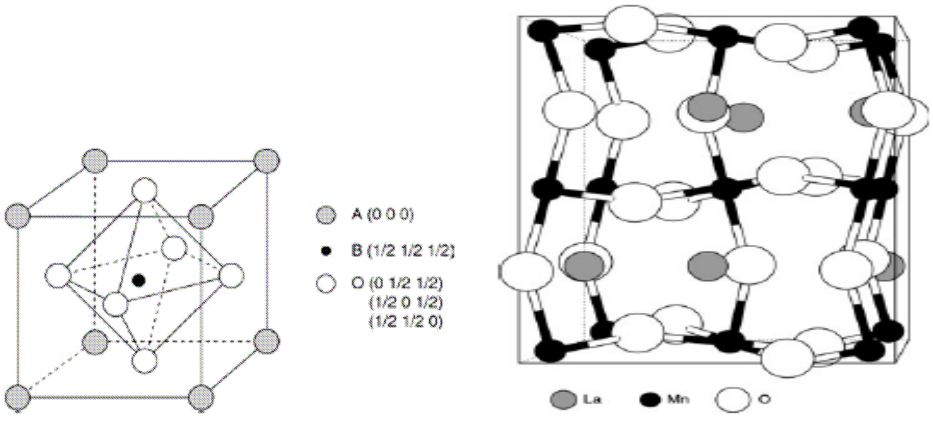

Figure 1.1: Schematic view of the cubic perovskite structure. Crystallographic structure of $LaMnO_3$.

The structure of the manganite is governed by the tolerance factor $t = (r_A + r_O)/\sqrt{2}\,(r_B + r_O)$. The perovskite structure is stable in the range $0.89 < t < 1.02$, $t = 1$ corresponding to the perfect cubic closely packed structure. Generally, t differs appreciably from 1 and the manganites have, at least, at low temperature, a lower rhombohedral symmetry or orthorhombic structure. This is illustrated by the orthorhombic structure of $LaMnO_3$ (Fig. 1.1), which is the parent compound of the most of the manganites studied for potential application by partial substitution of La by Ca and Sr.

For an isolated 3d ion, five degenerate orbital states are available to the 3d electrons with $l = 2$. In a crystal, the degeneracy is partly lifted by the crystal field. The five d-orbitals are split by a cubic crystal field into three t_{2g} orbitals and two e_g orbitals. For the MnO_6 octahedron, the splitting between the lowest t_{2g} level and the highest e_g level is $\Delta \sim 1.5$ eV (Fig.1.2). For the Mn^{3+} and Mn^{4+} ions, the intra-atomic correlations ensure parallel alignment of the electron spins having corresponding exchange energy of about 2.5 eV larger than the crystal field splitting Δ. Mn^{3+} is $3d^4$, $t_{2g}^{3\uparrow}$ $e_g^{\uparrow}$ with S = 2 whereas Mn^{4+} is $3d^3$, $t_{2g}^{3\uparrow}$ with S=3/2. Their respective magnetic moments are $4\mu_B$ and $3\mu_B$, neglecting the small orbital contribution.

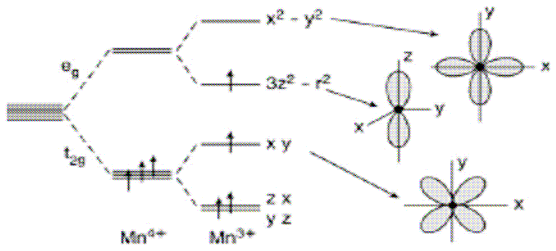

Figure 1.2: Energy levels and orbitals of Mn^{4+} and Mn^{3+} in a crystal field of octahedral symmetry and with axial elongation.

In a crystal field of symmetry lower than cubic, the degeneracy of the e_g and t_{2g} levels is lifted, as shown in the fig.1.2 for an axial elongation of the oxygen octahedron. Although the energy of Mn^{4+} remains unchanged by such a distortion, the energy of Mn^{+3} is lowered. Thus, Mn^{+3} has a marked tendency to distort its octahedral environment in contrast to Mn^{+4}. This Jahn – Teller distortion is rather effective in the lightly doped

manganites; i.e. with a large concentration, 1-x, of Mn^{+3} ions; the Jahn-Teller distortions are not independent from one Mn^{+3} site to another (cooperative Jahn-Teller effect). This is illustrated by the structure of $LaMnO_3$ (Fig.1.1) in which the MnO_6 octahedra are strongly elongated within the ab plane in a regular way leading to a doubling of the unit cell. On increasing the Mn^{+4} content, the Jahn-Teller distortions are reduced and the stabilization of the $3_{z^2-r^2}$ e_g orbital becomes less effective. Nevertheless, in a large number of manganites, the e_g orbitals of two types, $3_{z^2-r^2}$ and x^2-y^2 are not occupied by the e_g electrons of Mn^{3+} at random and an orbital order is achieved.

Double Exchange

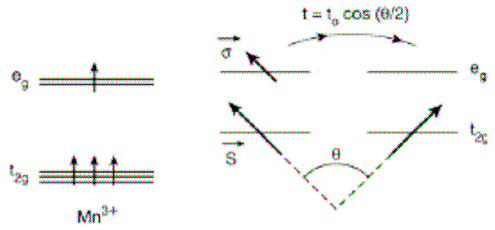

Figure 1.3: Schematic view of the double exchange (DE) mechanism.

A peculiar and interesting case is that of Mn^{+3}-O-Mn^{4+} for which the Mn ions can exchange their valence by a simultaneous jump of the e_g electron of Mn^{+3} on the O p -orbital and from the O p-orbital to the empty e_g orbital of Mn^{+4}. This mechanism of DE originally proposed by Zener ensures a strong ferromagnetic-type interaction [7]. As shown by Anderson and Hasegawa, the probability of the e_g electron transfer from Mn^{3+} to neighboring Mn^{4+} is $t_oCOS(\theta/2)$, θ being the angle between the Mn spins, in the case of strong Hunds coupling (Fig.1.3) [8]. The process of electron transfer lifts the degeneracy of the configurations Mn^{+3} - O - Mn^{+4} and Mn^{4+}- O -Mn^{3+} leading to two energy levels $E_{t=0} \pm t_oCOS(\theta/2)$. The energy gain of the parallel spin configurations to θ = 0, which maximizes *t*, with respect to the anti-parallel one θ =π, reveals the ferromagnetic character of the DE interaction. However in the DE, angular dependence of COS(θ /2) is quite different from COS(θ) of the usual exchange interaction. This different angular dependence in conjunction with the competition between DE ferromgmagnetism and superxchange anti-ferromagnetism is at the origin of the complex magnetic phase diagram of manganites versus the doping level, x. In particular, canted AF phases at small x were predicted early on by P. G. de Gennes [9].

1.1.2. (B) Electronic Transport

The simple manganites, such as $La_{1-X}M_XMnO_3$ (M= Ca, Sr, Ba) with x = 1/3 with strong DE exhibits a transition from high temperature paramagnetic (PM) semi-conducting or insulating (I) phase to a low temperature FM phase.

Paramagnetic region

In the P phase, the electrical resistivity generally exhibits strong temperature dependence. Different $\rho(T)$ laws have been used in fitting experimental data, the most popular ones being: (1) simple thermal activation law $\rho = \rho_\infty \exp(E_0/k_BT)$ with a typical gap value of ~ 0.1 eV (ii) hopping of adiabatic polarons $\rho \sim T \exp(E_0/k_BT)$; (iii) Mott variable range-hopping (VRH), $\rho = \rho_\infty \exp [(T_0/T)^{1/4}]$. Each of these laws have some physical origins, which is respectively (i) the existence of a pseudogap at the Fermi level in the P phase (ii) the local lattice distortion accompanying the moving charge carrier (Jahn-Teller polarons); (iii) the localization of the charge carriers by the magnetic disorder [10]. In a narrow range of temperature, it is practically impossible to discriminate between these different $\rho(T)$ laws.

Ferromagnetic region

At low temperature, the spontaneous alignment of the Mn spins below the Curie temperature, T_C, allows the delocalization of the e_g electrons, leading to a low resistive FM phase with $\rho \approx \rho_0 + aT^2$ for $T \leq T_C$. This alignment of the Mn spins can be induced for $T \geq T_C$, or reinforced for $T \leq T_C$, by applying an external magnetic field. The maximum effect is obtained close to T_C since the initial magnetic susceptibility diverges as $T \rightarrow T_C$. Thus, these manganites have a rather large negative magnetoresistance, the so –called CMR, which peaks at about T_C. This phenomenon is observed in large number of manganites. In general, since the resistivity of the P phase strongly increases on decreasing T, whereas that of the FM phases decreases, the CMR becomes larger as T_C becomes smaller at least for a given doing level.

Effects of doping level and A-site cation size

The physical properties of perovskite-type manganites are determined by two main parameters: the doing level, $x = Mn^{4+}/ (Mn^{3+} + Mn^{4+})$, and the average size of the cation A, $\langle r_A \rangle$. A third relevant parameter is the degree of disorder at site A, defined by

$\sigma^2 = \sum x_i r_i^2 - < r_A >^2$. An enormous number of experimental studies have been performed to quantify these effects [11]. In general, ferromagnetic DE is maximum around x=1/3 and for $<r_A>$ ≈ 1.24 Å. The reduction of $<r_A>$ from this optimum value leads to an increasing distortion of the crystallographic structure. The resulting reduction of the Mn-O-Mn angle from 180º to a smaller value weakens the ferromagnetic DE and increases the tendency to localize the charge carriers. This drastic effect of $<r_A>$ on the resistivity, is exemplified by the phase diagram in fig.1.4 for x=0.3 [12]. Figure 1.4 also shows the phase diagram of two extreme cases of $La_{1-x}Sr_xMnO_3$ which is most FM manganite and $Pr_{1-x}Ca_xMnO_3$ which displays large charge ordering (CO) effects.

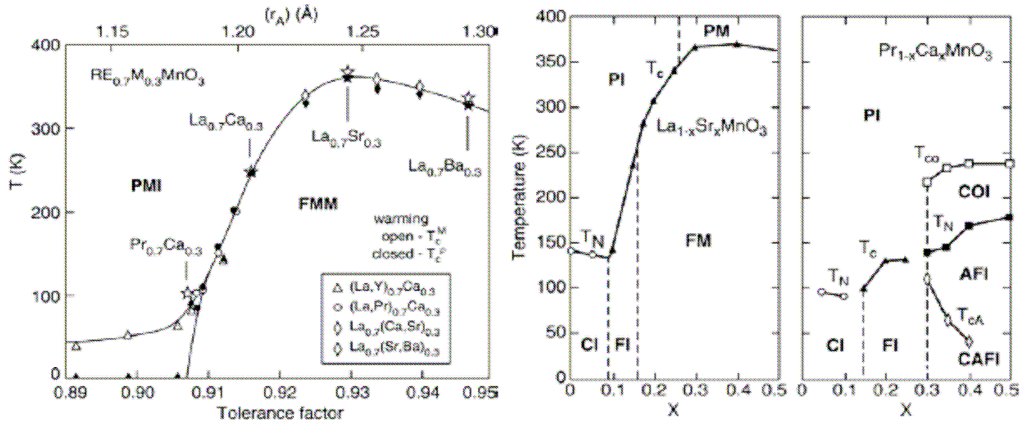

Figure 1.4: Phase diagrams of temperature versus tolerance factor and average radius of cation at A-site for $Re_{0.7}A_{0.3}MnO_3$, single crystal $La_{1-x}Sr_xMnO_3$ and $Pr_{1-x}Ca_xMnO_3$ system. (Reproduced form the refs. 12, 13).

1.1.2. (C) Magnetic properties

The magnetic properties of the manganites are governed by exchange interactions between the Mn ion spins. These interactions are relatively large between two Mn spins separated by an oxygen atom and are controlled by the overlap between the Mn d-orbitals and the O p-orbitals. The corresponding superxchange interaction depends on the orbital configuration following the rules of Goodenough & Kanamori.[6]. Generally, for Mn^{4+}-O-Mn^{3+}, the interaction is AF, whereas Mn^{3+}-O-Mn^{4+}, such as in $LaMnO_3$ where both F and AF interactions coexist [7]. The $LaMnO_3$ end member was found to be antiferromagnetic, with ferromagnetic planes that had alternating directions of magnetization. The other end member $CaMnO_3$ was also found to be antiferromagnetic

with each Mn^{+4} surrounded by the six closest neighbors having opposite spin. Other doping levels gave different types of antiferromagnetic ordering but in the doping range of $x \cong 0.3$, the samples were ferromagnetic. Goodenough has explained the magnetic structures for different doping levels in terms of different types of bonding, where some bonds are ferromagnetic and others are antiferromagnetic or paramagnetic. This is determined by the relative orientation of occupied and unoccupied orbitals of the Mn-O-Mn pairs.

Charge and Orbital Ordering in Manganites

As shown in the fig. 1.4, upon doping, the manganites exhibit a wide verity of ordered states, including ferromagnetic and charge-ordered (CO) phases. In these compounds, there exist orbital degrees of freedom of the e_g electrons in Mn^{3+} ions, and orbital ordering can lower the electronic energy through the Jahn-Teller mechanism. Therefore, charge and orbital-ordering effects are particularly pronounced in mixed valent manganites. Some of the arrangements that have been identified are shown in fig.1.5. At x=0, the A-type spin state is orbitally ordered as it appears in the fig. 1.5 (a). Figure 1.5. (b) shows the related charge and orbital ordering scheme for x=0.5, where there is same amount of Mn^{4+} and Mn^{+3} ions and the charge-exchange (CE) type arrangement is formed. In $La_{1/3}Ca_{2/3}MnO_3$, there are twice as many $Mn^{4+}(3d^3)$ ions as compared to the $Mn^{3+}(3d^4)$ ions and the ordering of the diagonal rows of Mn^{4+} and Mn^{3+} ions plus the orientational ordering of the d_z^2 orbitals in Mn^{3+} gives rise to the stripe pattern as shown in fig.1.5.(c) [14].

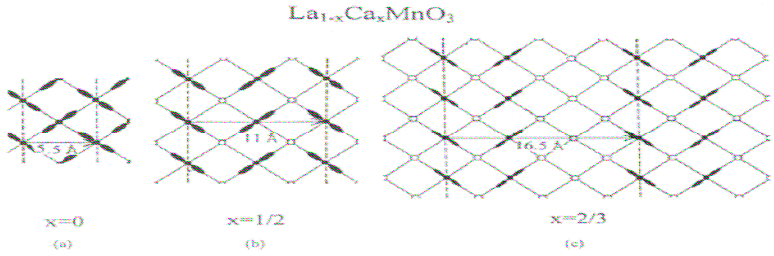

Figure 1. 5 : The charge and orbital ordering configurations in the orthorhombic basal plane for x= 0, ½, 2/3 of $La_{1-x}Ca_xMnO_3$. Open circles are Mn^{4+} and the lobes show the orbital ordering of the e_g electrons of Mn^{3+}

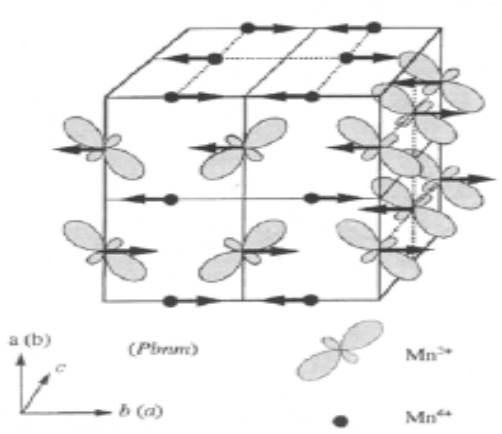

Figure1.6: Spin, charge and orbital ordering pattern of CE antiferromagnetic type Observed for most of the x=1/2 manganites. The e_g orbital ordering on Mn^{3+} sites is also shown. The Mn^{3+} sites are indicated by closed circles.

Several other manganites exhibit CE- type CO-phase at x=0.5 as well. A sketch of the complex orbital, charge and spin order is shown in figure 1.6. While the spins are purely antiferromagnetic, the charge and orbital ordering occurs in alternate b-c planes, giving rise to charge-stack order. This state can be easily destroyed by a magnetic field in a first order transition [15]. Investigations on charge ordering have established the intimate connection of the lattice distortion to CO. It is the lattice distortion associated with orbital ordering that appears to localize the charge and initiate charge ordering. Eventually, the Coulomb interaction wins over the kinetic energy of the electrons to form long range CO state. The scale of the energy involved with CO as measured by the charge-ordering gap is around 0.5-1 eV. This is similar to the unscreened bare nearest neighbor Coulomb repulsion. This is also close to the approximate energy required to create ~ 1 % orthorhombic distortion. It is likely that both the energy scales along with magnetic exchange decides the energy scale of the charge-ordering gap.

Half metallic nature

Half- metallic materials are characterized by the coexistence of metallic behavior for one electron spin and insulating behavior for the other. Thus, the electronic density of states is completely spin polarized at the Fermi level and the conductivity is dominated by these metallic single – spin charge carriers (Fig.1.7). These exotic physical properties could have a significant effect on technological applications related to magnetism and

spin electronics. Some ferromagnetic systems, such as Heusler compounds and chromium metallic exhibits half metallic behaviour [16, 17].

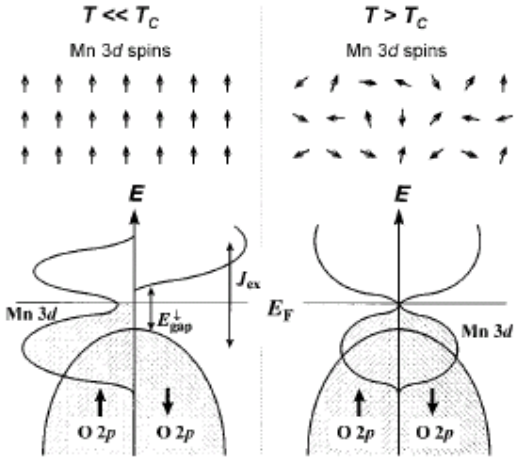

Figure 1.7: Schematic energy diagrams and the Mn 3d spin alignments of the doped manganese perovskite at $T \leq T_C$ and at $T \geq T_C$. J_{ex} is the Hunds rule exchange energy and E_{gap} denotes the insulating band gap of the minority-spin states.

The doped manganese perovskite is mixed-valent with $Mn^{3+}(3d^4)$ and Mn^{4+} $(3d^3)$. For the octahedral site symmetry of the MnO_6 complex, the configuration becomes $t_{2g}^3$for Mn^{3+} and t_{2g}^3 for Mn^{4+}. In the double-exchange mechanism, the e_g electrons are considered as mobile charge carriers interacting with the localized Mn^{4+} (S=3/2) spins. The carriers with hopping avoid the strong on site Hund`s exchange energy J_{ex} when the Mn spin are aligned ferromagnetically. J_{ex} (~2.5 eV) is much larger than the e_g band width (~1 eV). Thus the conduction electrons are expected to be highly spin polarized, and the possibility of 100% spin polarization (that is half-metallic state) occurs [18].

1.1.2. (D) Magneto transport Properties

High Field Magnetoresistance (HFMR)

In the ferromagnetic region, manganite sample shows metallic behaviour, i.e. a positive temperature coefficient of the resistivity. Near the ferromagnetic transition, spin disorder leads to a sharp increase in the resistivity. The application of an external magnetic field results in to decrease in the resistivity, with the highest negative MR occurring close to the magnetic transition temperature, which is indicated by peak in the

zero-field resistivity. The peak in the resistivity becomes smaller and shifts to higher temperature with the field. This gives resistivity suppression in high field and MR known as high field magnetoresistance.

Low Field Magnetoresistance (LFMR)

Presently large numbers of research groups are trying to achieve large, low field RT MR in substituted rare earth manganites. The physical reason behind the observation of low field magnetoresistance (LFMR), in the epitaxial and granular thin films (with grain boundaries) as well as in the bulk sample is totally different [19]. The epitaxial film shows almost zero MR, however, bulk material show much larger negative MR as compared to the epitaxial thin films. This is one of the interesting aspects of transport in these materials and needs detailed investigation. In bulk samples and granular thin films having grain boundary effects, large LFMR at low temperature is exhibited due to the intergrain tunneling in the magnetic domain [20, 21].

1.2. Manganite thin films and hetrostructures: Properties and Applications

Besides the discovery of the large RT MR, the renewed interest in manganites has been propelled by another reason: the ability to synthesize high quality thin films as single crystal forms of complex perovskite oxide materials. The emergence of epitaxial metal oxide films has been one of the most attractive subjects of research of the condensed matter community in the last decade, which was primarily stimulated by the discovery of high-temperature superconductors (HTSC) and more recently by the discovery of CMR effects in the manganite.

Since most applications require thin films with good magnetic and electrical properties, it is of great importance to be able to prepare high quality single-crystalline epitaxial films. Different techniques including reactive sputtering, ion beam sputtering, co-evaporation, chemical vapor deposition (CVD) and pulsed laser deposition (PLD) have been used to grow the manganite thin films. PLD is the most straightforward method for thin film deposition of complex oxides due to its simplicity. In this technique, dense ceramic target is ablated by a pulsed laser under oxygen partial pressure, creating dynamic plasma constituting the bulk stoichiometry which condenses on the heated substrate. Since the stoichiometry of target material is complex and consists of more than

two constituents, it is often kept rotating during deposition to avoid the non-stoichiometric deposition of the thin film on to the substrate. Moreover, low pressure PLD under a strong oxidizing gas (ozone and atomic oxygen) allows a 'cell-by-cell' step-flow growth, which produces high quality epitaxial films or superlattices [22-23]. Manganite thin films are more often grown at high temperatures of ~ 600–800˚C to ensure a single crystal epitaxial microstructure. A small distortion in the unit cell of perovskite structured manganite material, i.e. the increase in the Mn–O bond length and the reduction in the Mn–O–Mn angle, changes the properties of the bulk material appreciably [24, 25]. Consequently, the physical properties of thin films are governed by the strain induced due to the lattice mismatch occurring between the film and the single crystal substrate. It is therefore of prime interest to control the internal microstructure of the film after deposition in order to understand the changes in both magnetic and electrical properties in fully strained films. There is a large effect of the growth parameters (such as temperature, pressure, and target-to-substrate distance) on both internal microstructure and surface morphology. Strain in the PLD deposited thin films has an appreciable effect on the electrical and magnetic properties of the material [26]. The strain in the film creates the magnetic anisotropy and dead layer in the manganite thin films which modifies the Low Field Magnetoresistance (LFMR) very effectively and results in to loss of the spin polarization.

In the interest of this thesis, which deals with the studies on the strain-induced magneto transport properties of manganite thin films and heterostructures, the effect of grain boundary & strain on the physical properties of film has been described in next part.

Grain Boundary Effect

Grain boundary (GB) strongly affects the properties of manganite thin films. LFMR has been attributed to the spin dependent scattering of polarized electrons at GB [20, 21]. Since large LFMR is highly desirable for practical applications, much effort has been made to enhance this property by artificially creating an interface between two elements.

Strain Effect

The influence of substrate strain is the main factor distinguishing manganite thin films from bulk ceramic sample. This is due to the fact that Mn e_g electrons, which determine most of the physical properties, are coupled to the lattice of freedom through the Jahn-Teller trivalent Mn. Thus, strain affects the properties of the manganite thin films and heterostructure. Consequently, to obtain and improve the desired properties, one needs to correctly understand the effects of the strain on the manganite thin films. Both in-plane and out-of-plane lattice parameters are often modified by strain effects when different substrates are used.

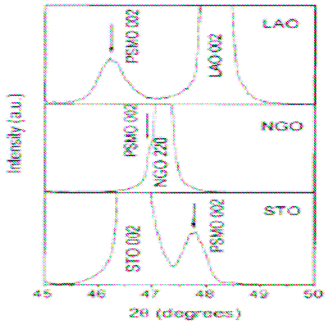

Figure 1.8: XRD patterns of three 30nm PSMO films grown on the LAO, NGO and STO substrate, respectively. The arrows indicate the PSMO (*002)* XRD reflections [Reproduced from ref. 27].

Figure 1.8 shows an example for 30nm thin films of PSMO grown on $LaAlO_3$ (LAO), $SrTiO_3$ (STO) and $NdGaO_3$ (NGO) substrates [27]. In this study, the effect of substrate on the physical properties is described and it is shown that, how the different substrates produce different tensile and compressive strain in the film [28]. Assuming that all the deposition conditions (oxygen pressure, target to substrate distance, deposition temperature, laser fluence) have been optimized to ensure a single crystal film, the strain modifies the transport as well as magnetic properties of the thin films.

Also in the dead layer of manganite thin films, magnetic anisotropy also plays an important role. The magnetic anisotropy of epitaxial thin films is usually an order of magnitude more than that of bulk samples depending on the strain in the film.

1.3 Applications of magnetoresistive materials

Basic research in the physical sciences, especially in condensed matter physics, can lead to important developments in applied physics and engineering. The manganites have potential for applications in various fields exploiting the property of CMR, spin polarized conduction of carriers and I-M transition. A few applications are listed below.

1. Magnetic Recording

The first application of manganite to produce a substantially large economic impact was that for the read heads in magnetic disk recorders, which are components of every computer. The read head senses the magnetic bits that are stored on the media (disks or tapes). This information is stored as magnetized regions of the media, called magnetic domains, along tracks (fig.1.9)

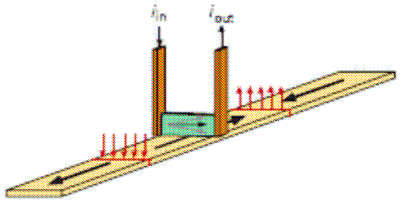

Figure 1.9: A schematic representation of a GMR read head (green) that passes over recording media containing magnetized regions. The magnetization direction of the soft layer in the head responds to the fields that emanate from the media bye rotating either up or down. The resulting change in the resistance is sensed by the current I passing through the GMR element. [Reproduced from ref. 2]

Magnetization is stored as a "0" in one direction and as a "1"in the other. Where two of these oppositely magnetized domains meet, there exists a domain wall, which is a microscopic region of 100 to 1000 Å (depending on the material used in the media). Although, there is no magnetic field emanating from the interior of a magnetized domain itself, uncompensated magnetic poles in the vicinity of the domain walls generate magnetic field that extend out of the media. It is these fields that are sensed by the GMR element. Where the heads of two domains meet, uncompensated positive poles generate

a magnetic field directed out of the media, and where the tails of two domains meet, the walls contain uncompensated negative poles that generate a sink for magnetic lines of flux returning back in to the media. The design goal for this element is to obtain a maximum rate of change in the resistance for a change in the sensed field. Typically, changes in the resistance of 1% per oersted are reported.

2. Nonvolatile Memory

The next application which is expected to have a large economical importance is nonvolatile memory. " Nonvolatile" refers to information storage that does not evaporate when power is removed from a system. Magnetic disks and tapes are the most widespread nonvolatile information storage media, because of their long storage lifetime, low cost and lack of any wear-out mechanism. Computer core memory itself was nonvolatile before the introduction of semiconductor RAM in the early 1970s (Fig.1.10).

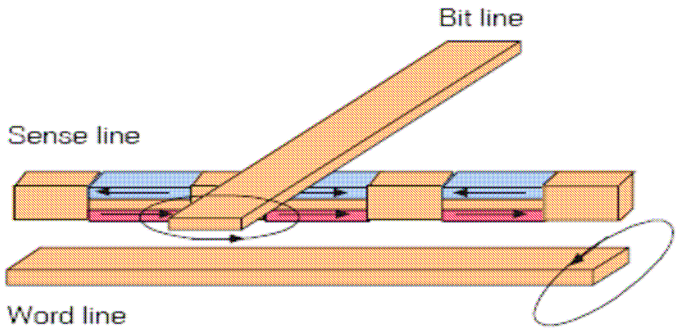

Figure 1.10: A schematic representation of RAM that is constructed of GMR elements connected in series. The elements are manipulated for writing or reading by applying magnetic fields that are generated by currents passing through lines above and below the elements. [Reproduced from ref. 2]

Honeywell had recently demonstrated that GMR elements can be fabricated in arrays with standard lithographic processes to obtain memory that has speed and density approaching that of semiconductor memory, but is nonvolatile [29]. An example of the structure of such an array is shown in fig.1.11. The GMR elements are essentially spin – valve structures that are arranged in series connect by lithographic wires to form a sense line. The sense line stores the information and has a resistance which is the sum of the

resistances of its elements. Current runs though the sense line and amplifiers at the ends of the lines detect changes in resistance in the elements. The magnetic fields needed to manipulate the magnetization of the elements are provided by additional lithographically defined wires above and below the elements with intersections at each of the GMR information storage elements.

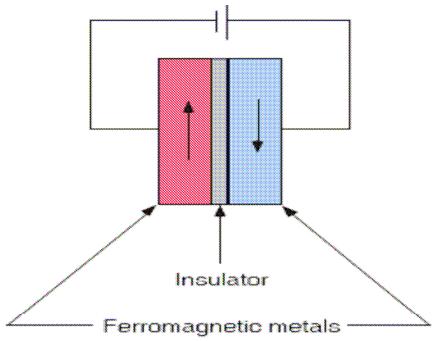

Figure 1.11: A magnetic tunnel junction formed by a thin insulating barrier separating two ferromagnetic metal films. Current passing though the junction encounters higher resistance when the magnetic moments are anti-aligned and lower resistance when they are aligned. [Reproduced from ref. 2]

3. IR Sensors (Bolometer)

The main material dependent properties of interest for the development of CMR bolometers are (1) operating temperature (2) high responsibility (3) optimized values of sheet resistances. The manganites exhibit large non-linear variation of resistivity with the temperature near I-M transition and, hence, are potential candidates for being used as bolometer sensors [30, 31]. The temperature coefficient of resistance (TCR) defined as $1/R(dR/dT)\times100$ evaluates the potentiality of any material for bolometer sensors. A good commercial bolometer possesses a TCR of ~ 4%. In some manganites, for example $La_{0.7}Ca_{0.3}MnO_3$, TCR as high as 10-18% has been exhibited. The TCR in most of the manganites increases manifolds on substitution of smaller size cation at A-site, but it occurs at low temperatures ,below RT ,which restrict them from applications.

4. Hybrid HTSC-CMR Devices

In these hybrid devices, injection of spin polarized carriers in to a superconducting strip forms a ferromagnetic contact pad, which locally quenches the superconductivity at the point of injection [32]. In this direction, FET structures can be fabricated using CMR materials as ferromagnetic layers epitaxially grown with YBCO layers. In such a device, the spin polarized electrons from the manganite layers are injected into the HTSC channel layers and the I-V characteristics as a function of gate current is studied [33]. Here, the properties largely differ when CMR layer with spin polarization character is replaced with the one having un-polarized electrons as carriers. Spin polarized carrier increases the pair breaking efficiency by many folds.

5. Spin Valve and Magnetic Tunneling Junction

A spin valve [Fig.1.12.(A)] is a GMR-based device which has two ferromagnetic layers (alloys of nickel, iron, and cobalt) sandwiching a thin nonmagnetic metal (usually copper), with one of the two magnetic layers being pinned; i.e. the magnetization in that layer is relatively insensitive to moderate magnetic fields [34]. The other magnetic layer is called the free layer and its magnetization can be changed by application of a relatively small magnetic field. As the magnetization in the two layers change from parallel to anti-parallel alignment, the resistance of the spin valve rises typically from 5 to 10 %. Pinning is usually accomplished by using an antiferromagnetic layer that is in intimate contact with the pinned magnetic layer. The two films form an interface that acts to resist changes in the magnetization of pinned magnetic layer.

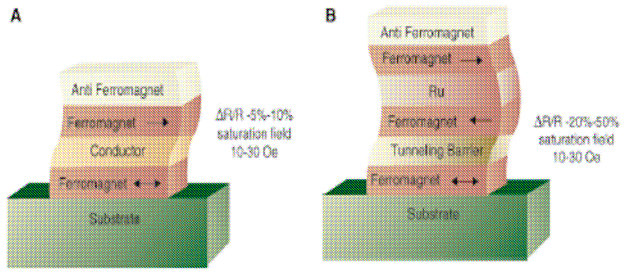

Figure 1.12: Spin-depend transport structures. (A) Spin valve

(B) Magnetic tunnel junctions. [Reproduced from ref. 45]

A magnetic tunnel junction (MTJ) [Fig.1.12.(B)] is a device in which pinned layer and free layer are separated by a very thin insulating layer, commonly aluminum oxide. The tunneling resistance is modulated by magnetic field in the same way as the resistance of a spin valve which exhibits 20 to 40% change in the MR and requires a saturating magnetic field equal to or somewhat less that that required for spin valves. Because the tunneling current density is usually small, MTJ devices tend to have high resistances. Applications for GMR and MTJ structures are expanding. Important applications include magnetic field sensors, read heads of hard drives, galvanic isolators and magnetoresistive random access memory (MRAM).

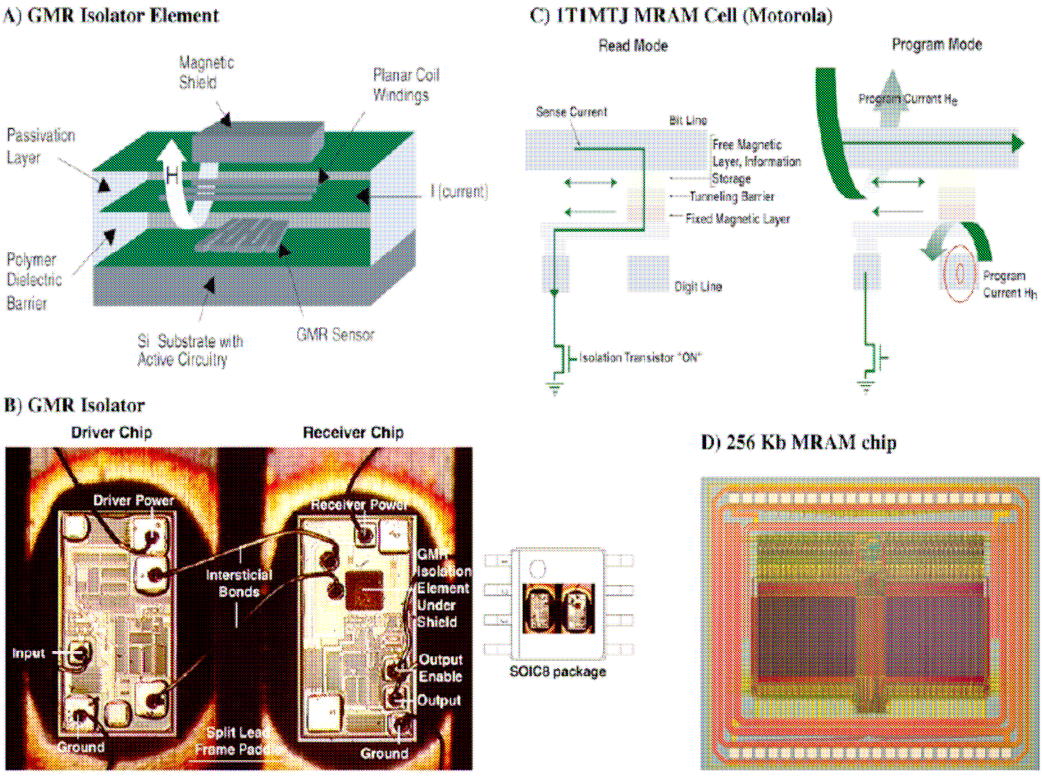

Figure 1.13: Device applications of MR thin films. [Reproduced from ref.35]

Other applications of magnetoresistive thin films and heterojunctions are shown in the figs. 1.13. Among these, galvanic isolator is a combination of an integrated coil and GMR sensor on an integrated chip (figure 1.13(A). The GMR isolator is ideally suitable for integration with other communication circuits and the packaging of a large number isolation channels on a single chip. Figure 1.13(B) shows a simple single

channel GMR isolator composed of a driver chip and receiver chip. Figures 1.13(C) & (D) show the schematic presentation of the MRAM cell and 256 Kb MRAM chip. Figure 1.14 shows the P-N junction type of device using the manganite thin film in which current is controlled by the magnetic field.

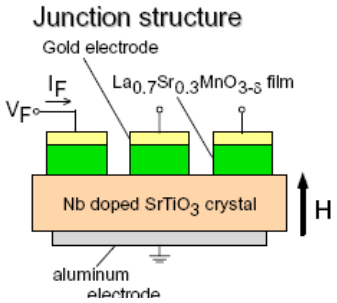

Figure 1.14: Field controlled P-N junction.

5. Electric Field Effect Devices

Manganites have also been tested in FET devices. CMR channel based FETs with either para-electric layer such as $SrTiO_3$ (STO) or a ferroelectric layer such as PZT have shown remarkable properties depending upon the nature of layer introduced. For STO the polarity has no effect on the response of the device and peak resistivity shifts to lower temperatures [36]. The lack of polarity in STO based device may be an indication of effects induced by the spin polarized character rather than charge injection. This device can help in understanding the fall of polarization with increasing Curie temperature. The ferroelectric gate based devices show large change in resistance (as large as ~ 100 %) which makes them attractive for potential non-volatile applications [37].

Future Applications

In addition to the abovementioned applications, which are either already available or near-term, there have been several demonstrations of effects that suggest possibility of using various manganites thin films and heterostructures in some other applications. Mixed-valent manganites also have potential for applications owing to their chemical properties of catalytic activity of Mn^{3+} and Mn^{4+} valence. The chemical properties include the catalysis of automobile exhausts, oxygen sensors and solid electrolytes in fuel cells. The alkali ion substituted manganites are useful in such kind of applications.

Also, a metal-base transistor has been fabricated, which uses a GMR multilayered magnetic metal film for the base [38]. The mean free path of the electrons in the metal base can be altered by switching the GMR layer from its anti-aligned high resistance state, resulting in a drop in the trans-conductance of the device. Finally, several research groups are pursuing the injection of spin-polarized carriers into a two dimensional electron gas channel that is formed at a compound semiconductor heterostructure interface [39]. The long mean free path of electrons in these channels is expected to yield micrometer-length paths that are free of spin-flip scattering for spin-polarized carriers.

1.3. Swift Heavy Ion Irradiation (SHI) Study

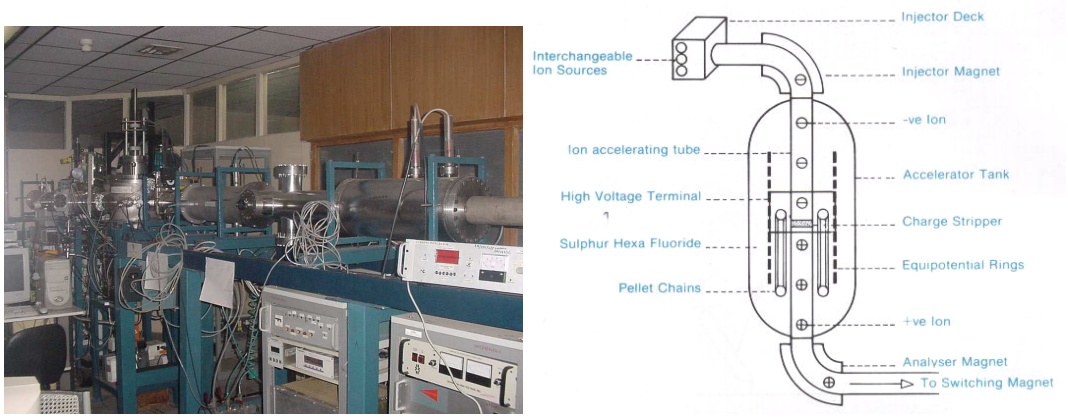

Figure 1.15: Photograph of the beam line dedicated to material science research at IUAC, New Delhi. A schematic diagram showing the principle of acceleration of ions in pelletron. [Reproduced from ref. 42]

Modifications in the characteristics of the manganite thin films due to the swift heavy ions irradiation is an exciting but not yet fully understood area of research [40, 41]. The study of the swift heavy ion (SHI) irradiation is an important technique to create controlled defects in thin films. It is an established fact that SHI irradiation is responsible for the dramatic changes in the transport and magnetic properties of manganites because it creates the effects like: changes in the surface morphology, magnetic anisotropy, columnar or point defect formation, amorphaizasion of the material, etc [40, 41]. Figure 1.15 shows the photograph of the beam line dedicated to material science research

at IUAC, New Delhi, while schematic diagram showing the principle of acceleration of ions in pelletron is shown next to the photograph.

It is interesting to study, the modifications in the resistive and magneto transport properties induced by the point or columnar defects formed by the irradiation of Ag^{+15} ions on Pulsed Laser Deposited CMR thin films and multilayered structures. The creation of point or columnar defects, act as scattering centers for the conduction of the carriers resulting in an increased peak resistivity. The magnetic field application can reduce the scattering resulting in an enhancement of MR. Usually the SHI studies are carried out on manganite thin films so that the ion can pass though the sample and finally strike the substrate. SRIM calculations are useful for the determination of electronic & nuclear energy loss of energetic ion on their passage through the material.

1.4 Motivation of the Present Work

The $LaMnO_3$ manganite possesses ABO_3 type perovskite structure and is an antiferromagnetic insulator (AFI) below 170K. On substituting divalent cations at trivalent La^{3+} site, the resulting composition $La_{1-x}A_xMnO_3$ (where, A is divalent cation) display interesting correlated transport, magnetic and magnetoresistive properties. The physical properties of these compounds are determined by three main factors; i) the divalent doping at the La-site (which determines the ratio of Mn^{3+}/Mn^{4+}) ii) the average A-site cation radius and iii) size-disorder at the A-site. Depending upon these factors, the exchange interaction between the Mn^{3+} and Mn^{4+} ions via oxygen, largely known as Zener Double Exchange (ZDE), comes into play and drives the material to exhibit insulator to metal transition at T_P and paramagnetic to ferromagnetic transition at T_C. In the vicinity of T_P, the resistivity drops by a large magnitude on the application of an external magnetic field, thus making these materials to exhibit a large negative MR.

The application potential of manganites has prompted to synthesize them in thin film forms. The study of epitaxial films enhances our understanding of various physical properties of manganites in the absence of dominating grain boundary effects. In addition to observation of the CMR effect and the occurrence of metallic phases with a fully spin-polarized conduction band, these new materials have potential applications in variety of magnetic and recording devices. For this, it is necessary to master the growth of high quality thin films with controlled and tailored properties. Progress in the growth of

epitaxial thin films opened up a way for the application of magnetic oxide materials in devices.

The present research work is of major importance in the context of development of thin films and multilayered structures having low field, large CMR effect observed near RT. It is speculated that, various thin films of the mixed valent manganites deposited using PLD technique will possess highly tunable transport and magnetic properties. To achieve this goal, I have grown the single crystalline $La_{0.5}Pr_{0.2}Sr_{0.3}MnO_3$ (LPSMO) thin films on the different single crystalline $SrTiO_3$ (STO) and $LaAlO_3$ (LAO) substrates with the varying thickness, having transition temperatures (T_P) in the vicinity of the RT which exhibits relatively high a MR ~ 60-70 % around RT in 5 T field. Field dependencies of MR at different temperatures show that, MR % increases appreciably above 200 K & has a maximum value of ~ 82 % at 275 K. Also these films exhibit, the half metallic nature in a wide range of temperature (5-220K) which is highly useful physical property in application as spin injector device.

Swift Heave Ions are known to produce the wide variety of defects and lattice distortions in the material, which creates modifications in the electronic transport and magnetic properties. Observation of large change in the structural, electronic transport, magnetic and magnetotransport properties of the $La_{0.7}Ca_{0.3}MnO_3$ have been studied as function of irradiation doses (10^{10}-10^{14} ions/cm^2). It is found that physical properties changes gradually up to a dose of 10^{13} ions/cm^2; however, drastic change occurs when the sample is irradiated at the higher dose of 10^{14} ions/cm^2. Also columnar defects and points defects are created in the manganite thin films due to the SHI irradiation. The observed modifications in the noise properties and temperature sensitivity of the irradiated $La_{0.75}Ca_{0.5}MnO_3$ thin films are consistent with general expectation concerning the effect of SHI irradiation induced lattice defects.

In the present work, an effort is made to study the thickness dependent irradiation effects on the electronic and magneto transport properties of the $La_{0.5}Pr_{0.2}Ba_{0.3}MnO_3$ (LPBMO) manganite thin films. It is shown that, the columnar defects formed due to SHI irradiation of LPBMO film, release the strain at the interface of film and substrate in the lower thickness films resulting in to the decrease in the resistivity, while a large damage caused by the energetic ions with increasing thickness, creates more scattering

centers and enhances resistivity resulting in to higher values of Temperature Coefficient Resistances (TCR).

During the course of present work, I have grown few manganite heterostructures of LPSMO/Al_2O_3/LPSMO with an aim to improve the MR in the vicinity of the RT. It is seen that, in such a multilayered structure, observation of large MR (~77 %) in the vicinity of T_P (~ 210 K) is mainly due to magnetic field controlled spin fluctuations in the scattering barrier of Al_2O_3. At low temperatures, hysterisis in the MR vs. H curve of these multilayers indicate a percolative transport behavior through the FMM manganite layer impregnated with the scattering barrier, which seems to be responsible for the large MR (~39 %). Temperature Coefficient of Resistance (TCR) for the heterostructure is found to be almost twice that of the parent LPSMO thin film. Observation of large field sensitivity (~ 20 %) in the 0.5 Tesla field, can be of interest for the application of such a multilayered manganite as a field sensor. In addition, it has been shown that how the substrate induced strain, oxygen annealing and other preparative factors affect the physical properties of the films under study.

Details of the various chapters comprising the present thesis are as below

Chapter I

This chapter introduces in brief, the phenomenon of CMR in mixed valent manganites from physics and application point of view. Various physical properties exhibited by CMR materials are described in detail. Also, the properties and phenomena exhibited by CMR thin films and multilayered structures are discussed, followed by description about their applications in magnetic recording, memory, sensors, spin valves, etc. In addition, the effects of Swift Heavy Ions (SHI) irradiation on the modification in properties of manganite thin films have been discussed in the light of controlled defects introduced by SHI. At the end of this chapter, motivation for present work has been given.

Chapter II

Chapter II describes, in short, various experimental tools and methods used for characterization of the bulk & thin films manganites studied in the present work. The synthesis of the thin films by Pulsed Laser Deposition (PLD) and Chemical Solution Deposition (CSD) techniques are described in detail. The details about the Rietveld method for the analysis XRD data has been emphasized to explain the phase formation and other structural details. The basic principle and description of the various techniques such as d.c. four-probe method for resistivity measurements, d.c. and a.c. magnetization measurements, magnetoresistance measurements, their need and importance as a characterization tool has been discussed. The principle and working of the various instruments such as Pulsed Laser Deposition system, Atomic Force Microscope, SQUID magnetometer, Physical Property Measurement System (PPMS) used to characterize of the samples studied has also been given in this chapter.

Chapter III

In this chapter, a detailed study of the structural, transport and magnetotransport properties of the $La_{0.5}Pr_{0.2}Sr_{0.3}MnO_3$ (LPSMO) manganite thin films deposited on LAO and STO substrates with varying thicknesses have been given. From the electronic transport and fitted ρ-T data in the magnon scattering laws, it has been proved that, LPSMO films posses half metallic behavior in a wide temperature range (5 to 200 K) which is absent in the case of LSMO films. Also, thickness and substrate effects on the

transport and magnetotransport properties are discussed in detail in this chapter. Phenomenon of release of strain at the film-substrate interface due to the SHI irradiation has been discussed briefly and is explained in terms of the dominance of the dead layer in thinner film and ion induced annealing and damage in the crystalline structure of the films.

Chapter IV

This chapter is completely devoted to the investigations on the SHI irradiation studies on the $La_{0.5}Pr_{0.2}Ba_{0.3}MnO_3$ (LPBMO) manganite thin films. The studies on thickness dependent SHI irradiation effects on the electronic transport of the LPBMO thin films shows that, with increasing irradiation dose, there is a significant enhancement in resistivity and decrease in the T_P of the 200 nm film while there is no appreciable change in 50 nm thin film. The cause for such behavior may be either due to (i) a large damage generated by the energetic ions with increasing thickness, which creates more scattering centers and enhances resistivity or (ii) the presence of columnar tracks which may cause a local release of strain at the film-substrate interface which increases the conductivity in low thickness films. In addition, we have studied the effect of the SHI irradiation on the low temperature minima and has shown that defects reduces the role of inelastic scattering in the resistivity resulting in to broadening effect in the minima curves.

Chapter V

In this chapter, results of studies on electronic and magnetotransport properties of the manganite - based multilayered structure of LPSMO/Al_2O_3/LPSMO grown by the Pulsed Laser Deposition (PLD) are given. It is shown that, how the sandwiched insulting Al_2O_3 barrier between the two ferromagnetic LPSMO layers, is responsible for providing the spin scattering centers which can be controlled by the external applied field resulting in high MR in the multilayer as compared to LPSMO thin film. In addition, the study on the oxygen annealing effects on the physical properties of the manganite multilayers show that, these multilayers are useful for field sensing application. At the end of this chapter, a comparative study of physical properties of LCMO manganite thin films grown by Chemical Solution Deposition (CSD) and Pulsed Laser Deposition (PLD) technique has been given.

REFERENCES

1. M. N. Baibich, J. M. Broto, F. Nguyen Van Daw, F. Petroff, P. Etienne, G. Crevzet, A. Friederich and J. Chazelas

   Phys. Rev. Lett. **61** 2472 (1988).

2. Gary A. Prinz

   Science **282** 1660 (1998).

3. M. Julliere

   Phys. Lett. A. **54** 225 (1975).

4. S. Zin, T. H. Tiefel, M. McCormack, R. A. Fastnacht, R. Ramesh and L. H. Chen Science **264** 413 (1994).

5. R. Von Helmolt, J. Wecker, B. Holzapfel, L. Schultz and K. Samwer

   Phys. Rev. Lett. **71** 2331 (1993).

6. J. B. Goodenough

   Phys. Rev. **100** 564 (1955).

7. C.P. Zener

   Phys. Rev. **81** 440 (1951).

8. P. W. Anderson and H. Hasegawa

   Phys. Rev. **100** 675 (1951).

9. P. G. de Gennes

   Phys. Rev. **118** 141 (1960).

10. M. Viret, L, Ranno and J. M. D. Coey

    Phys. Rev. B **55** 8067 (1997).

11. B. Reveau, A. Maignan, C. Martin and M. Hervieu

    " Colossal Magnetoresistance, Charge Ordering and Related properties of manganites Oxides" ed:by C. N. R. Rao and B. Raveau

    (Singapore: word scientific) P 43, P 83 (1998).

12. J. M. D. Coey, M. Viret, L. Ranno and K. Ounadjela

    Phys. Rev. Lett. **75** 3910 (1995).

13. Y. Tokura, Y. Tomioka, H. Kuwahara, A. Asamitsu, Y. Morimoto and M. Kasai
J. Appl. Phys. **52** 88 (1998).
14. E. Wollen and K. Koehler
Phys. Rev. **100** 545 (1955).
15. H. Kuwahara, Y. Tomioka, A. Asamistu and Y.Tokura
Science **270** 961 (1995).
16. R. A. De Groof, F. M. Moller, P. G. Van Engen and K. H. J. Buschow
Phys. Rev. Lett. **50** 2024 (1983).
17. K. Schwarz
J. Phys. F. **16** L211 (1986).
18. Y. Okimoto
Phys. Rev. Lett **75** 109 (1995).
19. H. Y. Hwang, S-W Cheong, N. P. Ong and B. Batlogg,
Phys. Rev. Lett. **77** 2041 (1996).
20. J. Z. Sun, L. Krusin-Elbaum, D. K. Duncombe, A. Gupta and R. B. Laibowwitz
Appl. Phys. Lett. **70** 1769 (1997).
21. A. Gupta, G. Q. Gong, G. Xiao, P. R. Duncombe, P. Lecouer, P. Trouilloud,
Y. Y. Wang, V. P. Dravid and J. Z. Sun
Phys. Rev. B **54** R15 629 (1996).
22 J. A. Thornton
J. Vac. Sci.Technol. **A 4** 3059 (1986).
23. M. Strikovski and H. J. Miller
Appl. Phys. Lett. **73** 1733 (1998).
24. Lan MacLaren, Zhong Lin wang, H. S. Wang and Qi Li
Appl. Phys. Lett. 80 1406 (2002).
25. H. L. Ju, J. Gopalakrishnan, J. L. Peng, Q. Li, G. C. Xiang, T. Venkatesan and
R. L. Greene
Phys. Rev. B **51** 6143 (1995).
26. J. Z. Sun, D. W. Abraham, R. A. Rao and C. B. Eom
J. Appl. Phys. **74** 3017 (1999).

27. H. S. Hwang, E. Wertz, Y. F. Hu. G. Li and D. G. Schlon
J. Appl. Phys. **87** 7409 (2000).

28. R. A. Rao, D. Lavric, T. K. Nath, C. B. Eom, L. Wu and F. Tsui
Appl. Phys. Lett. **73** 3294 (1998).

29. M. Dax
Semicond. Lnt. **20** (No.10) 84 (1997).

30. R. N. Parmar, J. H. Markna, D. G. Kuberkar, Ravi Kumar, D. S. Rana, V.C. Bagve and S. K. Malik
Appl. Phys. Lett. **89** 202506 (2006).

31. A. Goyal, M. Rajeshwari, R. Shreekala, S.E. Lofland, S.M. Bhagat, T. Boettcher, C. Kwon, R. Ramesh and T. Venktesan
Appl. Phys. Lett. **71** 1718 (1998).

32. M. Rajeshwari, C.H. Chen, A. Goyal, C. Kwon, M.C. Robson, R. Ramesh, T. Venkatesan and S. Lakeou
Appl. Phys. Lett. **68** 3555 (1996).

33. Z. W. Dong
Appl. Phys. Lett. **71** 1718 (1997).

34. B. Dierry
J. Appl. Phys. **69** 4774 (1999).

35. S. A. Wolf, D. D. Awschalom, R. A. Buhrman, J. M. Daughton, S. Von. Molnar, M. L. Roukes, A. Y. Chtchelkanova and D. M. Treger
Science **294** 1488 (2001).

36. S. B. Ogale, V. Talyansky, C. H. Chen, R. Ramesh, R. L. Greene and T. Venkatesan
Phys. Rev. Lett. **77** 1159 (1996).

37. S. Mathew, R. Ramesh, T. Venkatesan and J. Benedetto
Science **276** 238 (1997).

38. D. J. Monsama, J. C. Lodder, T. J. A. Popma and B. Dieny,
Phys. Rev. Lett. **74** 5260 (1998).

39. J. Nitta, T. Akazaki, H. Takayanagi and T. Enoki
Phys. Rev. Lett. **78** 1335 (1997).

40. S. B. Ogale, R. Shreekala, R. Bathe, S. K. Date, S. I. Patil, B. Hannoyer, F. Petit and G. Marest
Phys. Rev. B **57** 7841 (1998).

41. Ravi Kumar, R. J. Choudhary, S. I. Patil, Shahid Hussain, J. P. Srivastava and S. K. Malik
Appl. Phys. Lett. **86** 222501 (2005).

42. www.iuac.ernet.in

Chapter - 2

2.1 Synthesis Methods

The synthesis of materials with desired physical properties has been an area of increasing vitality and importance in the past few years. New phenomena arise because the size of the resulting materials is of the same order as the fundamental interaction distances which gives rise to new physical phenomena and enabling new technologies. In the PLD technique, dense and single-phase bulk target is used for the ablation process to make good quality films. Therefore, the selection of sample preparation method is a crucial factor. The synthesis of polycrystalline bulk target samples is broadly divided into two categories namely; 1) solid state reaction method and 2) chemical route comprising sol-gel technique, nitrate route, co-precipitation technique, etc. [1-3]. Due to its simplicity, all the bulk polycrystalline samples studied during the course of present work have been synthesized using the solid-state reaction method. In order to prepare a single-phase sample, the synthesis conditions during any reaction are very important. During synthesis, the parameters such as temperature, pressure, gas flow and time for the reaction are needed to be varied according to the phase requirements in the sample. Mapping of all variables has to be made to select the conditions, which are best suited for each material and phase. In the CSD technique, we have used co-precipitation technique in which the mixing, stirring and heating of appropriate stoichiometric quantities of the metal acetates in a distilled water and acetic acid resulted in a clear solution of the constituents used for deposition. In CSD method, the parameters such as temperature and annealing time were varied to achieve desired physical properties.

2.1.1 Ceramic method

The most common method of synthesizing inorganic solids is by the reaction of the component materials at elevated temperatures. If all the components are solids the method is called the ceramic method. As the name suggests, the solid form of the constituents are reacted at high temperatures for a certain minimum period of time which is generally attained by resistance heating. The general procedure involved in solid-state reaction method for producing mixed valent manganite oxides is described below.

In the present work, firstly the stoichiometric composition of constituent materials in the form of carbonates, oxides, nitrides, etc. (all 99.99% pure Aldrich make) were preheated for appropriate time and temperature (350°C to 550°C) to remove the

low temperature volatile impurities and then weighed in proportionate quantities according to the desired composition. In the solid state reaction, for the reaction to take place homogeneously, it is very important to mix and grind the powders thoroughly for long duration to obtain homogeneous distribution in required proportions of the desired stoichiometric compound. The proper grinding of mixed powders using pestle-mortar decreases the particle size, which is necessary for obtaining close contact among the atoms so the right material is formed. This powdered mixture is then heated in air at about 950^{o}C. During the first calcination, CO_2 is liberated from the mixture. After successive calcinations, the compounds are reground, palletized and sintered for a long time (~100 hours) in the temperature range 1100^{o}C - 1250^{o}C. Before every sintering of samples, the samples were ground throughly to obtain back powders until the particle size reduced to ~ 40 micron size by using suitable sieves and then pressed into cylindrical pallets. Many intermediate grindings are required to get appropriate phase formation and phase purity. These heatings in atmospheric conditions are required to obtain single phasic material and to release the remaining CO_2, if any. The final sintering is carried out at a sufficiently high temperature (in the range 1300-1400^{o}C) to get the better crystallization. The furnace is turned off and the samples are left inside to cool to RT.

The solid-state reaction method has proved to be the most suitable for synthesizing reproducible samples of CMR manganite oxides. The similar oxygen annealing is not important for manganites as these materials posses good stability of oxygen stoichiometry.

2.1.2 Laser ablation Technique

The interest in the use of Pulsed Laser Deposition (PLD) technique for the thin film synthesis is mainly due to the good quality of films of mixed oxide materials prepared using this technique as compared to other methods. This technique is also used to deposit the thin films of multicomponent oxides such as ferroelectric and ferrites [4, 5]. The ease, with which oxide ceramic materials can be grown as high quality thin films using PLD method, makes it as important technique for the growth of oxide thin films. In the present work the PLD technique is used to synthesise the manganite thin films and multilayers structures.

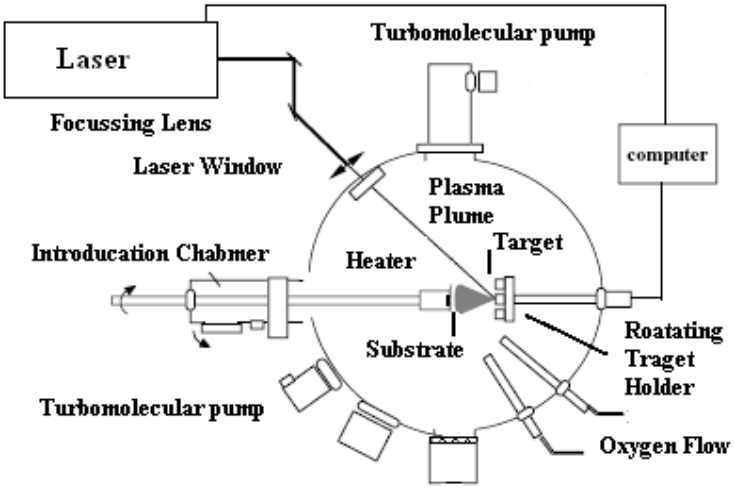

Figure 2.1: A schematic illustration of a typical pulsed laser deposition (PLD) system.

A schematic illustration of a typical PLD system is as shown in fig.2.1. Usually, Excimer laser is used for deposition. Between the ouput port of the laser and the port of the deposition chamber, optical elements are placed in order to steer and focus the laser beam. The optical elements that couples the energy from the laser to the target are leses and aperatures, such as mirrors, beam splitters, and laser windows. Once the laser beam passes through the optical elements it enters the deposition system and is focused onto the surface of the target. All the elements in the target are then repidly heated up to their evaporation temperature. The emitted materials tend to move towards the substrate, and condense on the substrate. Well polished substrate located at a typical distance from the target is stationary or rotated for homogenization of the deposited material. The temperature of the substrate may be kept between RT and 850^{o}C. This temperature depends upon the nature of material used for ablation. A gas supply is often provided to produce desired chemical reaction during film growth. Mixed oxide materials are prone to loose oxygen during the deposition. Therefore, during deposition of such oxide materials, certain optimum partial pressure of oxygen is maintained during the deposition. During the course of present work, the O_2 partial pressure was maintained at 400 mTorr. The vacuum chamber is made up of stainless steel and is evacuated down to 10^{-6} bar by using a turbo pump.

The most important feature of PLD is that, the stoichiometry of the target can be retained in the deposited films. This is the result of the extermely high heating rate of the target surface (~10^8K/s) due to pulsed laser irradiation. It leads to the congruent evaporation of the target regardless of the vaporizing temperature of the constituent elemments of compounds of the target.

To synthesise the thin films of manganites studied during this work, Q-Swiched Nd:YAG laser with the wavelength of 6nm, the energy density of 2.17 J/cm^2 and KrF excimer gas laser with the wavelength of 25nm and the energy density of ~ 3.1 J/cm^2 were used.The details of deposition condition and parameters used for Nd: YAG and KrF lasers are discussed in chapters 3 and 4 respectively.

Principle of PLD

The principle of pulsed laser deposition is a very complex physical phenomenon. It comprises many processes in a chain namely, 1) the physical process of the laser-material interaction on solid target followed by 2) the formation of plasma plume with high energetic species and 3) the transfer of the ablated material through the plasma plume onto the heated substrate surface. Firstly, the pulsed laser beam is focused onto the surface of the target. This laser beam strikes the surface of the target material with sufficiently high energy and short pulse duration, which results into the rapid heating of the target elements up to their evaporation temperatures. Because of such a high energy, the elements are dissociated from the target surface and ablated out with stoichiometry as in the target. In most materials, the ultraviolet radiation is absorbed by only the outermost layers of the target up to a depth of ~ 1000 Å. The extremely short laser pulses (<50 ns) rapidly increase temperature of the surface to thousands of degrees Celsius, but the bottom of the target remains virtually unheated. Such un-equilibrium heating produces a flash of evaporated elements that deposit on the substrate, producing a film with composition identical to that of the target surface. Rapid deposition of the energetic ablation species helps to raise the substrate surface temperature. In this respect PLD tends to demand a lower substrate temperature for crystalline film growth.

2.1.3 Spin coating method

Chemical Solution Deposition (CSD) using a spin coater is another technique to obtain the polycrystalline and single crystal thin films and is highly inexpensive

technique as compared to PLD and sputtering methods. By using, CSD method, epitaxial and polycrystalline thin films can be deposited through many routes. The synthesis of the manganite thin films was carried out by dissolving the stoichiometric amounts of metal acetates such as $La(CH_3COO)_3$, $Ca(CH_3COO)_2$ and $Mn(CH_3COO)_2$ in acetic acid and distilled water. This precursor solution was then heated (80 ^oC) and stirred until the clear aqueous solution formed which was used for the thin film deposition. Thin films were then heated at 350 ^oC and annealed at different temperatures varying from 700 ^oC to 1100 ^oC. The CSD method helps in controlling the particle size by varying the rpm (rotations per minute) of the spin coater. The deposited thin films sintered at different temperatures will decide the connectivity and compactness of the thin films. The deposition parameters can be optimized to obtain physical properties of the thin films exhibiting large magnetoresistance in low fields and near room temperature.

2.2 Structure and surface morphology

The X-ray diffraction technique, in addition to its major use in analysis of crystal structures, finds a multitude of other applications in material science. Indeed much of our knowledge of the microscopic world has been derived from the persistent use of X-ray techniques. X-ray diffraction technique is highly useful in determination of phase purity of bulk polycrystalline material and expitaxy of the thin film. In the same way, surface morphological studies are of importance for the understanding of the films growth on the different substrate as well as grain size and surface roughness. Also surface morphology is highly useful to observe the defects created by the irradiation on the film surface, which has large impact on the physical properties and microstructure. During the course of work of this work, XRD measurements have been carried out on all the bulk targets and thin films to ascertain the structural purity and other important crystallographic information such as compressive and tensile strain and particle size. To study surface morphology of the pristine and irradiated thin films, I have used Atomic Force Microscopy (AFM) technique. The details of these two techniques is given in next section.

2.2.1 X-ray diffraction (XRD)

X-rays are electromagnetic waves whose wavelengths are in the neighborhood of 1Å. Except for the fact that their wavelength is so short, they have the same physical

properties as other electromagnetic waves, such as optical waves. The wavelength of an X-ray is thus of the same order of magnitude as the lattice constants of crystals and it is this which makes X-rays useful in the analysis of crystal structures [6, 7].

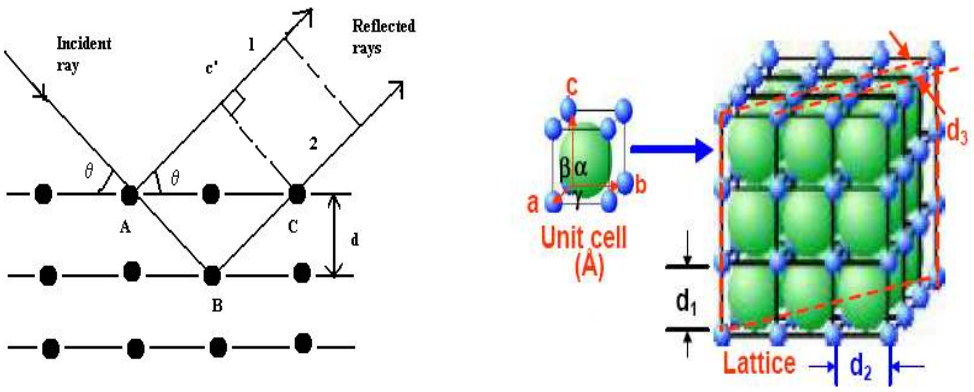

Figure 2.2: Reflection of X-rays from a crystal. The reflected rays are nearly parallel because the detector is positioned far form the crystal. A smallest building block of unit cell.

When a monochromatic X-ray beam is incident on the surface of a crystal, it is reflected. However, the reflection tales place only when the angle of incidence has certain values. These values depend on the wavelength and the lattice constants of the crystal, and consequently it seems reasonable to attempt to explain the selective reflectivity in terms of interference effects, as in the physical optics. If we consider a crystal as a series of planes with their inter-atomic distance being'd'. Then the incoming X-ray, with wavelength, λ, will undergo scattering and interfere constructively only with that from adjacent planes at special angles 'θ', that satisfies the Braggs condition (Fig.2.2),

$$n.\lambda = 2d\sin\theta$$

A crystal contains parallel planes along three different axes, so the actual measured values of θ vary with the alignment between the crystal planes and the incoming beam of X-rays. A plane perpendicular to the crystallographic a-axis is called the [100] plane; one perpendicular to b-axis is called [010] plane, and so on. Cell parameters a, b and c (length) and α,β, and γ angles between a, b, and c which can be determined by using XRD.

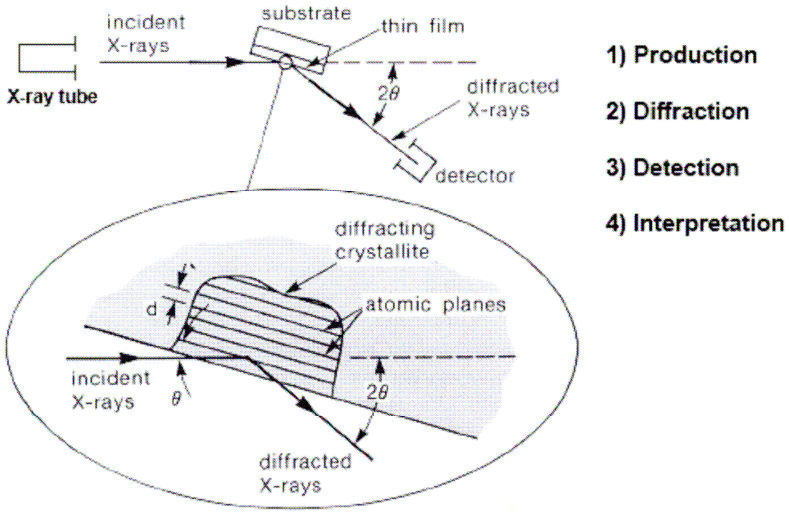

Figure 2.3: Basic factures of typical XRD experimental setup for the thin film measurement.

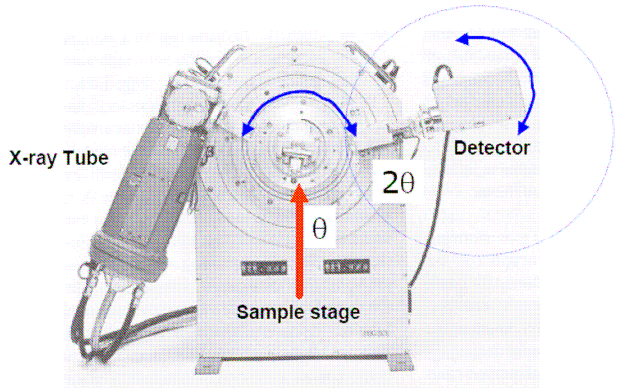

Picture 2.1: A modern automated X-Ray diffractometer.

Figure 2.3 shows the schematic diagram of experimental setup for determination of the structure of thin films using XRD. The Picture 2.1 shows the modern automated X-ray diffractometer. Powder XRD (X-ray Diffraction) is the most widely used x-ray diffraction technique for characterizing polycrystalline materials [8]. From the XRD measurements, we can study the phase purity, crystallographic perfection, orientation relationship, and lattice constants of the manganite bulk and thin films.

Rietveld Analysis

The Rietveld method refines a XRD data by comparing the observed diffraction pattern with the calculated from the known crystal structure. A least-square refinement is used to optimize the structure parameter [9,10].

The refinements of the XRD data of all the bulk samples studied were made using FULLPROF program. The order of refining the parameters was: the scale factor, the zero point for 2θ, five of the background parameters, the cell parameters, three of the peak shape parameters, the z co-ordinates, the isotropic displacement parameters, the occupation numbers, the fourth peak shape parameter, the anisotropic displacement parameters and the last background parameter. A few different routes to convergence were tried to confirm an optimal result. The R factors are good indicators if a route is not converging to a reliable result. Obtained cell parameters of bulk material are used to index the XRD peaks of the thin films.

Applications of XRD

- XRD is nondestructive technique
- To identify crystalline phase and orientation
- To determine structural properties: Lattice parameters, strain, grain size, expitaxy, phase composition, preferred orientation (Laue) order-disorder transformation, thermal expansion
- To measure thickness of thin films and multi-layers
- To determine atomic arrangement

2.2.2 Atomic force microscopy (AFM)

The atomic force microscope (AFM) was invented in 1986 by Binnig, Quate and Gerber [11]. Like all other scanning probe microscopes, the AFM utilizes a sharp probe moving over the surface of a sample in a raster scan. In the case of the AFM, the probe is a tip on the end of a cantilever, which bends in response to the force between the tip and the sample. When the probe is scanned over the surface, the cantilever responds to valleys and other features of the sample surface that it encounters. These reactions are recorded and produce an image of the material's surface showing the presence of humps and valleys on the surface, resembling a surface topographic map.

Picture 2.2: The Multimode model AFM uses sample scanning to obtain topographic and phase imaging of the surface and hence the sample size is limited to ~ 1 cm^2. This equipment can image samples using the Contact mode, Tapping mode and Imaging under liquid. In addition this equipment is capable of imaging under variable temperature from room temperature up to 250°C.

One method of AFM is the use of contact mode where the cantilever remains in contact with the surface during scanning. When it encounters variations in the surface it responds by deflecting to follow the contours. This process produces accurate topographical maps of the surface for many different samples, but there are some unwanted drawbacks. With the cantilever in continuous contact of the sample, damage to the surface can occur which can then alter both the resulting image and properties of the material.

To counter this problem, a new method called tapping mode was developed. In this process, the cantilever arm is oscillating at a resonant frequency as it scans the surface. When the tip begins to lightly touch the surface, a sensor reverses the motion of the cantilever to continue the oscillation. The tip then intermittently touches the surface,

instead of being dragged avoiding damages. But since the cantilever is not in continuous contact with the surface, a method of measuring the differences in the surface height must be determined. This results from changes in the amplitude of oscillation of the cantilever. When it encounters bumps on the surface, the amplitude of oscillation is reduced. Conversely, valleys or depressions cause the amplitude to increase. By recording these changes, an accurate topographical map can be produced without damaging the surface of the material. To ensure that the oscillation and amplitude remain fairly constant, a digital feedback loop is also implemented.

AFM use feedback to regulate the force on the sample. The presence of a feedback loop is one of the subtler differences between AFM and older stylus-based instruments such as record players and stylus profilometers. The AFM not only measures the force on the sample but also regulates it, allowing acquisition of images at very low forces.

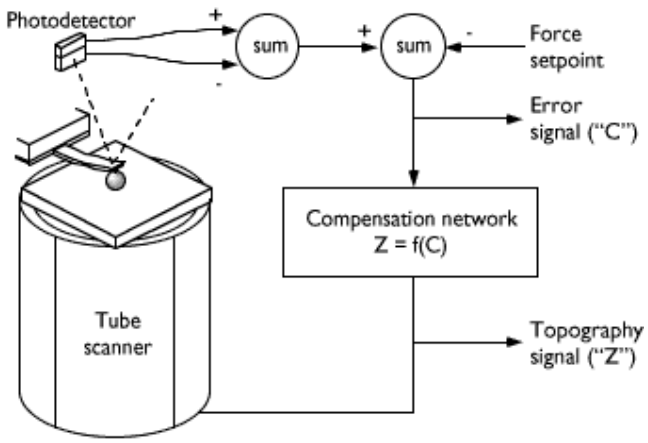

Figure 2.4. The AFM feedback loop. A compensation network monitors the cantilever deflection and keeps it constant by adjusting the height of the sample.

The feedback loop (Fig.2.4) consists of the tube scanner that controls the height of the entire sample; the cantilever and optical lever, which measures the local height of the sample; and a feedback circuit that attempts to keep the cantilever deflection constant by adjusting the voltage applied to the scanner. One point of interest: the faster the feedback loop can correct deviations of the cantilever deflection, the faster the AFM can acquire images; therefore, a well-constructed feedback loop is essential to microscope

performance. AFM feedback loops tend to have a bandwidth of about 10 kHz, resulting in image acquisition times of about one minute.

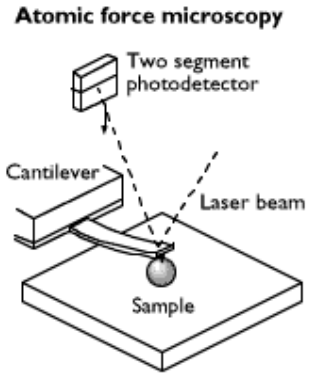

Figure 2.5: A schematic illustration of AFM set-up while topographic imaging uses the up-and-down deflection of the cantilever, frietion imaging uses torsional deflection.

Almost all AFMs can measure sample topography in two ways: by recording the feedback output ("Z") or the cantilever deflection ("error") [see fig.2.4]. The sum of these two signals always yields the actual topography, but given a well-adjusted feedback loop, the error signal should be negligible. As described below, AFMs may have alternative imaging modes in addition to these standard modes. If the scanner moves the sample perpendicular to the long axis of the cantilever (Fig. 2.5), friction between the tip and sample causes the cantilever to twist. A photodetector position-sensitive in two dimensions can distinguish the resulting left-and-right motion of the reflected laser beam from the up-and-down motion caused by topographic variations [12].

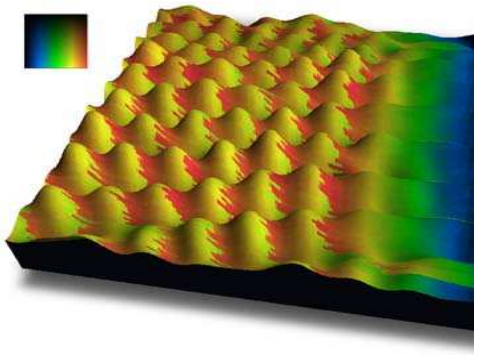

Picture 2.3: 2.5 x 2.5 nm simultaneous topographic and friction image of highly oriented pyrolytic graphite (HOPG). The bumps represent the topographic atomic corrugation, while the coloring reflects the lateral forces on the tip. The scan direction was right to left.

Therefore, AFM can measure tip-sample friction while imaging sample topography. Besides serving as an indicator of sample properties, friction (or "lateral force," or "lateral deflection") measurements provide valuable information about the tip-sample interaction. Picture 2.3 shows a simultaneous friction and topographic image of graphite atoms in 3-D projection is shown as above. Each bump represents one carbon atom. As the tip moves from right to left, it bumps into an atom and gets stuck behind it. The scanner continues to move and lateral force builds up until the tip slips past the atom and sticks behind the next one.

2.3 Electronic Transport and Magnetoresistive Properties

The bulk samples, targets, thin films and hetrostructured studied during the preset work were characterized for their electrical and magneto transport properties by using the experimental techniques described below.

2.3.1 D.C. four-probe method

Transport property measurements of the manganite thin films were carried out using standard four –terminal method on a Quantum Design PPMS system [13]. The PPMS system can conduct the measurements in the temperature range of 1.9 - 350K. Temperature sweep capability allows measurements to be taken while sweeping the temperature at a user defined rate (0.01-6 K/min). Continuous low temperature control (CLTC) ensures precise temperature control. The PPMS has a superconductor magnet, which can provide a magnetic field up to 9 Tesla with the uniformity of 0.01% over a 5.5 cm×1cm diameter cylindrical volume. The low noise, bi-polar power supply allows continuous charging through zero field with current compensation and over-voltage protection. The resolution of the field control is 0.02 mTesla up to 9 Tesla. A schematic illustration of the PPMS probe is shown in Figure 2.6. Samples were mounted on removable platforms (see picture 2.4). A thermometer, in direct contact with the platform, accurately determines the sample temperature. The rotator can sweep the angular range from-10 ^{o}C to 370 ^{o}C , with the step size of 0.053° for standard resolution. A low contact resistance is desirable due to the small resistance of the samples. To fulfill this requirement, standard four-probe method was used for measuring resistance of the samples [14]. To measure the resistivity using this technique, the samples were cut in a rectangular bar shape using a diamond saw. For making electrical contacts of the probes

with the sample silver paint was used. Fine slurry of the silver paint was made by dissolving it with an appropriate solvent (n-butyl acetate or thinner). This silver paste was applied at the ends for current and voltage contacts. Due to very less resistance, thin copper wires were connected with silver paint as shown in fig.2.6 and the whole assembly was attached to a sample holder (see picture 2.4), where the wires were connected with leads to the measurement instruments. Such a sample holder is known as resistivity puck for measuring resistivity using a Physical Property Measurement System (PPMS).

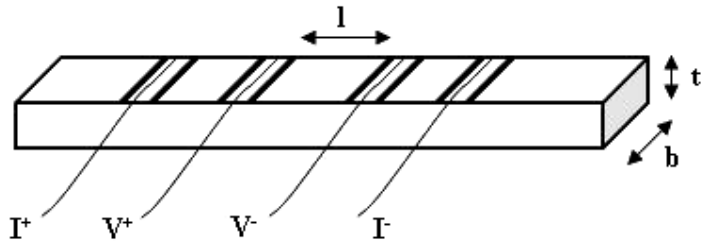

Figure 2.6: Four probe contacts used in the resistivity measurements.

Picture 2.4: Sample rotator with sample mounting platform (Reproduced from the Ref. 13).

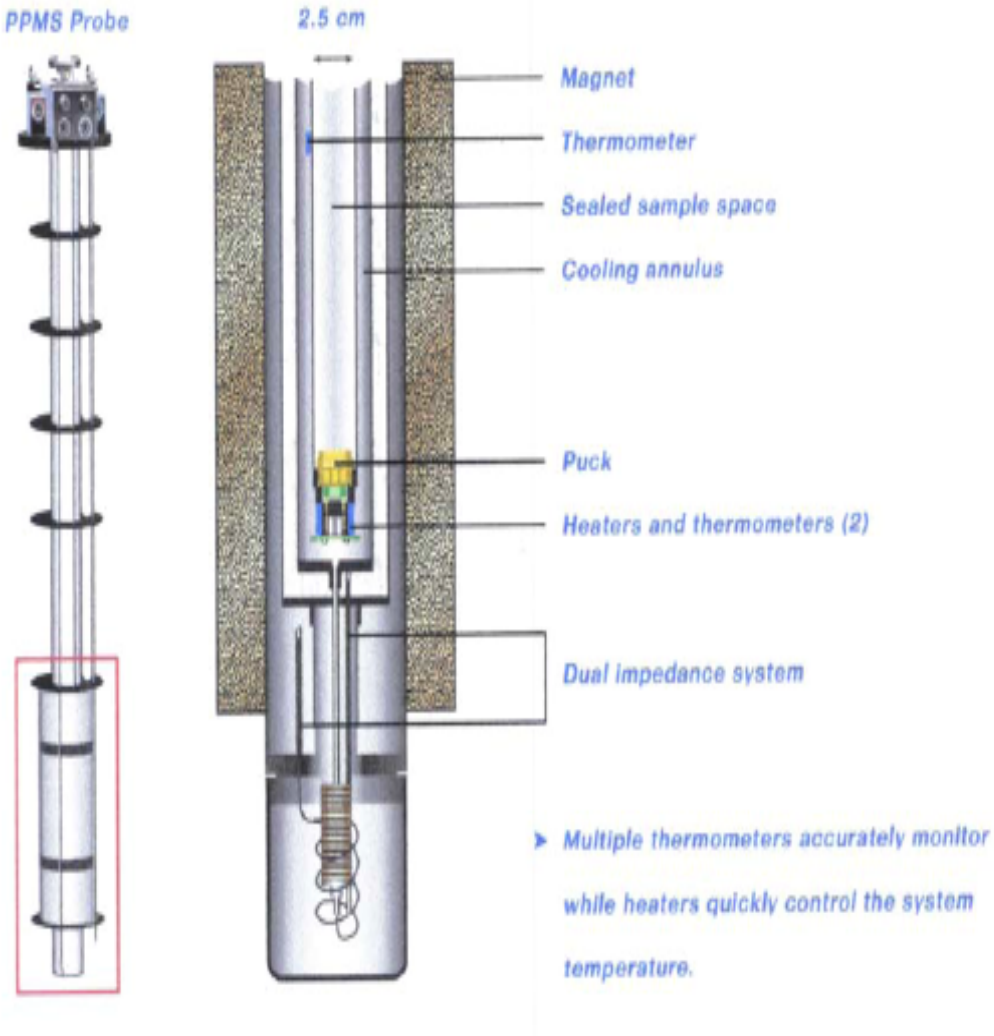

Figure 2.7: A schematic illustration of the PPMS 6000 probe
(Reproduced from the Ref. 13).

2.3.2 MR measurements (Low field and High field)

To study magneto resistive characteristics of the samples, resistance was measured by using the standard four probe method as explained in the previous section, in the presence of an external magnetic field in a Quantum Design Physical Property Measurement System (PPMS). At a constant applied field, resistance was measured as a function of temperature (magneto R-T) in the range of RT-5 K. All the manganite samples studied in the present work were characterized by using this technique.

2.4 Magnetic susceptibility and magnetization measurements

2.4.1 D.C. magnetization

Superconducting Quantum Interference Device (SQUID) magnetometer is the most powerful, sensitive and widely used instrument for magnetic characterization in material science [21]. This device works on the principal of quantum interference produced using Josephson junctions. This Josephson junction (sensor) mainly consists of the superconducting ring interpreted by a thin insulting film called weak link. The sensor and its pick up system is sensitive to change in the magnetic fluxes and thus to the change of the magnetization of magnetic material as a function of temperature, magnetic field and time. The SQUID has one or more Josephson junctions as its active element.

In most practical systems in use today, the SQUID is located inside a small cylindrical, superconducting magnetic shield in the middle of a liquid helium Dewar. The schematic diagram of the SQUID measurement probe is shown in the fig.2.8. Superconducting pickup coils, typically configured as gradiometers that detects the difference in one component of the field between two points, are located at the bottom of the Dewar, and are placed beneath the magnetometer. The rest of the hardware is designed to minimize helium boil off, eliminate rf interference, and avoid Johnson noise or any external distortion a. c. fields. If a constant biasing current is maintained in the SQUID device, the measured voltage oscillates according to the changes in phase at the two junctions, which depends upon the change in the magnetic flux. The flux change can be evaluated by counting the oscillations. It may be noted that the sensitivity of SQUID is 10^{-14} Tesla, which is incredibly large to measure any magnetic signal.

The above-mentioned measurement systems are used for d. c. magnetization and M versus H measurements of the samples. For d. c. magnetization a small external field is applied and χ is measured as a function of temperature at constant applied field. For M-H measurements, magnetization is measured at a constant temperature while magnetic filed is varied up to a certain value of positive and negative applied field. The most common units for the magnetic moment is emu. The natural unit of the magnetization is thus emu/g or emu/cm^3. If one can estimate the number of atom in the sample then one can also calculated the magnetic moment per atom in μ_B.

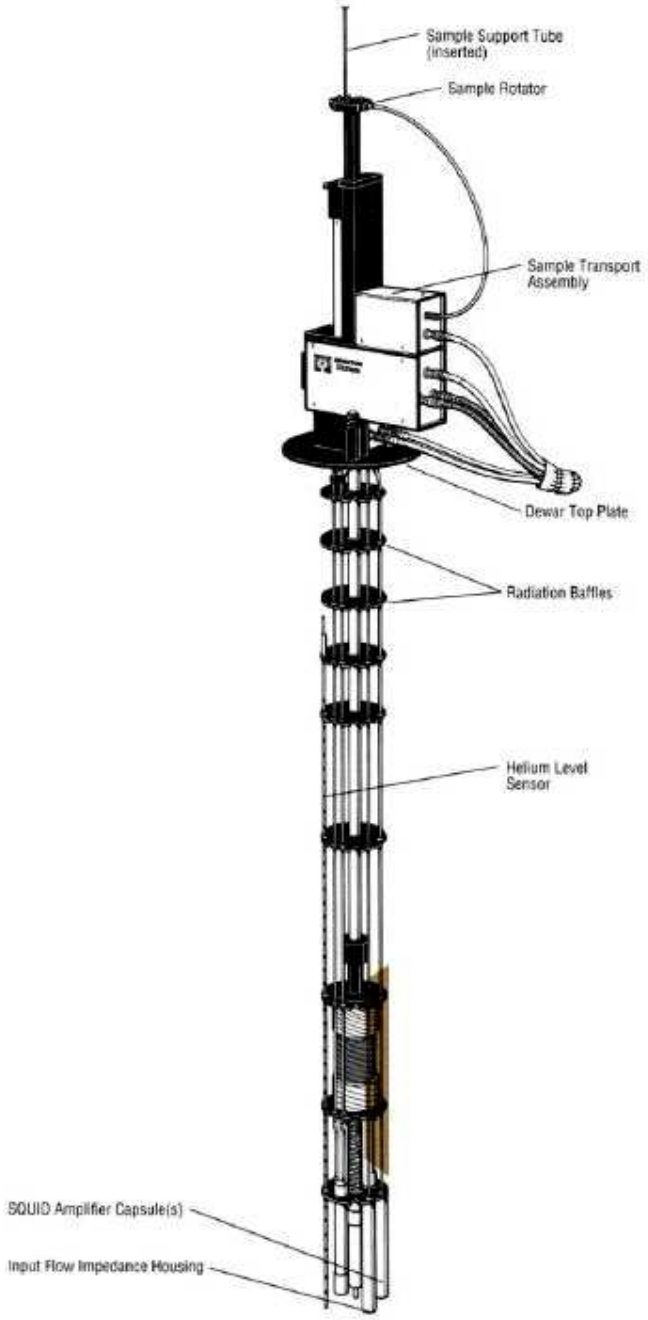

Figure 2.8: A schematic diagram of the SQUID sample measurement probe (Reproduced from the Ref. 15)

2.4.2 A.C susceptibility

In ac susceptibility (χ_{ac}) measurements the magnetization is probed by a small sinusoidal field of frequency f. The susceptibility measurement provides the information about the curie temperature (T_C), magnetic ordering in the materials.

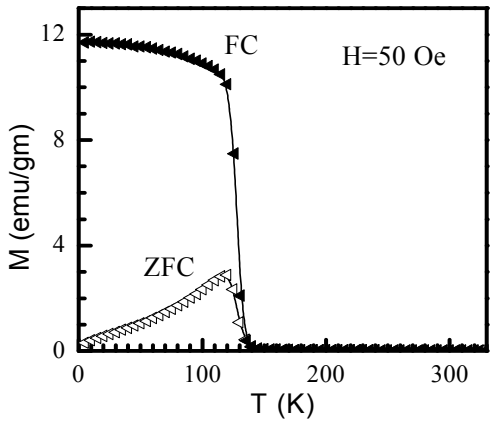

Figure 2.9: Temperature dependence of the FC and ZFC magnetization.

If a magnetic material get magnetized in the direction of the magnetic flux lines and shows a certain finite magnetic susceptibility (χ), which is defined as ratio of magnetization (M) to the applied magnetic field (H). The dynamic susceptibility has two components: one component is in-phase (χ') with the excitation while other one is a dissipative out of phase (χ'') component. Susceptibility can be measured on cooling or heating the sample.

REFERENCES

1. E. M. Engler

   Chem. Technol. **17** 542 (1987).

2. S. X. Dou, H.K. Liu, A.J. Bourdillon, J. P. Zhou, N.X. Tan, X.Y. Sun,

   C.C. Sorrell and J. Am.

   Ceram. Soc. **71C** 329 (1998).

3. C. J. Brinkered and G. W. Scherer

   "Sol-Gel Science" Academic Press Inc, Boston (1990).

4. D. B.Chrisery and G. K.Hubler

   " Pulsed Laser Deposition" Wiley-Interscience, New York, (1994).

5. Young Sun, M. B. Salamon and S. H. Chun

   J. Appl. Phys. **92** 3235 (2002).

6. B. D. Cullity, "X-ray Diffraction" Addison-Wesley, New York (1972).

7. C. Kittel ,"Introduction to Solid State Physics" New York, Plenum (1966).

8. A. Taylor, "X-ray Metallography" John Wiley & Sons (1961).

9. H. M. Rietveld, J. Appl. Cryst. **2** 65 (1969).

10. R. A. Young

    "The Rietveld Method" Oxford University Press Inc, New York (1993).

11. G. Binnig, C. F. Quate and Ch. Gerber

    Phys. Rev. Lett. **56(9)** 930 (1986).

12. G. Meyer and N. M. Amer, Appl. Phys. Lett. **57(20)** 2089 (1990).

13. PPMS manual by Quantum Design.

14. L. J. Vanderpauw

    Philips Res. Repts. **16** 187 (1961).

15. SQUID Magnetometer, Manual by Quantum Design.

Chapter - 3

3.1 Bulk and Pristine Thin film studies

In the recent years, renewed interest in the studies on manganite ceramics and their thin films has been accelerated due to the potential applications of these materials in bolometers, magnetic field sensors and computer read heads. Hole doped manganites of the type $RE_{1-x}A_xMnO_3$ (RE being rare earth ion and A divalent ion such as A=Ca, Sr, Ba and Pb) having perovskite structure are being revisited and their magnetoresistance (MR) properties have been studied in detail [1-3]. Alongwith the search for new materials which exhibit colossal magnetoresistance (CMR) effect under low applied fields, the research is also focused on synthesizing the manganites having insulator to metal transition (T_{IM}) and paramagnetic to ferromagnetic transition (T_C) above room temperature (RT). In order to achieve this, many groups have tried to substitute various types of dopants at A-site (RE, A) and B-site (Mn) in ABO_3 type $RE_{1-x}A_xMnO_3$ manganites [4-7]. Also several efforts are underway to enhance the MR by doping of small size cation at rare earth site and substitution of various magnetic and non-magnetic ions at Mn-site [8, 9]. This suggests that, physical properties of CMR materials strongly depend on the A-site cation mismatch or size variance. The two-manganite systems, which have been extensively studied, are, $La_{0.7}Ca_{0.3}MnO_3$ (LCMO) and $La_{0.7}Sr_{0.3}MnO_3$ (LSMO). LCMO is narrow bandwidth system having T_C and T_{IM} much below RT with large MR while LSMO is a large bandwidth system having T_C and T_{IM} above the RT with low MR.

Studies on the LSMO system are carried out in the present work, on the epitaxial films and multilayered structures in the context of enhancement in their MR behaviour near RT in low applied field. Our main interest in studying the Pr doped $La_{0.7}Sr_{0.3}MnO_3$ (LSMO) based manganite system is to study the effect of size variance ($\sigma^2 \sim 0.00249$) due to substitution of La by Pr in this system. It has been reported that, for the LSMO thin films, electronic transport and magnetic properties of the system are extremely sensitive to strain at the interface of the film and substrate [10, 11]. This has been attributed to the lattice mismatch between the film and the substrate, oxygen deficiency, deposition parameters like substrate to target distance, substrate temperature and oxygen partial pressure, etc. [12-14]. Grain boundary effect and the lattice strain effect are two factors, which are shown to create significant differences between the bulk and thin film

properties [15]. It has also been reported that, the small distortion in the Mn-O-Mn bond angle or bond length changes the transport and magnetotransport properties significantly [16, 17]. The Mn-O-Mn bond angles are highly affected by the strain which, amongst others, can also be produced due to the lattice mismatch between the single crystal substrate and sample film and hence due to substitution of the ion at M site. In present case, effect of replacing La by Pr^{+3} which increases the A-site size mismatch, results in a large MR ~ 55% at RT.

From application point of view, one of the interesting characteristics of manganites is its half – metallic ground state [18]. In the ground state, conduction electrons are perfectly spin polarized due to the strong Hund's coupling between localized t_{2g} spins and itinerant e_g electrons [19]. This half metallic nature of manganites is widely used to understand various properties like spin valve mechanism and spin polarized current [20]. We have fitted the observed R-T data of $La_{0.5}Pr_{0.2}Sr_{0.3}MnO_3$ (LPSMO) thin films in magnon scattering laws in which one-magnon scattering type of behavior is useful as an important test for half metallic behavior [21]. The results obtained on the studies on the structural, transport and magnetotransport properties of LPSMO thin films have been discussed in the context of cationic size disorder and substrate induced strain effects.

Synthesis

Polycrystalline bulk target sample of LPSMO was synthesized by using standard ceramic method. Dried powders of La_2O_3, Pr_6O_{11}, $SrCO_3$, and MnO_2 (all > 99.9% pure) were mixed in stoichiometric proportions and calcined at 950°C for 24 hours. The mixture was then ground, palletized and sintered in the temperature range of 1100°C - 1400°C with several intermediate grindings. The final well-sintered 15mm diameter pellet was used as a target for the deposition of single crystalline epitaxial thin films of LPSMO using Pulsed Laser Deposition (PLD) technique. Third harmonic (355 nm) of a Q-switched Nd: YAG laser (6 ns) having energy density of about 2.17 J/cm^2 at 10 Hz repetition rate was used for the ablation. Polished (*h00*) $SrTiO_3$ (STO) and $LaAlO_3$ (LAO) single crystal substrates were placed in front of the target at a distance of 5.5 cm and heated to 740^{o}C. The chamber was first pumped down to 10^{-5} bar. The laser deposition process was carried out at in an oxygen partial pressure of 400 mTorr. The

deposited films were having thickness of 50nm and 150nm. Various deposition parameters used are summarized in the Table 3.1.

Table 3.1: Thin films deposition parameters.

Laser used	Q-switched Nd: YAG
Laser frequency	10 Hz
Laser Energy	2.17 J/cm^2
Pulse width	6 ns
Substrate to target distance	5.5 cm
Substrate heater temperature	740°C
Oxygen partial pressure	400 mTorr
Target used	$La_{0.5}Pr_{0.2}Sr_{0.3}MnO_3$
	(Diameter – 15mm, thickness – 2mm)
Substrate used	Single crystal $SrTiO_3$ (*h00*) &
	$LaAlO_3$ (*h00*)

The structure of the samples was analyzed using X-ray diffraction (XRD) and surface morphology was studied using Atomic Force Microscopy (AFM). The resistivity was measured as a function of temperature in range of 5K-320K and as a function of magnetic field recorded as 0T - 9T - (-9T) - 0T using PPMS facility at TIFR, Mumbai.

3.1.1 Structure and Surface morphology

3.1.1(A) Structure

Structural refinement was carried out by rietveld fitting of the XRD patterns using standard FULLPROF programme [22]. Figure 3.1 shows the rietveld refined XRD pattern of the bulk polycrystalline LPSMO target showing that there is a good agreement between fitted and experimental patterns. The analysis reveals that, sample crystallizes in a distorted orthorhombic structure (space group: *Pnma*, no. 62) with the refined cell parameters namely, a = 5.512(3) Å, b = 7.791(2) Å and c = 5.548(2) Å.

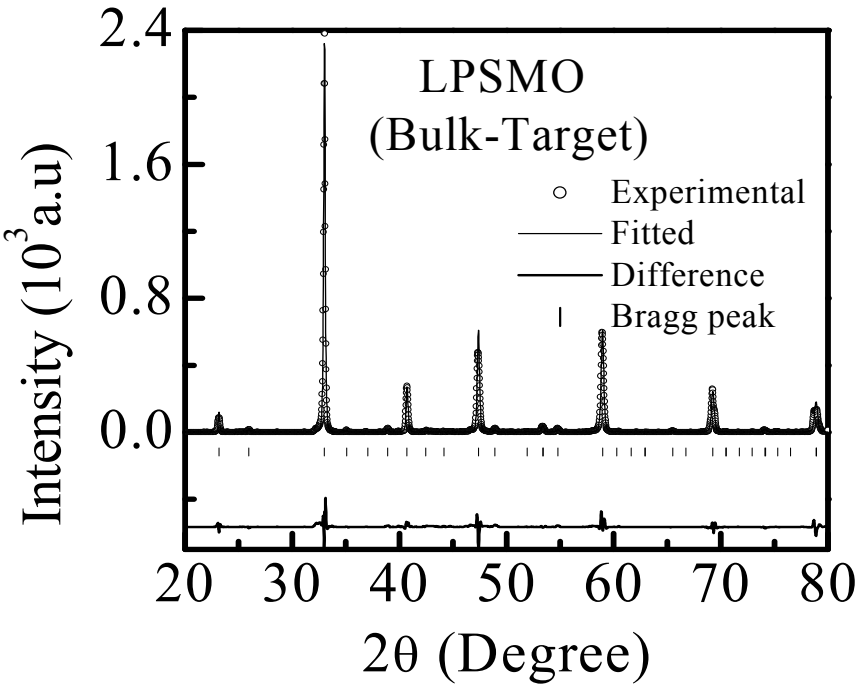

Figure 3.1: A typical rietveld fitted XRD pattern of LPSMO bulk target.

Structural characterization was carried out on all the LPSMO films by analyzing the XRD patterns obtained. X-ray diffraction patterns of 50 and 150nm LPSMO thin films deposited on the STO and LAO substrates are shown in figs 3.2. (A) & (B) and 3.3.(A & B), respectively. It can be seen from the figures that, all the films exhibit only the (*0k0*) family of XRD peaks, suggesting the epitaxial growth of the films. Figure 3.4 shows the XRD patterns of 150nm LPSMO films on the STO and LAO substrates in the log scale, to ensure that the there is no any impurity phase present in the samples. The influence of substrate strain is the main factor distinguishing manganite films from bulk manganite samples. The strain affects the properties of the manganite thin films. Consequently, to obtain and improve the desired properties, one needs to correctly understand the effects of the strain on the manganite thin films [23, 24].

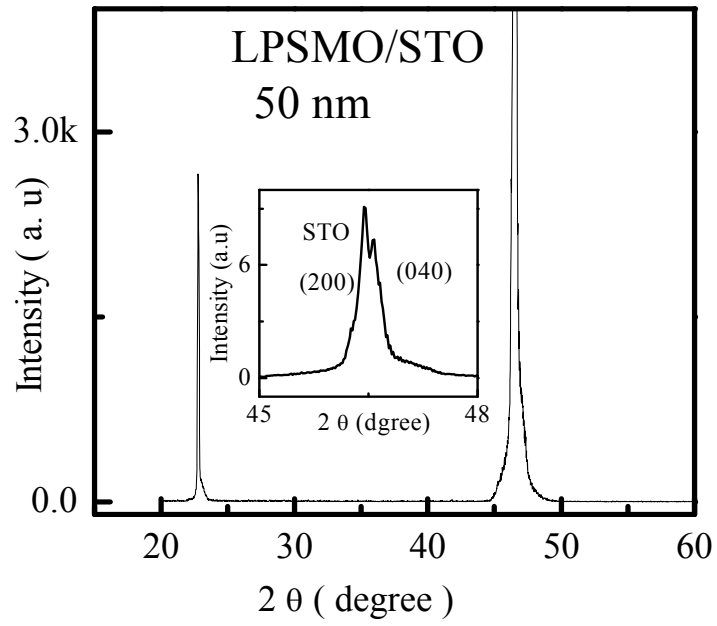

Figure 3.2. (A): A typical XRD pattern of 50nm LPSMO/STO film.

(Inset of the figure shows the enlarged view of *040* peak).

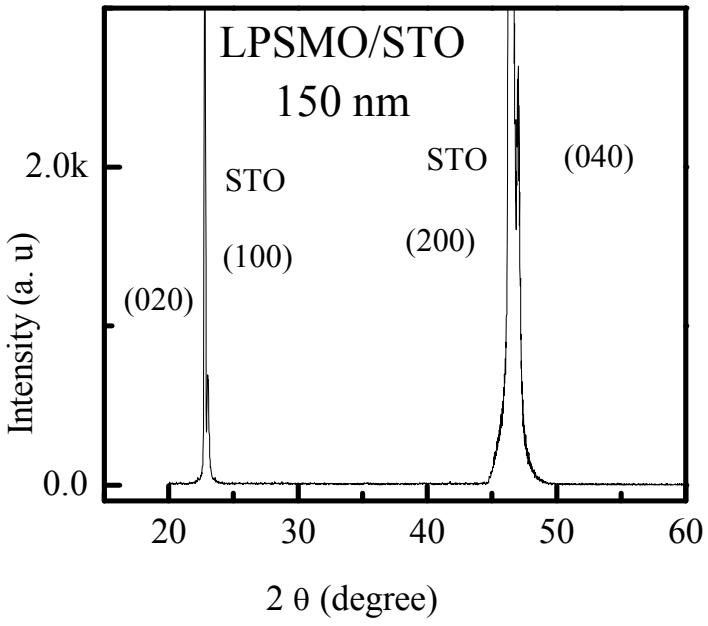

Figure 3.2. (B): A typical XRD pattern of 150nm LPSMO/STO film.

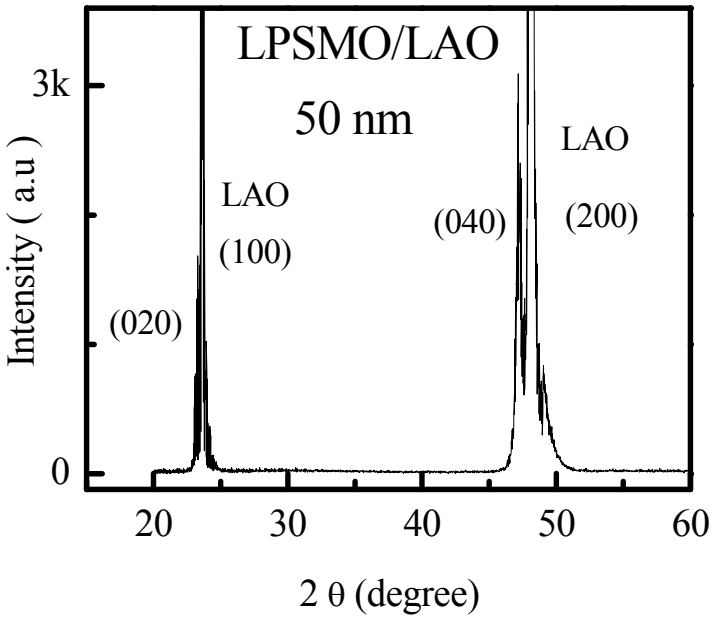

Figure 3.3. (A): A typical XRD pattern of 50nm LPSMO/LAO film.

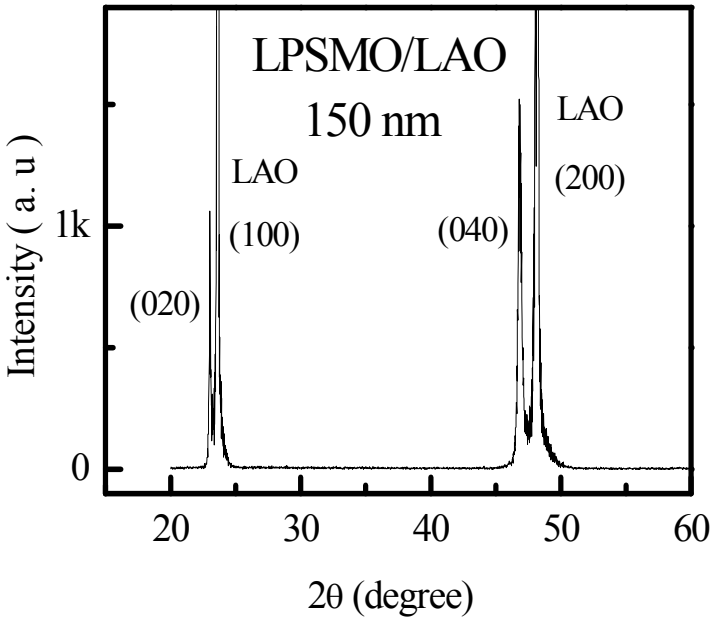

Figure 3.3. (B): A typical XRD pattern of 150nm LPSMO/LAO film.

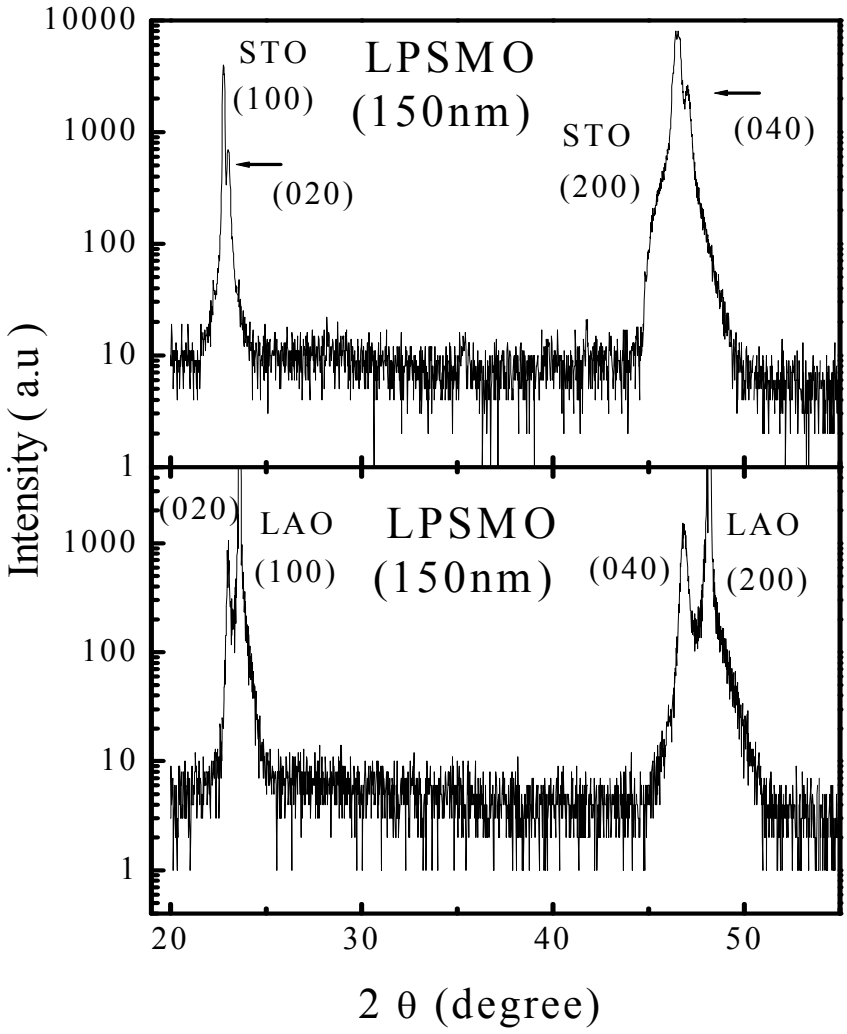

Figure 3.4: XRD patterns (plotted in log scale) for the 150 nm LPSMO thin films on the STO and LAO substrates.

The lattice mismatch or strain in film at the interface was calculated using the formula,

$$\delta = \frac{d_{substrate} - d_{thin\ film}}{d_{substrate}} \times 100 \qquad \text{.....(1)}$$

Positive values of the mismatch correspond to the tensile strain whereas negative values describe compressive stress (for details, see chapter - 4). In the LPSMO films, use of STO substrate results into the tensile strain while LAO substrate produces the compressive strain on the film. The Positive values of mismatch representing the tensile

strain in LPSMO/STO films are ~ 1.00 % for 50nm and ~ 0.80 % for 150nm films. Negative values of the mismatch corresponding to the compressive strain in LPSMO/LAO films are ~ -2.56 % and -2.04 % for the 50nm and 150nm films, respectively. In both the sets of films, mismatch is reduced with film thickness indicating the release of strain with thickness [11].

3.1.1(B) Surface morphology

The surface morphology of all the LPSMO films was studied using the AFM measurements. The pictures 3.1 and 3.2 show the surface topology of the 50nm and 150nm LPSMO/STO films. The surface roughness analysis of both the film surfaces shows the RMS roughness ~ 1.048 & 1.970nm for 50 & 150nm films respectively (picture 3.1 & 3.2). In the similar manner pictures 3.3 and 3.4 show the topology of the 50nm and 150nm LPSMO/LAO films having RMS roughness of the ~1.084 nm and ~3.501 nm respectively. AFM images clearly indicate that, STO & LAO substrate have a large influence on the surface morphology. LPSMO films deposited on the STO substrate possess small grains as compared to films deposited on the LAO substrate. Also the LPSMO/LAO films have better grain connectivity as compared to LPSMO/STO films. From the comparison of surfaces of 50nm and 150nm LPSMO/LAO films, it can be clearly observed that, in the 150nm film, grain size is very large as compared to grain size of the 50nm film.

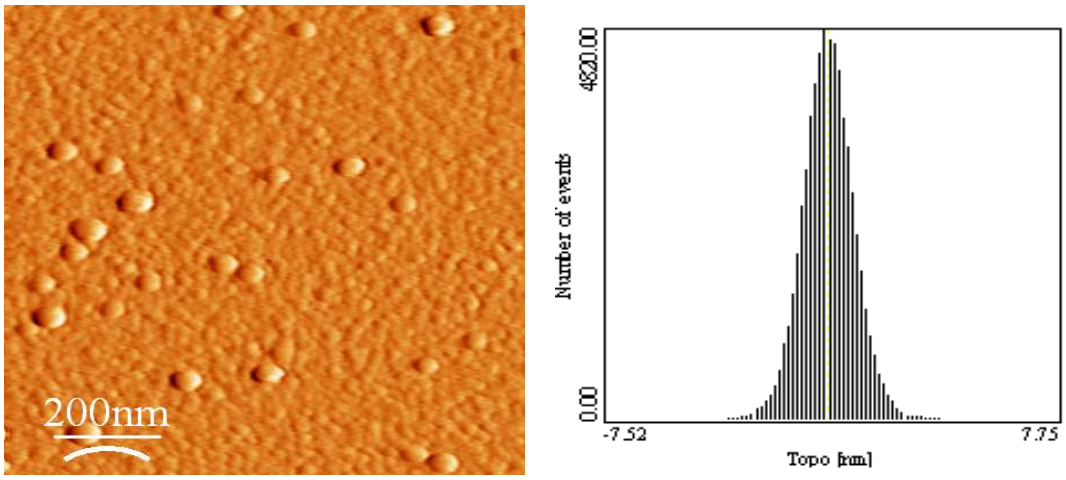

Picture 3.1: 2D AFM images and histogram for the roughness analysis of the 50nm LPSMO/STO thin film.

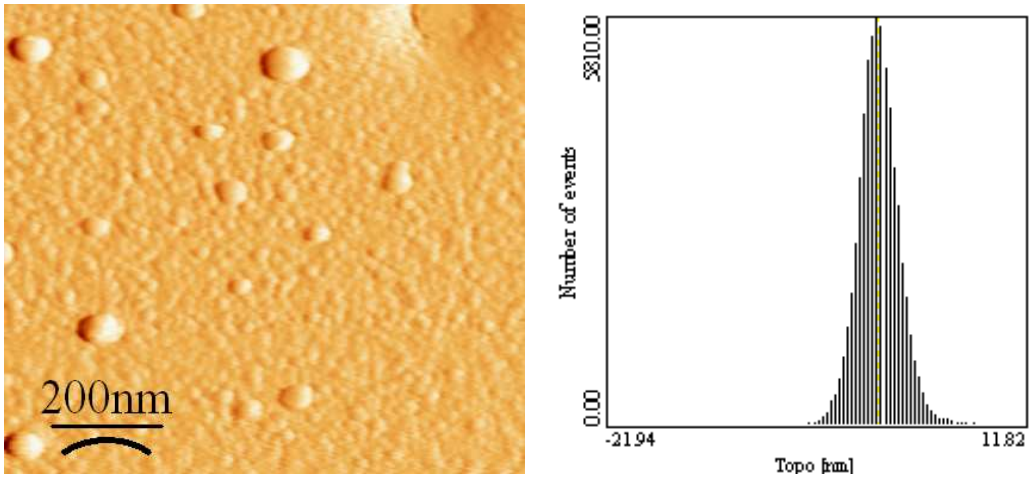

Picture 3.2: 2D AFM images and histogram for the roughness analysis of the 150nm LPSMO/STO thin film.

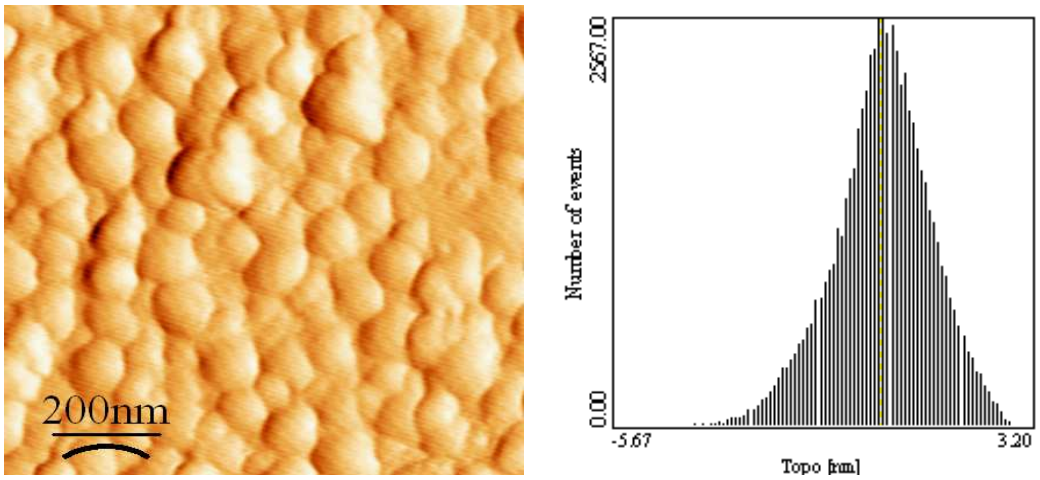

Picture 3.3: 2D AFM images and histogram for the roughness analysis of the 50nm LPSMO/LAO thin film.

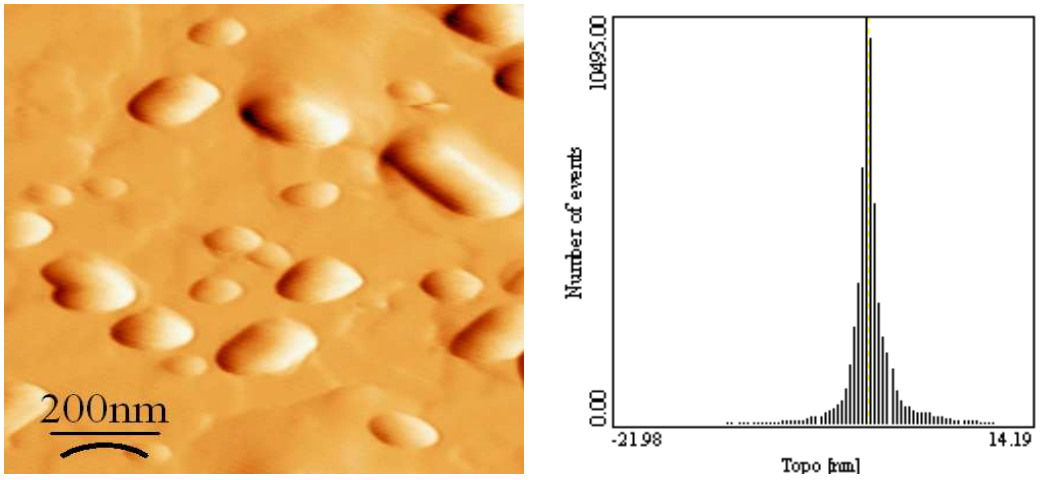

Picture 3.4: 2D AFM images and histogram for the roughness analysis of the 150nm LPSMO/LAO thin film.

3.1.2: Electrical resistivity and magnetoresistance

3.1.2(A): Electrical resistivity

Figures 3.5 and 3.6 display the resistivity (ρ) versus temperature (T) plots for the 50 and 150nm LPSMO films on the STO and LAO substrates respectively, in the temperature range 5-350 K under 0-5T applied fields. It can be seen from the plots that, LPSMO/STO films exhibit T_{IM} ~ 295 K for 50nm and 328 K in 150nm film under 0 T field.

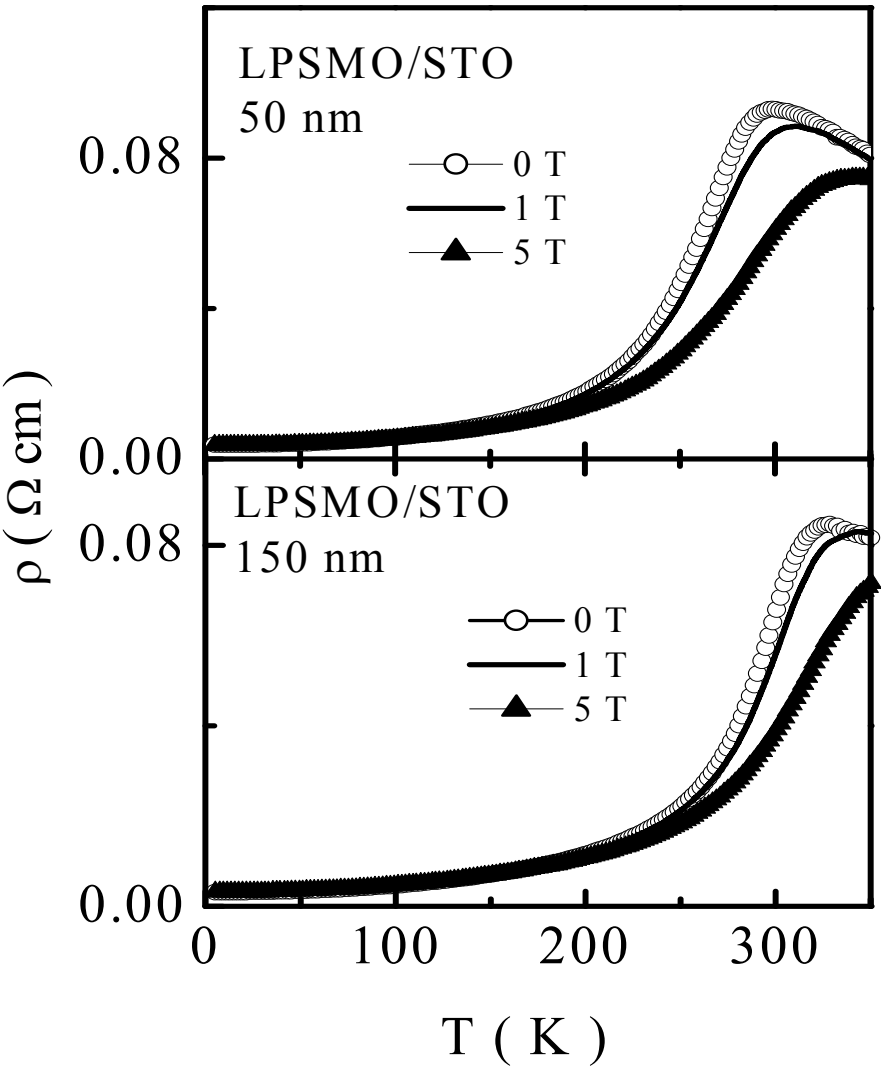

Figure 3.5: Resistivity vs. temperature plots of the 50 & 150nm LPSMO/STO films.

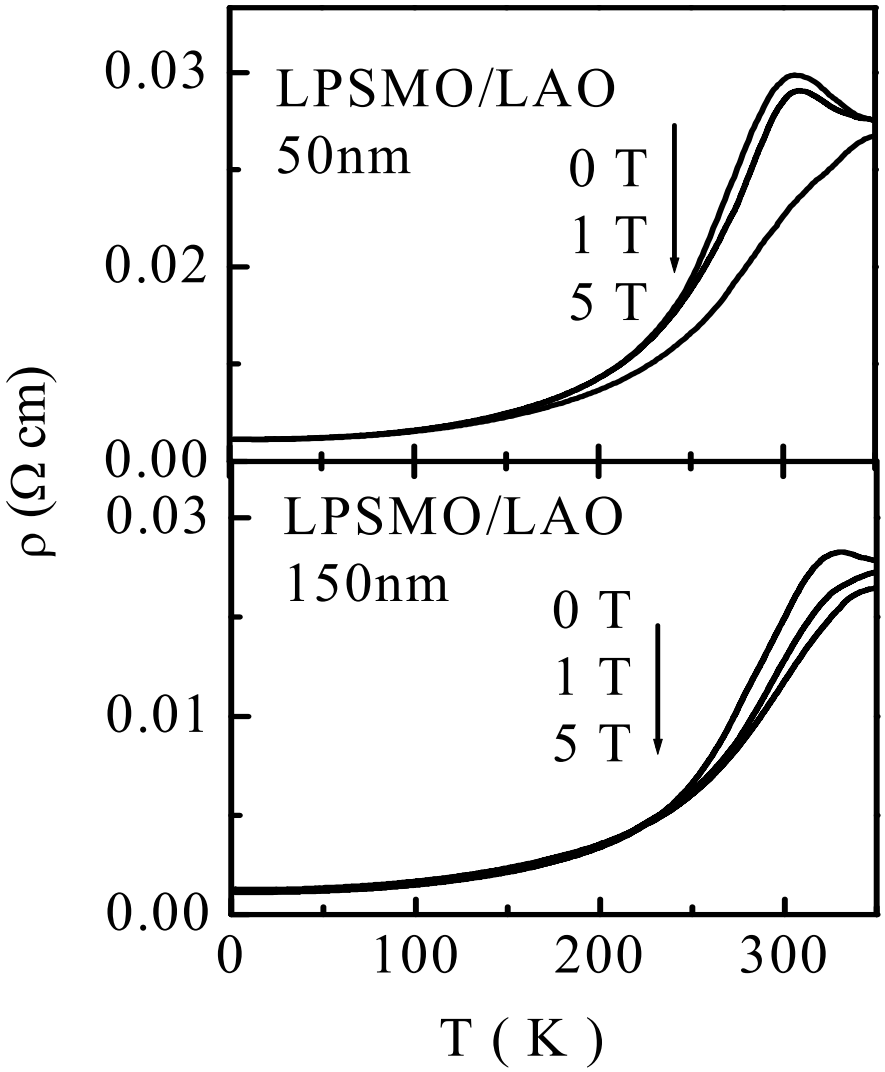

Figure 3.6: Resistivity vs. temperature plots of the 50 & 150nm LPSMO/LAO films.

The LPSMO/LAO films exhibit T_{IM} ~ 308K for 50nm and ~328K for 150nm under 0T field. The degree of epitaxial strain on the lattice due to STO and LAO substrates in LPSMO films is expected to decrease with film thickness resulting in the higher T_{IM} in the thicker films as compared to the lower thickness films [25]. Here it also notable that resistivity of the LPSMO/LAO films is lower than that of the LPSMO/STO films while the T_{IM} value is higher as compared to that of LPSMO/STO films. This effect may be due to the different substrate induced strain such as tensile strain in case of STO substrate and compressive strain in the LAO substrate. An interesting aspect in ρ - T plots, with and without applied field is that, resistivity follows the same path in both the

cases below 200 K (Figs. 3.5 and 3.6) which indicates that, without any applied field, spins are fully polarized and all the films have T_{IM} in the vicinity of the RT. Table 3.2 lists the values of T_{IM} (at 0T) and strain values calculated for both the sets of LPSMO films.

Table 3.2: Values of T_{IM} (at 0T) and δ for 50& 150nm LPSMO films on STO & LAO.

Thin film	**Substrate**	**Thickness (δ)**	**Mismatch**	**T_{IM} (0T)**
LPSMO	STO	50nm	1.00%	295K
LPSMO	STO	150nm	0.80%	328K
LPSMO	LAO	50nm	-2.56%	308K
LPSMO	LAO	150nm	-2.04%	328K

3.1.2(A)-1: Low temperature resistivity (Magnon Scattering)

It is well known that the resistivity behaviour in the metallic region can be explained by electron-electron, electron-phonon and electron-magnon inelastic scattering mechanisms. To understand the ρ - T behavior and the underlying mechanism in detail, below the 200 K in metallic region, all the ρ - T curves of the films studied during this work were fitted using the equation, $\rho(T) = \rho_0 + BT^n$ …… (2)

where, B is electron-magnon coefficient for corresponding scattering mechanism, ρ_0 is residual resistivity of the sample, which is due to the contribution from various defects, domains, grain boundaries and other temperature – independent scattering processes and n is free parameter. If n = 2, the resistivity obeys electron-electron scattering, n = 2.5 suggests that one magnon behavior is exhibited, n = 3 shows the unconventional one-magnon scattering, whereas n = 4.5 and 7.5 correspond to two magnon scattering phenomenon [18, 21, 25-28]. Typical values of the residual resistivity (ρ_0) are always less than 4×10^{-3} Ω cm, which can be considered as a check for the high quality of the samples.

To understand the low temperature resistivity behaviour in the case of CMR manganite, various researchers have reported different scattering mechanisms having n values ranging from 2-7.5, which are summarized as below. M. B. Salmon et al have shown that the T^2 dependence of resistivity usually ascribed to the electron - electron scattering [25]. Kubo and Ohata et al have shown that resistivity varies as $T^{2.5}$ due to minimal contribution from single magnon scattering [26], the proposition corrected by Xindong Wang and X.-G. Zhang suggesting that Anderson localization allows a nearly half-metallic ferromagnet to behave like a true half-metallic ferromagnet which shows that only majority spin channel carries the current and single magnon scattering leads to a $T^{2.5}$ temperature dependence of the resistivity has a significant contribution [27]. Nobuo Furukawa suggested that T^3 dependence of resistivity (unconventional one-magnon scattering) is a crucial test for the search of half metallic behaviour in LSMO [18, 21, 28]. Two magnon scattering leading to $T^{4.5}$ and $T^{7.5}$ type temperature dependences has been suggested by Kubo and Ohata et al in which magnon processes are exponentially suppressed by a factor $\exp(-E_g/K_BT)$, where Eg is the minority spin band gap at the Fermi energy.

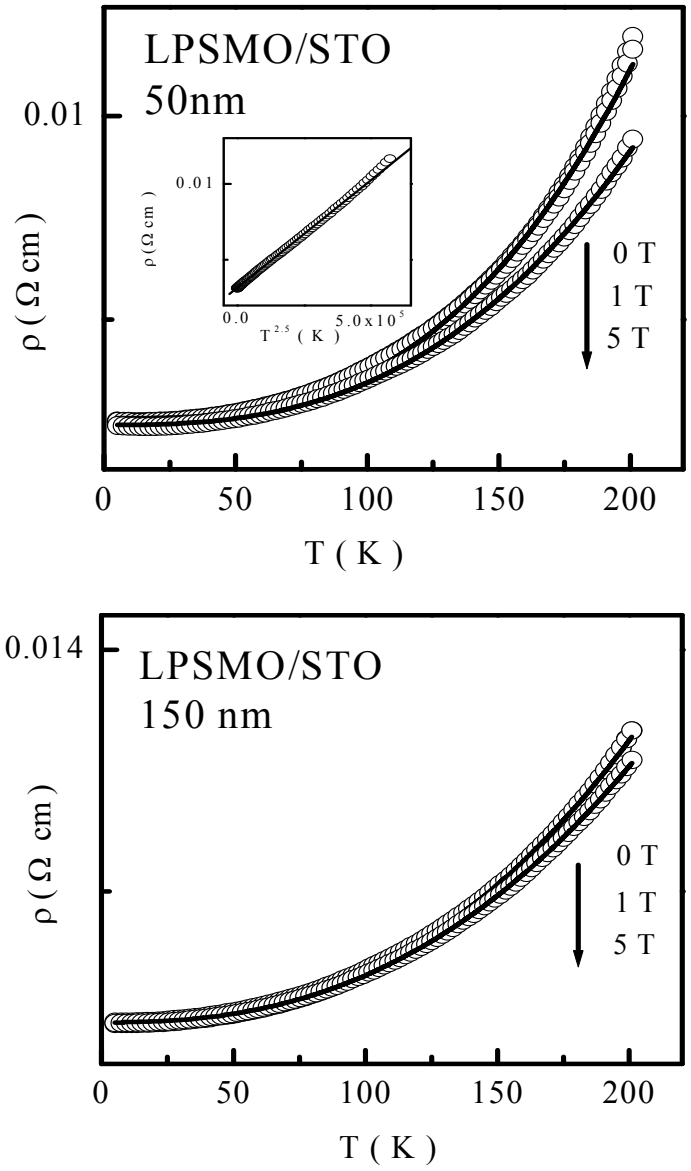

Figure 3.7: Low-temperature resistivity fits to magnon-scattering law for 50 & 150nm LPSMO/STO thin films. The symbols are the experimental data points and the solid curves are the theoretical fits.

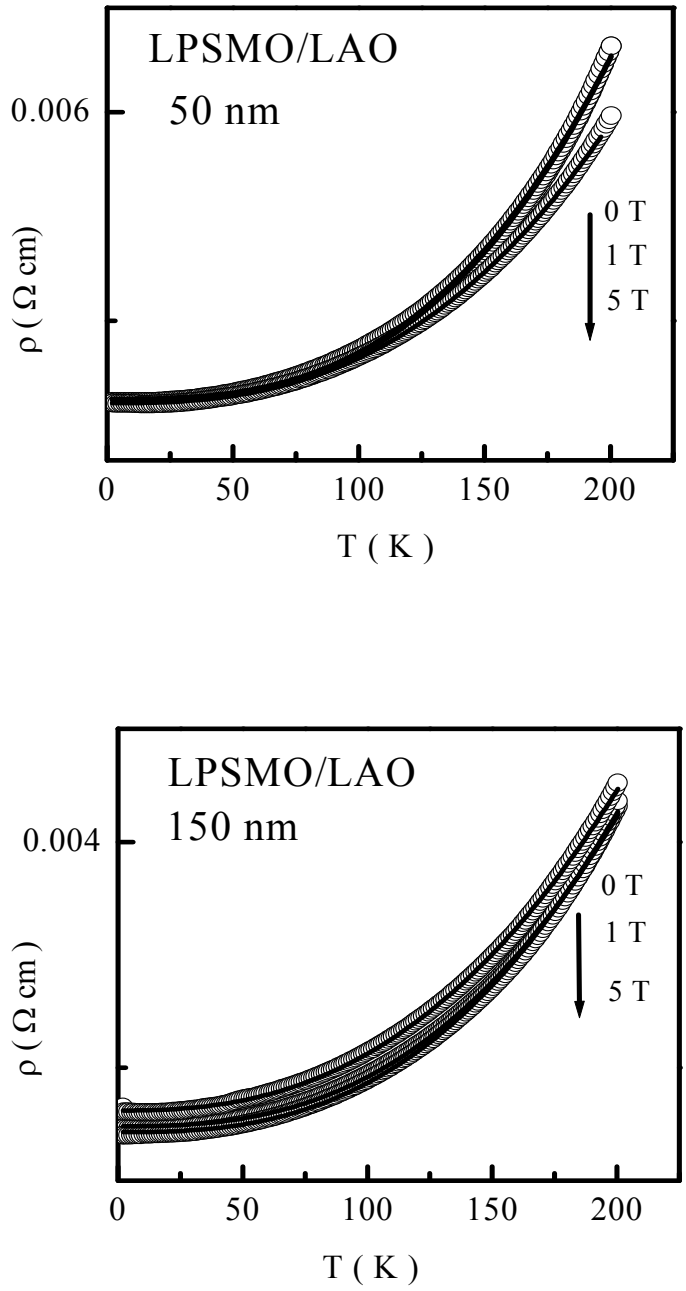

Figure 3.8: Low-temperature resistivity fits to magnon-scattering law for 50&150nm LPSMO/LAO thin films. The symbols are the experimental data points and the solid curves are the theoretical fits.

Figures 3.7 and 3.8 depict the low temperature ρ - T fits to eqn. (2) for 50 nm and 150 nm LPSMO films on the STO and LAO substrates respectively, with and without field. Table 3.3 lists the values of various parameters derived from fitting the equation (2). It can be seen from figs 3.7, 3.8 & Table-3.3 that, n value varies between $2 \leq n \leq 3$ with good fitting, which shows that at low temperature resistivity is mainly due to magnon carrier scattering. In the present studies we have fitted the ρ - T data in broad low temperature range of 5 – 200 K. From Table-3.3, it can be seen that, the $\rho_0 \sim 2$ - 4 mΩcm suggesting good quality of films.

TABLE 3.3: Values of applied fields, coefficients of the fit to equation (2) and the normalized χ^2 for 50 and 100nm LPSMO films.

Film thickness	**(H) (Tesla)**	**σ_0 (Ωcm)**	**B × 10^{-9}**	**n**	**χ^2 × 10^{-9}**
	LPSMO/STO				
50nm	0	0.0039	1.40	3.00	20.9
	1	0.0038	2.00	2.90	20.3
	5	0.0036	5.30	2.30	6.70
150nm	0	0.0032	9.03	2.40	2.60
	1	0.0032	1.25	2.30	2.50
	5	0.0032	1.72	2.31	07.4
	LPSMO/LAO				
50nm	0	0.00187	0.91	2.50	1.92
	1	0.00188	1.18	2.87	1.52
	5	0.00182	3.49	2.63	30.0
150nm	0	0.00148	2.13	2.65	41.0
	1	0.00143	1.77	2.69	57.5
	5	0.00162	5.13	2.49	27.8

We report for the first time, the observation of half metallic behavior in 50nm LPSMO/STO thin films in broad temperature range of 5-200K where in ρ - T obeys unconventional one-magnon scattering law ($\rho \propto T^3$; n=3). N. Furukawa et al has reported the half metallic nature ($\rho \propto T^3$) in the $La_{1-x}Sr_xMnO_3$ and $Sm_{0.6}Sr_{0.4}MnO_3$ bulk samples in the temperature range up to 50 K [18]. The 150nm LPSMO/STO films exhibit $T^{2.5}$ type resistivity dependence, suggesting one-magnon scattering mechanism responsible for charge conduction. The 50 & 150nm LPSMO/LAO films obey the one-magnon scattering behaviour up to temperature range up to 200K (Table 3.2). These observations on the ρ(T) behaviour of LPSMO/STO & LPSMO/LAO films, supports the argument that, resistivity in these films has no contribution from grain diffusion. As observed by Gupta et al., even grains of the order of 10 μm have strong effects on both ρ_0 and ρ(T) at low temperatures [29]. In fact, due to the diffusion at grain surface, the ρ_0 becomes higher and the behavior of ρ changes as a function of temperature, as described above. In our case, ρ_0 is in the order of mΩ and hence this reason is ruled out for the anomalous magnon scattering behaviour. Two possibilities exist, which are responsible for magnon scattering in the LPSMO films, namely, substrate induced strain and another is A-site size variance. We have deposited LPSMO films on both the STO & LAO substrates resulting into different strains, namely compressive and tensile. In both the sets of films the magnon scattering is explained. Hence we can say that, it is the intrinsic property of the material and the reason behind observation of such behavior may be attributed to the Pr^{+3} substitution at A-site, which induces A-site size variance in broadband LSMO system and change the Mn-O-Mn bond angle, thereby preventing the overlapping between Mn e_g and O_{2p} orbitals, resulting the half metallic behavior in large temperature range 5 – 200 K. Such behavior is absent in pristine LSMO system in the low temperature range [21].

3.1.2(B) Magnetoresistance

In the manganites, magnetoresistance (MR%) is calculated as MR % = $(\rho_0 - \rho_H)/\rho_0 \times 100$ %, where ρ_H and ρ_0 are the resistivities with and without fields. The MR behaviour can be studied in two regions, namely, Low Field Magnetoresistance (LFMR) and High Field Magnetoresistance (HFMR) [30, 31]. The origin of LFMR is due to spin-polarized tunneling through insulating grain boundary (GB), while HFMR is ascribed to the reorientation of disordered spins at interfaces in high field. The GB effect plays an important role in the MR behaviour of the polycrystalline sample while it is absent in the epitaxial thin film.

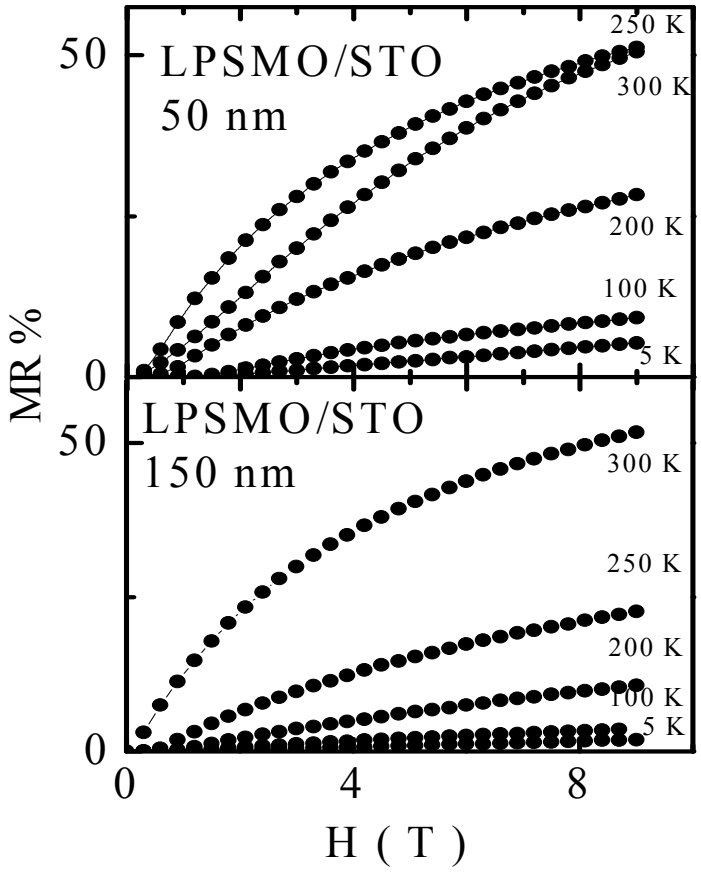

Figure 3.9: MR vs. H (T) behavior of 50nm & 150nm LPSMO/STO films at different temperatures.

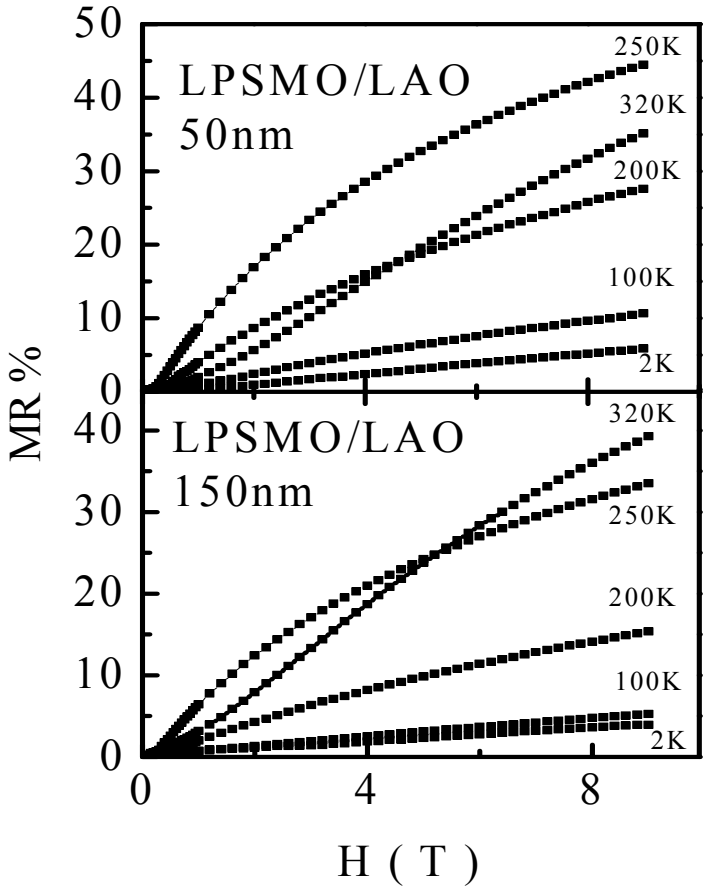

Figure 3.10: MR vs. H (T) behavior of 50nm and 150nm LPSMO/LAO films.

Figures 3.9 and 3.10 show the magnetoresistance behavior of 50&150nm LPSMO films on STO & LAO substrate in 0-9T applied fields. The 150nm LPSMO/STO film exhibit MR ~ 51 % at 300K while MR ~ 50 % is observed in 50nm film at 300K (near the T_{IM}). In the LPSMO/LAO films, the MR ~ 45 % at 250K (50nm) and 40 % at 320K (150nm) (near T_{IM}) has been observed. All the LPSMO thin films studied shows the large MR in the vicinity of the RT as compared to other manganite films which can be attributed to the large A-site size disorder resulting into structural distortions and hence magnetic disorder at Mn-O- Mn bond. It can be clearly seen from above curves that maximum, MR% is observed at 250K in the 50nm while in 150nm film, it is observed at 300K (Fig. 3.9). A similar MR behaviour is observed in LPSMO/LAO films, which supports the thickness dependent strain effect in manganite film. Also, the MR% in LPSMO/STO film is higher as compared to LPSMO/LAO films which points towards the role of substrate in the producing the strain and growth

morphology of film. The presence of larger strain in LPSMO/STO films, results in the disorder in the dead layer thereby increasing resistivity which on application of field gets suppressed appreciably resulting in higher MR.

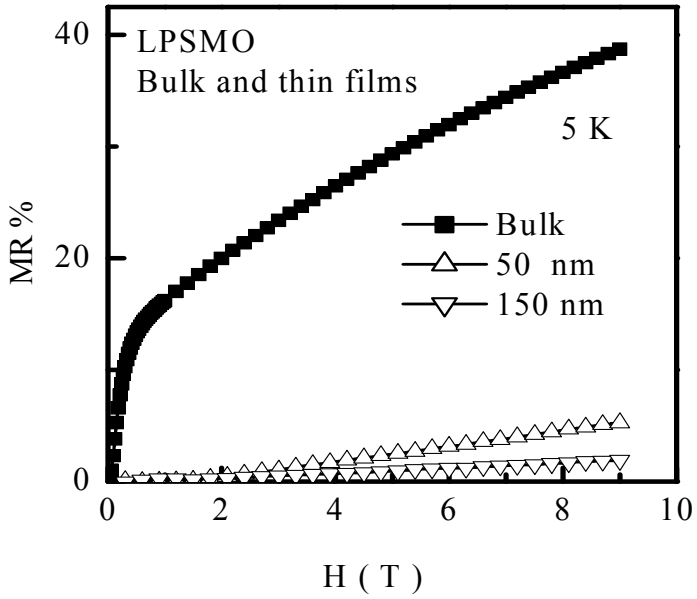

Figure 3.11: MR vs. H (T) behavior of bulk and LPSMO/STO thin films with the thickness of 50nm and 150nm.

Figure 3.11 shows the comparison of MR behaviour of the bulk and LPSMO/STO films (50nm & 150nm) at 5K. At low temperature, in the bulk sample, LFMR (<1 T) of MR ~ 17% is exhibited while thin films exhibit negligible LFMR (< 1%). This large disparity in the LFMR of the bulk and films confirms the good quality and high epitaxial growth of thin films having no grain boundary effects. Another notable feature which can be seen from LFMR curves is that with increase in field (0-9T) the MR does not change appreciably in the LPSMO/STO films, which shows that, at low temperatures the spins are fully polarized.

3.1.3 TCR and FCR studies

Uncooled infrared imaging systems based on microbolometers offers the possibility for the development of a light weight, inexpensive alternative for complex, cooled IR imagining systems based on the HgCdTe (MCT) or InSb [32]. The sensitivity of presently used microbolometer based systems is one order of magnitude lower than

that of semiconducting systems. The active element in the microbolometer based detector is an oxide-coated silicon micro-bridge. The oxide film has a temperature-dependent resistance. Heating of the micro-bridge by the incident IR radiation is detected by a change in the micro bridge resistivity. Present day microbolometer-based systems use V_xO_y which has a reported temperature coefficient of resistance (TCR) of – 2 $\%K^{-1}$ at RT [33]. The discovery of new materials with higher TCR would increase the sensitivity of the microbolometers comparable with MCT detectors.

3.1.3 (a) TCR studies

The value of the temperature coefficient of resistance (TCR) is very useful for device application, which can be calculated as:

$$TCR(\%) = \frac{1}{R}\frac{dR}{dT} \times 100\, K^{-1} \quad \text{.....} \quad (3)$$

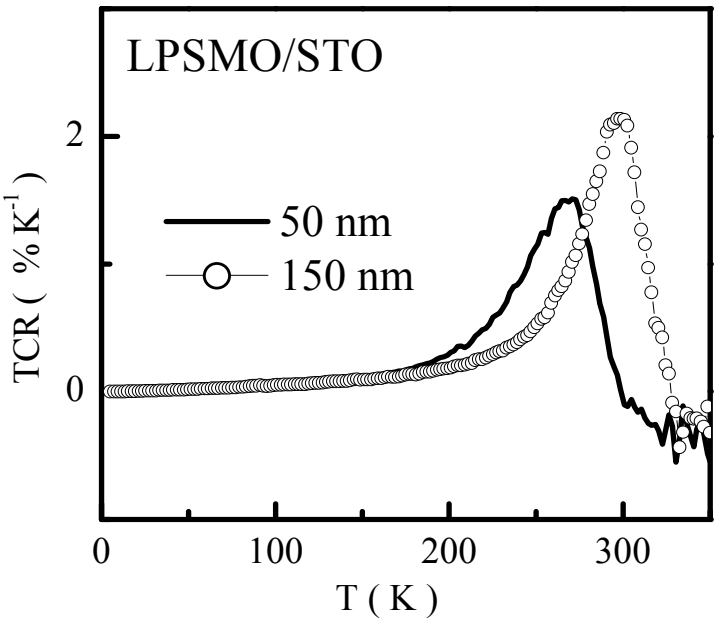

Figure 3.12. (A): Temperature coefficient of resistance of the 50nm and 150nm LPSMO/STO films.

The variation of TCR with temperature for 50nm & 150nm LPSMO/STO and LPSMO/LAO films has been shown in figs 3.12. (A) & (B). Table 3.4 lists the values of maximum positive and negative TCR for both the sets of films. 150nm LPSMO/STO film exhibit the maximum positive TCR ~ 2.14$\%K^{-1}$ (at 300K) and maximum negative TCR values are ~ -0.29$\%K^{-1}$ at 332K. While 50nm LPSMO/LAO film shows the maximum positive TCR value ~1.20$\%K^{-1}$ at 274K and maximum negative TCR ~ -0.42

$\%K^{-1}$ at 326K. Thus, LPSMO films shows the maximum negative and positive TCR values in the vicinity of the RT enabling them to be used as resistance sensor with low noise values as compared to LCMO & LBMO films having higher TCR but at lower temperature.

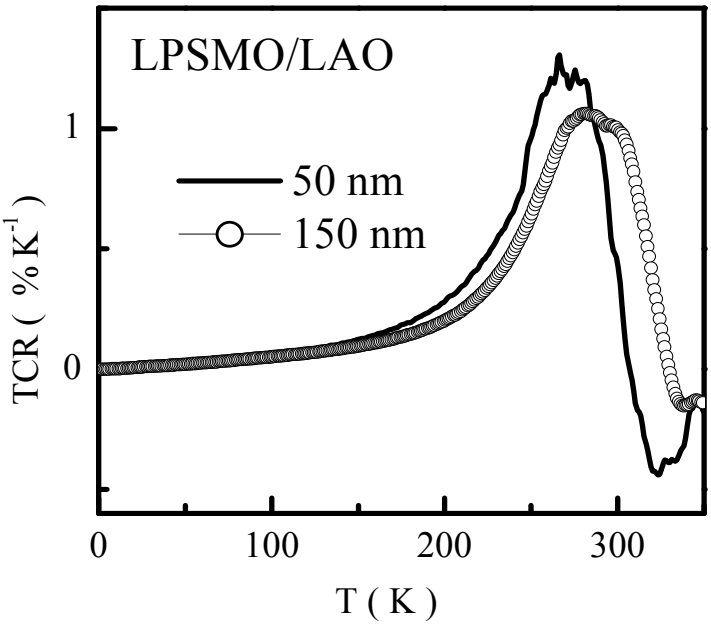

Figure 3.12. (B): Temperature coefficient of resistance of the 50nm and 150nm LPSMO/LAO films.

Table 3.4: TCR values for the 50nm and 150nm LPSMO thin films deposited on the STO and LAO substrates.

Sample	Film Thickness	Maximum Positive TCR	Maximum Negative TCR
LPSMO/STO	50nm	1.51% K^{-1} (273K)	-0.30% K^{-1} (332K)
	150nm	2.14% K^{-1} (300K)	-0.29% K^{-1} (332K)
LPSMO/LAO	50nm	1.20% K^{-1} (274K)	-0.42% K^{-1} (326K)
	150nm	1.04% K^{-1} (285K)	-0.14% K^{-1} (337K)

3.1.3 (a) FCR studies

It is know fact that, on application of manganite field, the resistivity of the manganite decrease due to the alignment of spins of Mn-O-Mn bond. This property of field dependence of resistivity of manganite films can be used for field sensing application.

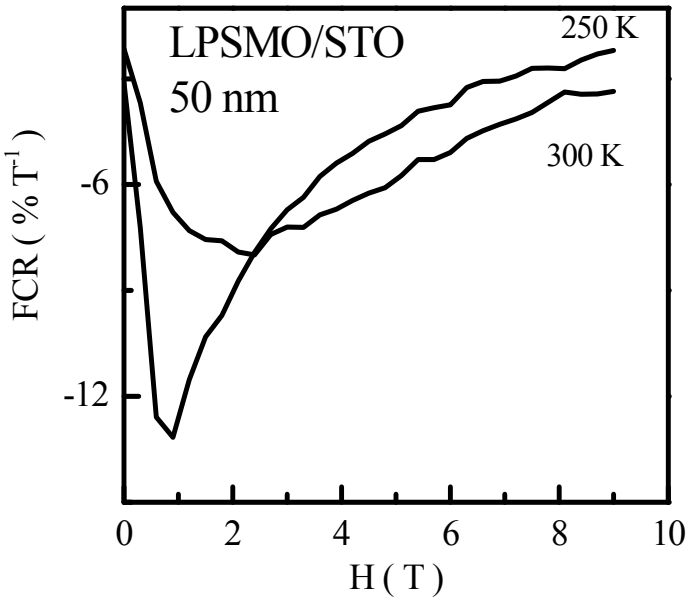

Figure 3.13. (A): FCR vs. H (T) plots of 50nm LPSMO/STO film at 250 & 300K.

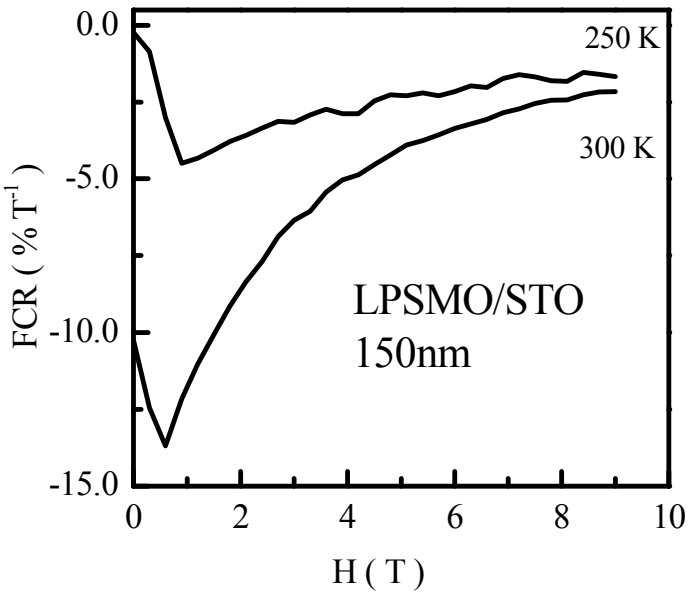

Figure 3.13. (B): FCR vs. H (T) plots of 150nm LPSMO/STO film at 250& 300K.

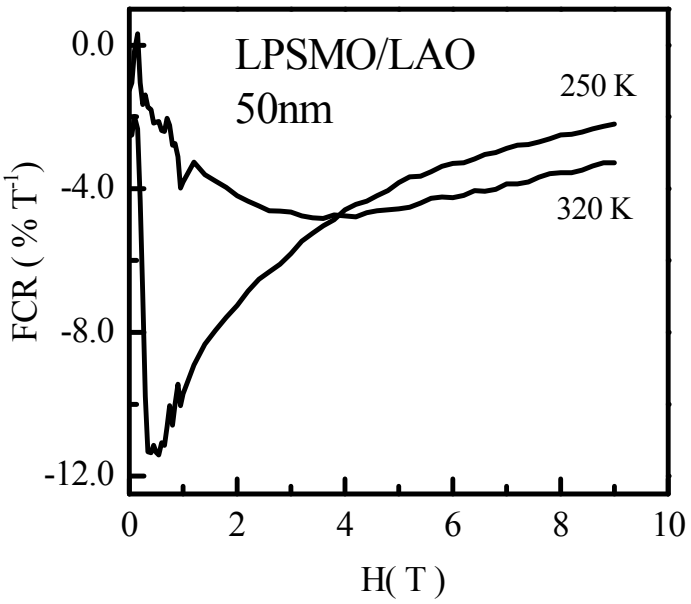

Figure 3.14. (A): FCR vs. H (T) plots of 50nm LPSMO/LAO film 250& 320K.

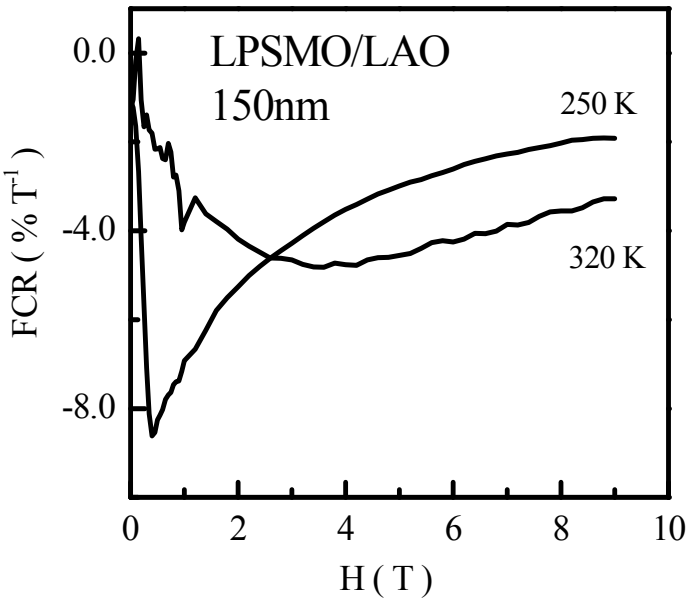

Figure 3.14. (B): FCR vs. H (T) plots of 150nm LPSMO/LAO film 250& 320K.

Table 3.5: Values of FCR for 50nm and 150nm LPSMO films deposited on the STO and LAO substrates.

Sample	Film Thickness	Temperature	Field (Tesla)	Maximum FCR
LPSMO/STO	50nm	250K	0.9	$-13.10\%T^{-1}$
		300K	2.1	$-7.91\%T^{-1}$
	150nm	250K	0.9	$-4.50\%T^{-1}$
		300K	0.6	$-13.56\%T^{-1}$
LPSMO/LAO	50nm	250K	0.5	$-11.33\%T^{-1}$
		320K	3.4	$-4.75\%T^{-1}$
	150nm	250K	0.38	$-8.50\%T^{-1}$
		320K	3.5	$-4.77\%T^{-1}$

The field coefficient of resistance (FCR) can be determined using

$$FCR(\%) = \frac{1}{R}\frac{dR}{dH} \times 100 \bullet T^{-1} \quad \text{.....(4)}$$

Figures 3.13.(A) & (B) and 3.14.(A) & (B) shows the FCR vs H plots at the different temperatures for the 50nm and 150nm LPSMO thin films grown on the STO and LAO substrates, respectively. Table 3.5 lists the maximum FCR values calculated at different fields and temperatures in the vicinity of the T_{IM} for all the LPSMO films. From these figures, it can be seen that, FCR curve has a negative peak at very low field indicating the effect of the magnetic field on the manganite domains in the films which is reflected in the field sensitivity of the sample. With the application of field, spins in the magnetic domains are aligned resulting in a large decrease in the resistance. Value of the FCR depends upon the ferromagnetic response of the film, which is temperature dependent. Further, 150nm LPSMO/STO film shows the high FCR value at the 300K as compared to 50nm strained films. A notable feature observed in LPSMO/LAO films is, at 320K, the FCR decreases with increasing field because above T_C, the LPSMO/LAO behaves as paramagnetic semiconducting insulator. From the Table 3.5 it can be noted that, FCR

values are higher in the LPSMO thin film deposited on the LAO substrate as compared to deposited on the STO substrate which suggests that reflected that LPSMO/LAO thin films are strain released as compared to LPSMO/STO films.

3.1.4 Conclusions

We have synthesized various LPSMO films on STO and LAO substrates using PLD technique and studied their structural, morphological, electronic transport and magnetotransport properties. XRD analysis reveals that, all the films possess single-phase epitaxial nature. The strain induced due to lattice-substrate mismatch in the films decreases with the film thickness in both the sets of films. AFM studies show that, grain size and growth is less prominent in LPSMO/STO films as compared to larger grain size and good grain connectivity in LPSMO/LAO films.

Temperature dependence of resistivity studies on LPSMO films show that, insulator to metal transition occurs in case of all the films in the vicinity of the RT. The nature of ρ -T curves with and without applied field, follows the same path in both the sets of films below 200K, indicating the complete spin polarization without field also. This behavior suggests the half metallic nature of the LPSMO manganite films in the temperature range up to 200 K. This behavior may be attributed to the Pr^{+3} substitution at A-site, which induces A-site size variance in broadband LSMO system and change the Mn-O-Mn bond angle, thereby preventing the overlapping between Mn e_g and O_{2p} orbitals, resulting into the half metallic behavior in temperature range $\sim 5 - 200$ K. From the above findings, it is clear that strain in the films plays an important role in the distortion of Mn-O-Mn bond angle, which results in the spin polarization. This behavior is highly useful in the spin injector and spin valve devices.

The observation of large MR (~50%) in LPSMO thin films near RT is mainly due to large size variance introduced to the Pr^{+3} substitution at La-site. Spin polarization up to 200 K in the 50 nm and 150 nm LPSMO films, results in the negligible MR at low temperature. Observation of LFMR ~ 17% (<1T) in the bulk LPSMO sample as compared the thin films ~ < 1% show the inter grain spin polarization in the bulk sample and absence of grain boundary effect in the thin films. All the LPSMO thin films exhibit maximum TCR value in the vicinity of the RT. The observation of appreciable FCR

value in the small-applied fields in the vicinity of the RT shows the potential of its application in field sensor.

From the above-mentioned conclusions, it can be inferred that, the transport & magnetotransport properties of LPSMO films on STO & LAO substrates have been tailored for the usefulness of these films for sensing applications in the vicinity of RT.

3.2 Studies on SHI irradiated LPSMO thin films

Effect of Swift Heavy Ion (SHI) irradiation on the modifications in the structural, electronictransport and magnetotransport properties of the manganite thin films is an exciting but not yet fully understood area of research [34, 35]. It is an established fact that, SHI irradiation is responsible for the dramatic changes in various properties of manganites because it results in the effects like: change in the surface morphology, magnetic anisotropy, columnar or point defect formation, amorphization of the material, etc. [34-36]. Since irradiation can lead to a controlled introduction of defect states in the material, it may be useful to improve the material properties in desired manner.

In our reported work, it has been shown that, irradiation with an optimal dose is responsible for the strain release in the $La_{0.5}Pr_{0.2}Ba_{0.3}MnO_3$ (LPBMO) manganite thin films [36]. Also, it is reported that, for a particular ion dose, the resistivity is suppressed by a small factor in $La_{0.75}Ca_{0.25}MnO_3$ (LCMO) manganite films, the reason for which was not made clear [37]. In the presently studied LPSMO films, there is a large lattice mismatch between STO substrate and film and the size variance (σ^2) is ~ 0.00249 which is large as compared to σ^2 ~ 0.00186 reported for LSMO film. This results into magnetic inhomogeneity in the dead layer and a large strain at the film-substrate interface. Hence, it is interesting to explore whether irradiation helps in the release of strain at the interface and reduce the disorder in the dead layer. Keeping this in mind, SHI irradiation was carried out on the LPSMO thin films. The comparison of the electronic and magnetotransport properties of pristine and irradiated LPSMO thin film is discussed in detail in this section.

Heavy ions like Ag^{+15} having energy ~ 200 MeV were choosen for irradiation because of the fact that due to their larger mass, they are known to produce columnar defects in the material [34, 35]. While passing through the material, the energetic ions lose energy mainly in two ways, namely through: i) inelastic collision of highly charged energetic ions with the atomic electron of the matter, called electronic energy loss [$(S_e) = dEe/dX$] , and ii) elastic scattering from the nuclei of atom of the matter [nuclear energy loss $(S_n)= dE_n/dX$]. In the present study, we have calculated S_e = 13.61 KeV/nm and S_n= 37.34 eV/nm for LPSMO thin films and projected range of Ag^{+15} ions was found to be about 23.28 μm using SRIM-2003 (The Stopping and Range of Ion in Matter)

calculations [38]. In the present case, projected range of Ag^{+15} ions is very high as compared to maximum film thickness (100 nm), which ensures that Ag ions pass through the film material and finally enters into film substrate. In present work, SHI irradiation was carried out using 200 MeV Ag^{+15} ions at a fluence of about 5×10^{11} ions/cm^2 at 15 - UD Tandem Accelerator at IUAC, New Delhi. The irradiation was performed at a low angle with respect to the ion beam to avoid the channeling effect. The ion beam was focused on to a spot of about 1 mm diameter on the sample and was scanned over a 10 x 10 mm^2 area using a magnetic scanner in order to irradiate the thin film over a sufficiently large area with uniformity.

The LPSMO films were characterized for structural phase and purity by XRD measurement and for the surface morphology using AFM measurements. Electrical resistivity and magnetoresistance measurements were carried out by using standard dc four-probe configuration with and without applied field (PPMS quantum design).

3.2.1 Structure and surface morphology

3.2.1(A) Structure

The Rietveld fitting of the XRD data of LPSMO bulk target showed that the sample crystallizes in orthorhombic Pnma type of structure with cell parameters a = 0.5512(2) nm, b = 0.7791(2) nm, c = 0.5548(2) nm. The XRD patterns of pristine and irradiated LPSMO thin films were indexed using orthorhombic cell parameters of bulk compound. Figs 3.15 (A) and (B) shows, the indexed XRD peaks of 50nm & 100nm pristine and irradiated LPSMO film. From the XRD patterns, it can be seen that, both the films possess epitaxial growth in (*0k0*) direction. It can be seen from the fig.3.15 (A) that, in 50nm pristine film, (*040*) peak located at ~ 47.03° shifts to lower angle ~ 46.69° after irradiation. Also, the XRD peak intensity increases while FWHM ~ 0.2988 for pristine 50nm film reduces to ~ 0.1248 after irradiation. Similar effect is observed in the 100nm film [Fig.3.15 (B)]. This observation shows that irradiation has an effect on the strain present in the film. The lattice mismatch δ along the interface has been calculated using the eqn.(1) [Section 3.1.1] .The positive value of the mismatch corresponds to the tensile strain ~ 1.00 %, and 0.87 % in 50 and 100 nm pristine LPSMO films respectively, suggesting that, strain is released with the increase in the film thickness. After irradiation, tensile strain becomes ~ 0.33 % and 0.24% for the 50 and 100 nm films,

respectively, suggesting that the strain is released appreciably in the films due to irradiation, which is confirmed from the XRD peak becoming sharp and reduction in FWHM value [Figure 3.15.(A) & (B)]. This indicates an improvement in the crystalline structure of the films irradiated with 5 $\times 10^{11}$ ions/cm^2 ion dose.

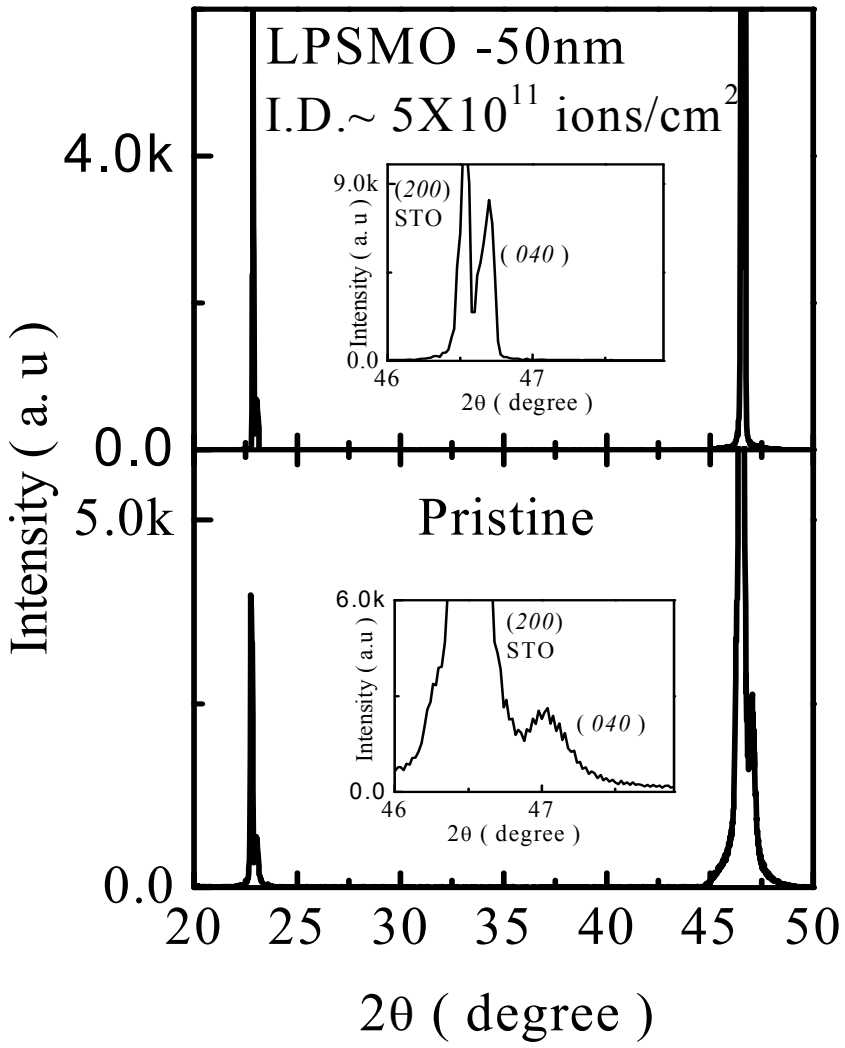

Figure 3.15.(A): A typical XRD pattern of 50nm LPSMO thin films (Pristine and Irradiated). Inset of the shows the enlarged indexed (*040*) XRD peaks of films.

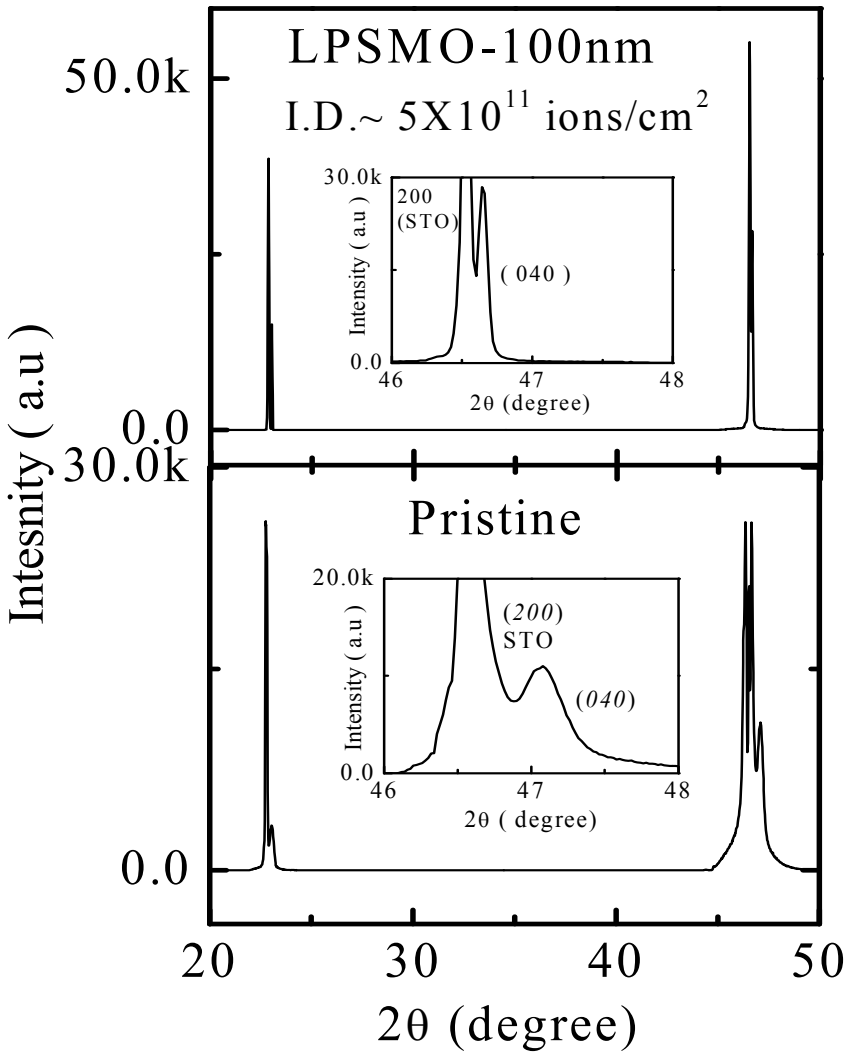

Figure 3.15.(B): A typical XRD pattern of 100nm LPSMO thin films (Pristine and Irradiated). Inset of the shows the enlarged indexed (*040*) XRD peaks of films.

3.2.1(B) Surface morphology

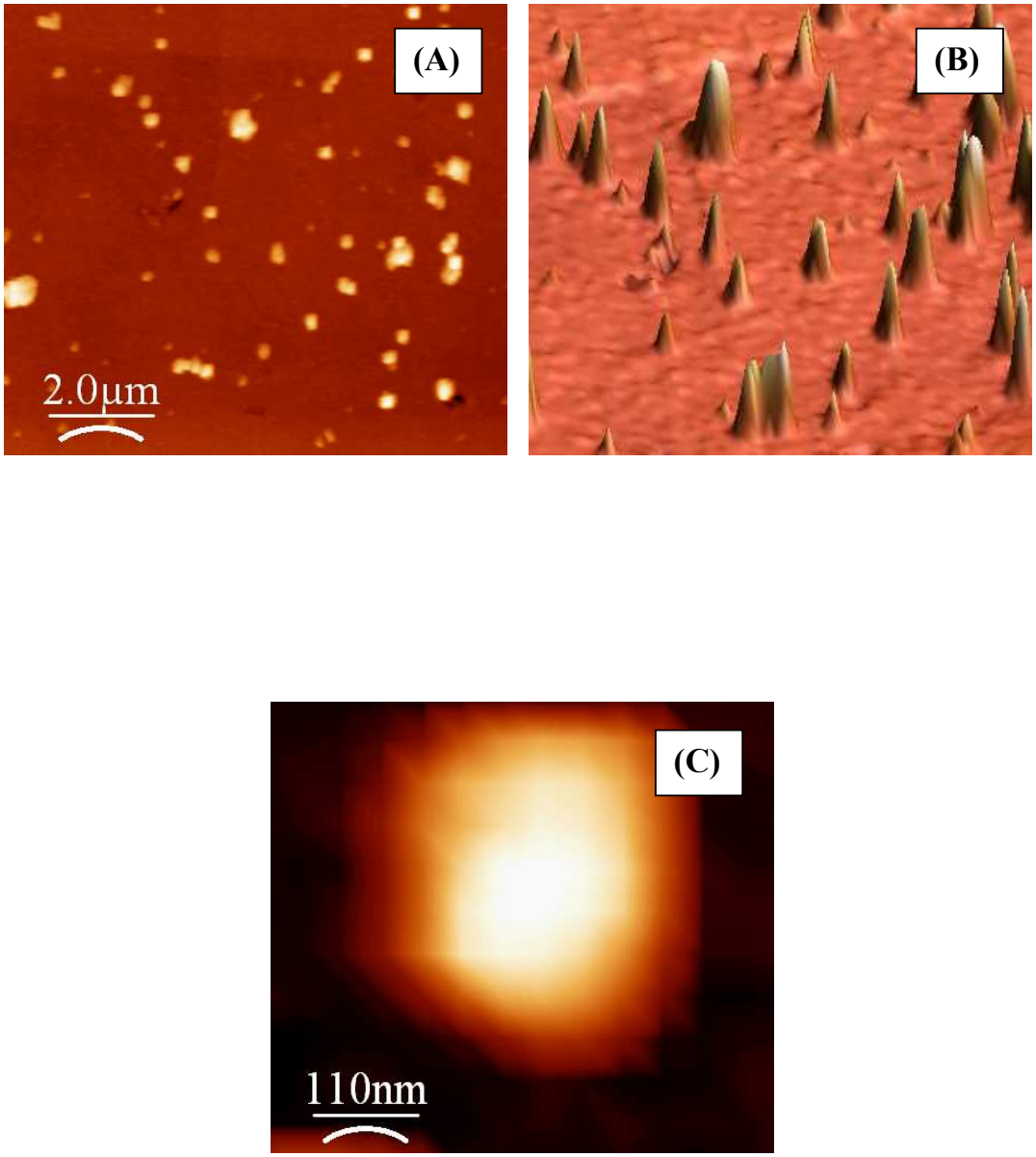

Picture 3.5: AFM pictures of irradiated 50 nm LPSMO thin films. (A) 2D view of irradiated surface (B) 3D image of the irradiated surface (C) Enlarged view of defect.

Picture 3.5 depicts the AFM photographs of irradiated 50 nm LPSMO thin film as a 2D image of the irradiated surface showing modification due to the Ag^{+15} ion bombardment. This surface modification can be clearly seen in the 3D image of the photograph [Picture 3.5 (B)] having the same scan size of the 2D image. The track like defects formed, possess an average diameter of ~ 50 nm [Picture 3.5 (C): enlarged view of defect]. From the calculation of size of the track like defects, it can be concluded that this size is quite large as compared to normal columnar defect size. Also the outgrowths present next to columnar like defects could be arising due to the energetic ions striking the surface-producing spike like structures.

3.2.2 Electrical resistivity and magnetoresistance

3.2.2(A) Electrical resistivity

The temperature dependence of the resistivity curves for the 50 & 100nm LPSMO/STO film have been shown in the figs 3.16, having T_{IM} values ~ 303 K and 324 K respectively. T_{IM} increases with the film thickness indicating the presence of higher strain in the thinner film [11]. In the same figure, effect of SHI irradiation on the resistivity of 50 nm and 100 nm LPSMO films has been shown. It can be seen, that irradiation results in the suppression in the resistivity by ~ 68 % and 31 % for 50 nm and 100 nm films respectively. The T_{IM} values decrease from 303 K to 298 K for 50 nm films and from 324K to 315K for 100 nm film. This observation of decrease in the T_{IM} due to irradiation cannot be attributed to the oxygen deficiency, as the resistivity is also found to decrease after the irradiation. It is well known that, oxygen deficiency increases the resistivity as one of the consequence of irradiation [38, 39]. The decrease in the resistivity and T_{IM} both indicates that, the irradiation creates appreciable changes in the transport properties by changing the lattice distortions and increasing the defect concentration. Also, the calculated projected range of Ag^{+15} ions in the LPSMO films is very large than the maximum film thickness. The nature of the fits to the resistivity plots of pristine & irradiated LPSMO films, below T_{IM} (in the metallic region) shows that, in the irradiated films drop in the resistivity increases considerably as compared to that in pristine LPSMO films (fig. 3.17).

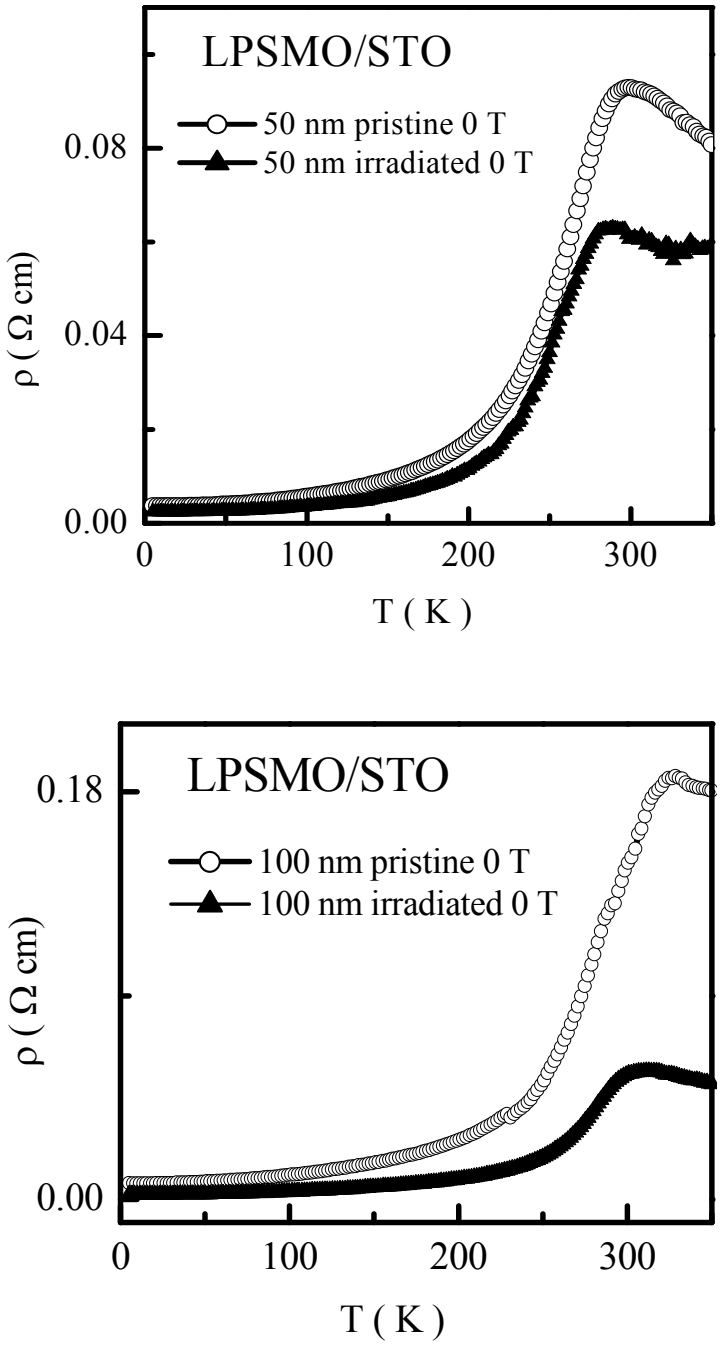

Figure 3.16: Resistivity vs temperature plots of 50nm and 100 nm LPSMO/STO films in zero applied field (Pristine and Irradiated).

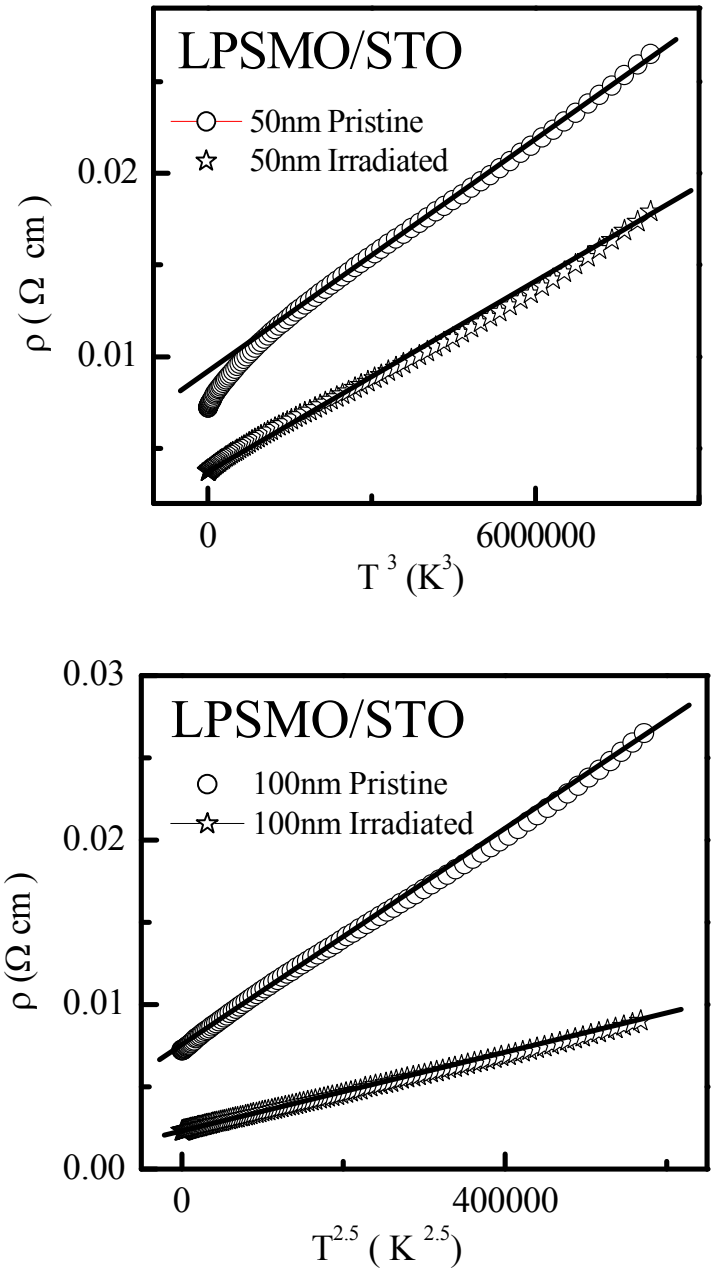

Figure 3.17: Low-temperature resistivity fits to magnon-scattering law in zero applied field for 50 nm and 00nm LPSMO/STO thin films. The symbols are the experimental data points& the solid curves are the theoretical fits.

The resistivity data in the metallic region was fitted in the magnon scattering law $\rho(T) = \rho_0 + BT^n$, in which ρ_0 is residual resistivity and B is electron – magnon scattering coefficient. From the fig. 3.17, it can be seen that, 50 nm and 100 nm films (pristine and irradiated both) obey the one magnon scattering law ($\rho \propto T^3$) and unconventional magnon scattering law ($\rho \propto T^{2.5}$), respectively. Also, the fitting of the ρ-T data to the magnon laws is better for irradiated LPSMO films as compared to their pristine counterparts, in the temperature range 5-200 K, indicating the better crystallanity in the film after irradiation.

3.2.2(B) Magnetoresistance and Field Sensitivity

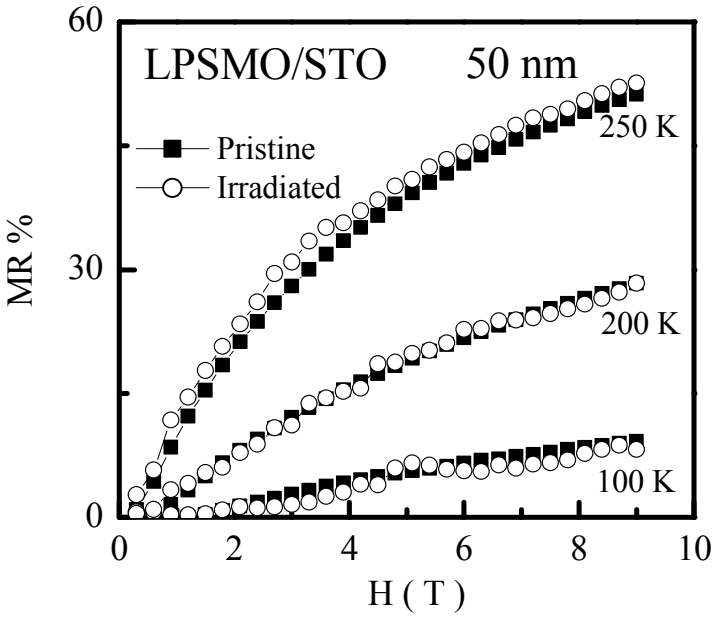

Figure 3.18.(A): MR vs. H (T) isotherms of 50nm LPSMO/STO thin film (Pristine and Irradiated).

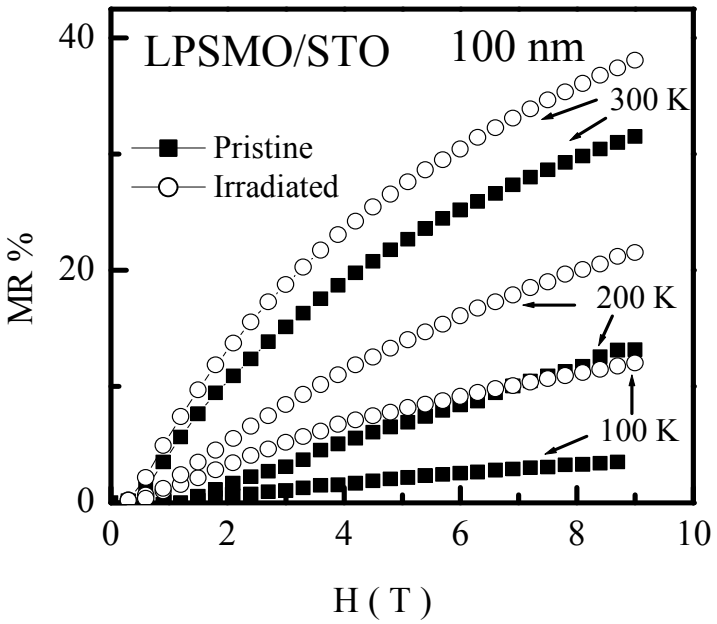

Figure 3.18.(B): MR vs. H (T) isotherms of 100nm LPSMO/STO thin film (Pristine and Irradiated).

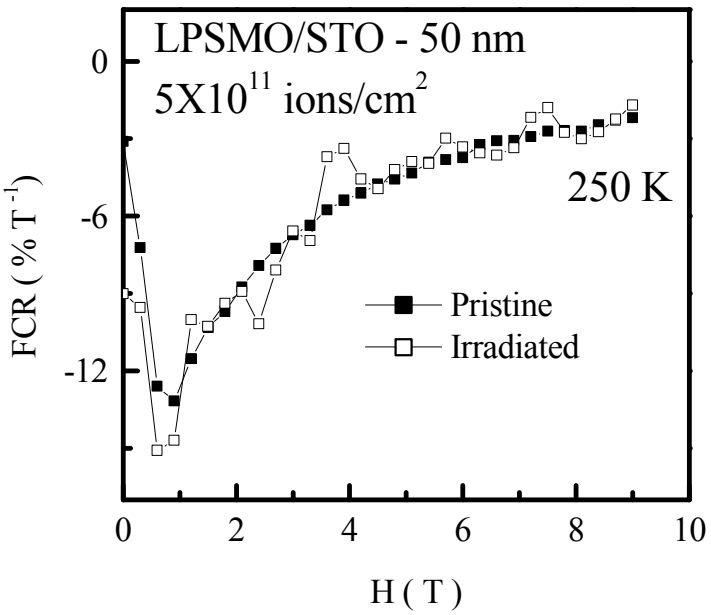

Figure 3.19.(A): FCR vs. H (T) plots of 50nm LPSMO thin film (Pristine and Irradiated).

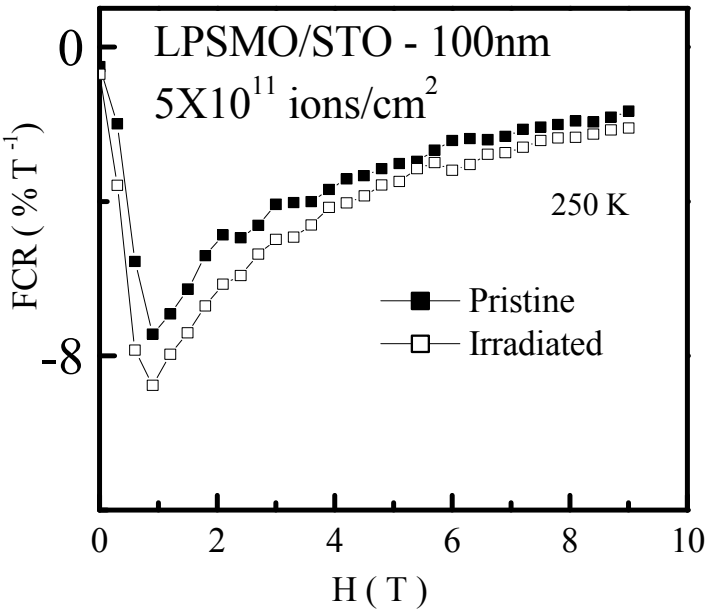

Figure 3.19.(B): FCR vs. H (T) plots of 100nm LPSMO thin film (Pristine and Irradiated).

Figure 3.18.(A) & (B) shows the MR vs H isotherms for the 50&100nm LPSMO/STO films (pristine and irradiated). Figure 3.19. (A) & (B) shows the FCR vs H isotherms of the LPSMO/STO thin films (pristine and irradiated). It can be seen from the figs 3.18 & 3.19 that, in the 50nm film after irradiation there is no change in the MR and FCR values while in the 100nm LPSMO/STO film, there is a marginal increase in the MR and FCR after irradiation with 5×10^{11} ions/cm^2. This may be understood in the terms of thickness dependent irradiation effect, as energy loss of heavy ions is thickness dependent. In the higher thickness films, SHI creates more defects resulting into magnetic anisotropy which is removed on application of field thereby giving higher MR and FCR values.

3.2.3: Comparison between properties of pristine and irradiated thin films

The comparison of physical properties of the pristine and irradiated LPSMO films shows that the suppression in resistivity of the irradiated films is more pronounced as compared to the pristine films which can be described due to

(1) The strain released at the film-substrate interface in the dead layer. Swift heavy ions with lower fluence (5×10^{11} ions/cm^2) are responsible for creating the pressure in the lattice, which reduces the structural distortion in the unit cells around their path effectively in the dead layer resulting in the strain release. In the lower thickness film (50 nm), it can be seen that, the contribution of the dead layer is more in releasing the strain and hence relatively large suppression in resistivity.

(2) Local heating effect caused by the swift heavy ion irradiation of the films, results in as annealing effect, which makes Mn – O – Mn bond angle towards the 180° thereby favoring Zener Double exchange and suppression in resistivity.

3.2.4 Conclusions

We have studied the effect of SHI irradiation on the physical properties of LPSMO/STO films. Structural studies using XRD, shows that, the indexed XRD peaks in the irradiated films swifts towards lower angle and the peak intensity increases while FWHM decreases in 50nm & 100nm LPSMO/STO films suggesting an improvement in the crystallanity of the films.

The strain calculations from the XRD studies show that, tensile strain is reduced on irradiation. AFM pictures show the modification in the surface morphology of the film due to the ion bombardment. Observed size of the defects from AFM of irradiated surface is quite large as compared to the calculated size of columnar defect. This rules out formation of columnar defects in these films due to irradiation with 5×10^{11} ions/cm^2. Also the outgrowths present next to track like defects could be arising due to the energetic ions striking the surface-producing spike like structures.

Irradiated LPSMO/STO films shows the suppression in resistivity as an effect of the irradiation with ion dose of 5×10^{11} ions/cm^2, possibly due to the surface modifications and formation of track like defects, which releases the strain at the interface of the film-substrate effectively in the dead layer. In addition, the passage of the swift heavy ions through the thin film might result into local heating which causes annealing effect and increases the Zener double exchange thereby favoring suppression of resistivity. It is also observed that, irradiation with 200 MeV Ag ions having fluence of 5×10^{11} ions/cm^2, does not have any appreciable effect on the magnetic sensing parameter and MR of LPSMO/STO films.

Thus, in conclusion, it can be said that, SHI irradiation helps to release the strain in the dead layer and results in an improvement in the crystallanity of the film.

REFERENCES

22. A. UrushiY. Moritomo, A. Asamitsu and Y. Tokura,
Phys. Rev. B **56** 12190 (1994).

23. A. P. Ramírez
J. Phys.: Condens. Matter. **9** 8171 (1997).

24. W.Prellier, Ph.Lecneur, C.Matrin and B. Raveau
J. Phys.:Condens. Matter. **13** R915 (2001)

25. F. Damay, A. Maigan, C. Martín and B. Raveau
J. Appl.Phys. **81** 1372 (1997).

26. D. Kumar and R. Singh
Phys. Rev. B **56** 13666 (1997).

27. K. Ghosh, S. B. Ogle, R. Armes, R. L. Greene, T. Venkatesan, K. M. Gapchup, Ravi Bathe and S. I. Patil,
Phys. Rev. B **59** 533 (1999).

28. C. Martín, A. Maignan, M. Herviev, C. Autret, B. Reveau and D. I. Khomskii
Phys. Rev. B **63** 174402 (2001).

29. S. Sunder Manoharan, H. L.Ju and Kanam M. Krishan,
J. Appl. Phys. **83** 7183 (1998).

30. N. H. Hong, Joe Sakai and Syozo Lami,
J. Appl. Phys. **89** 6976 (2001).

31. R. Von Helmolt, J.Wecker, B. Holzapfel and L. Schultz,
Phys. Rev. Lett. **71** 2231(1993).

11. J. Z. Sun, D. W. Abraham, R. A. Rao and C. B. Eom
Appl. Phys. Lett. **74** 3017 (1999).

12. Teruo Kanki, Hidejazu Tanaka and Tomoji Kawai,
Phys. Rev. B **64** 224418 (2001).

13. J. A. Thornton
J. Vac. Sci.Technol. A **4** 3059 (1986).

14. M. Strikovski and H. John. Miller
Appl. Phys. Lett. **73** 1733 (1998).

15. H. Y. Wang, S-W Cheong, Gang Xiao, N. P. Ong and B. Batlogg
Phys. Rev. Lett. **77** 2041 (1996).

16. Lan MacLaren, Zhong Lin wang, H. S. Wang and Qi Li
Appl. Phys. Lett. **80** 1406 (2002).

17. H. L. Ju, J. Gopalakrishnan, J. L. Peng, Q. Li, G. C. Xiang, T. Venkatesan and R. L. Greene
Phys. Rev. B **51** 6143 (1995).

18. N. Furukawa: "Physics of Manganites" edited by T. Kaplan and S. Mahanti (PlenumPublishing, New York, 1999).

19. C.P. Zener
Phys. Rev. **82** 403 (1951).

20. J. Sun , W. Gallgher, P.Duncombe, L. Krushin-Elbaum, R. Altman, A. Gupta, Y. Lu, G. Gong and G. Xiao
Appl. Phys. Lett. **69** 3266 (1996).

21. Nobuo Furukawa
J. Phys. Soc. Jap. **69** 1954 (2000).

22. J. Rodriguez_Carvajel
FULLPROF version 3.0 Laboratorie Leon Brillioun, CEA-CNRS, (1995).

23. A. Barman and G. Koren
Appl. Phys. Lett. **77** 1674 (2000).

24. Y. Suzuki, Y. Wu, J, Yu, U. Rudiger, A. D. Kent, T. K. Nath, C.B.Eom,
J. Appl. Pys. **87** 6746 (2000).

25. M. B. Salamon and M. Jaime
Rev. Mod. Phys. **73** 602 (2001).

26. K. Kubo and N. Ohata
J. Phys. Soc. Jpn. **33** 21 (1972).

27. Xindong Wang and X.-G. Zhang
Phys. Rev. Lett. **82** 4276 (1999).

28. T. Akimoto, Y. Moritomo, A. Nakamura, N. Furukawa,
Phys. Rev. Lett. **85** 3914 (2000).

29. A. Gupta and J. Z. Sun
J. Magn. Magn. Mater. **200** 24 (1999)

30. P. Raychaudhuri, T. K. Nath, A. K. Nigam and R. Pinto,
J. Appl. Phys. **84** 2048 (1998).

31. Sheng Ju. H. Sun and Zhen – Ya Li
Phys. Lett. A **300** 666 (2002)

32. R. A. Wood, B. E. Cole, C. J. Han and R. E. Higashi
Proc. IRIS Detector **1** 139 (1993).

33. M. Rajeswari, C. H. Chen, A. Goyal, C. Kwo, M. C. Robson, R. Ramesh,
T. Venkatesan, and S. Lakeou
Appl. Phys. Lett. **68** 3555 (1996).

34. S. B. Ogale, R. Shreekala, R. Bathe, S. K. Date, S. I. Patil, B. Hannoyer, F. Petit and G. Marest
Phys. Rev. B **57** 7841 (1998).

35. Ravi Kumar, R. J. Choudhary, S. I. Patil, Shahid Hussain, J. P. Srivastava and S. K. Malik
Appl. Phys. Lett. **86** 222501 (2005).

36. J. H. Markna, R. N. Parmar, D. G. Kuberkar, Ravi Kumar, D. S. Rana and S. K. Malik, Appl. Phys. Lett. **88** 152503 (2006).

37. Ravi Bathe, S. K.Date, S. R.Shinde, L. V. Saraf, S. B. Ogale, S. I. Patil, Ravi Kumar, S. K. Arora and G. K. Mehta
J. Appl. Phys. 83 (1998) 7174.

38. Program SRIM (2003)
J. F. Ziegler and J. P. Biersack, http://www.srim.org.

Chapter - 4

4.1 LPBMO/LAO thin films: Effect of different Ag-ion fluences

The $LaMnO_3$ manganite possesses ABO_3 type perovskite structure and is an antiferromagnetic insulator (AFI) below 170 K. On substituting divalent cations at trivalent La^{3+}, the resulting compositions $La_{1-x}A_xMnO_3$ (where, A is divalent cation) display interesting correlated transport, magnetic and magnetoresistive properties. The physical properties of these compounds are determined by three main factors; i) the divalent doping (substitution) at the La-site (which determines the ratio of Mn^{3+}/Mn^{4+}) ii) the average A-site cation radius and iii) size-disorder at the A-site [1-3]. Depending upon these factors, the exchange interaction between the Mn^{3+} and Mn^{4+} ions via oxygen, largely known as Zener Double Exchange (ZDE), comes into play and drives the material to exhibit insulator to metal transition (T_P) and paramagnetic to ferromagnetic transition (T_C). In the vicinity of T_P, the resistivity drops by a large magnitude on the application of an external magnetic field, thus making the material to display a large negative magnetoresistance (MR).

The application potential of manganites has prompted their synthesis in thin film forms. The study of epitaxial films enhances our understanding of various physical properties of these materials in the absence of dominating grain boundary effects. It is well established that, various properties of manganites such as Tp, T_C, resistivity and magnetoresistance (MR) are sensitive to disorder and crystallographic defects. Irradiation by Swift Heavy Ions (SHIs) is an important tool, which is known to produce structural disorder and localized strains in the lattice [4, 5], which in turn modifies the physical properties of material. However, it largely remains to be understood how irradiation effects change with varying thickness of the films. In order to study this, we have irradiated 50nm and 200nm $(La_{0.5}Pr_{0.2})Ba_{0.3}MnO_3$ (LPBMO) thin films by 200 MeV Ag^{+15} ions with different ion doses in the range of 5×10^{10} to 1×10^{12} ions/cm^2 and carried out resistivity and MR measurements on the films before and after irradiation. Heavy ions like Ag^{+15} having energy ~ 200 MeV were chosen for irradiation because of the fact that, due to their larger mass, they are known to produce columnar defects in the material. In the present studies, we have calculated the value of electronic energy loss (S_e) = 21 KeV/nm and nuclear energy loss (S_n) = 60.3 eV/nm for LPBMO thin films using SRIM-2003 (The Stopping and Range of Ion in Matter) calculations [6]. In this

chapter, it has been shown that, in 50 nm film, the irradiation (up to a dose of ~1×10^{12} ions/cm^2) has very little effect on the transport properties while it is appreciable in 200 nm thin film. Also, the effect of SHI irradiation on the low temperature resistivity minima exhibited by LPBMO films has been studied and the results are discussed.

Synthesis

Polycrystalline bulk target sample of $La_{0.5}Pr_{0.2}Ba_{0.3}MnO_3$ (LPBMO) was synthesized by using standard ceramic method. Dried powders of La_2O_3, Pr_6O_{11}, $BaCO_3$, and MnO_2 (all >99.9% purity) were mixed in stoichiometric proportions and calcined at 950°C for 24 hours. The samples were then ground, palletized and sintered in a temperature range of 1100°C - 1400°C with several intermediate grindings. The details of the bulk sample preparation are given in ref. [7]. Thin films (50nm and 200nm) of the target material were deposited on a single crystalline (*h00*) oriented $LaAlO_3$ (LAO) substrate by Pulsed Laser Deposition (PLD) technique using KrF excimer Laser. The details of the deposition parameters used have been summarized in the Table - 4.1.

Table 4.1: Thin films deposition parameters.

Laser used	KrF excimer
Laser Energy	3.1 J/cm^2
Laser frequency and Pulse width	248 Hz and 25 ns
Substrate to target distance	4.2 cm
Substrate heater temperature	830°C
Oxygen partial pressure	400 mTorr
Target used	$La_{0.5}Pr_{0.2}Ba_{0.3}MnO_3$ (Diameter – 15mm, thickness – 2mm)
Substrate used	Single crystal $LaAlO_3$ (*h00*)

The LPBMO thin films were irradiated by 200 MeV Ag^{+15} ions with irradiation doses of the 5×10^{10} to 1×10^{12} ions/cm^2 using a 15 - UD Tandem Accelerator, at Inter University Accelerator Center (IUAC) New Delhi. The irradiation was performed at an angle slightly away from the beam to avoid the channeling effect. The ion beam was focused on to a spot of 1 mm diameter. To irradiate the thin film uniformly, ion beam

was scanned over a 10×10 mm^2 area using a magnetic scanner. The structure of the samples was analyzed using X-ray diffraction (XRD) and surface morphology was studied using Atomic Forced Microscopy (AFM). The resistivity was measured as a function of temperature in range ~ 5-320K and as a function of magnetic field recorded as 0T - 9T - (-9T) - 0T using PPMS facility at TIFR, Mumbai.

4.1.1 Structure and surface morphology

4.1.1(A) Structure

Structural refinement was carried out by rietveld fitting of the XRD patterns using standard FULLPROF program [8]. Fig. 4.1 shows a typical rietveld refined XRD pattern of LPBMO sample showing a good agreement between the fitted and experimental patterns.

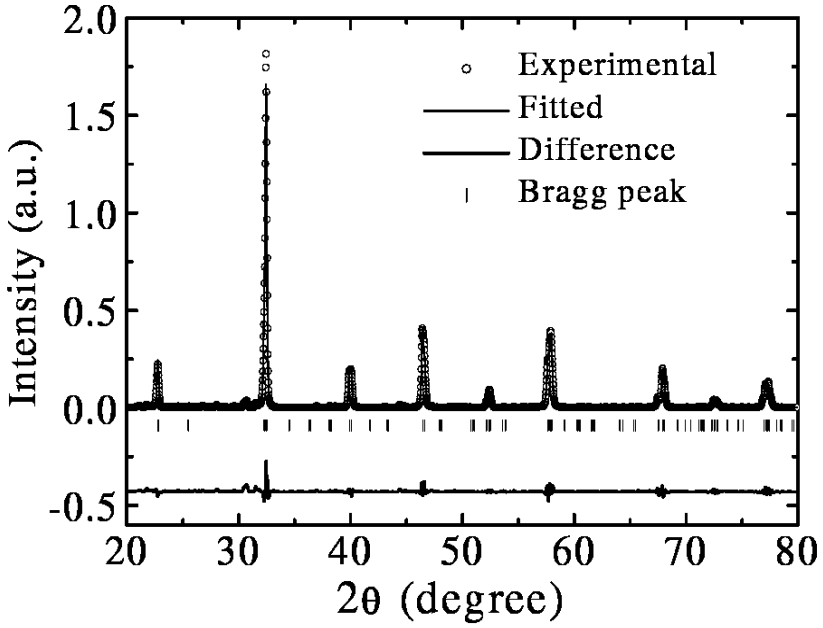

Figure 4.1: Rietveld fitted XRD pattern for LPBMO bulk sample.

The analysis of the XRD data of polycrystalline bulk LPBMO (target) reveals that, sample crystallizes in a distorted orthorhombic structure (space group: *Pnma*, no. 62) with the refined cell parameters, a = 5.512(3) Å, b = 7.791(2) Å and c = 5.548(2) Å,.

4.1.1:(A-1) Strain calculation in the thin film

In the thin films, due to the lattice mismatch between the film and substrate, strain is developed namely tensile strain and compressive strain. The lattice mismatch, δ, along the interface was calculated using eqn.(1) given in chapter III, section 3.1.1. Positive values of the mismatch correspond to the tensile strain [the cell is elongated in the plane of film and compressed along the out of plane growth direction {picture 4.1-(a)}], whereas negative values describe compressive stress [the cell is elongated along the growth direction and compressed in the direction of film plane {picture 4.1-(b)}]. The substrate mismatch strain induces a lattice deformation, which can be analyzed from the unit cell distortion. This distortion is generally calculated using the XRD data [9, 10].

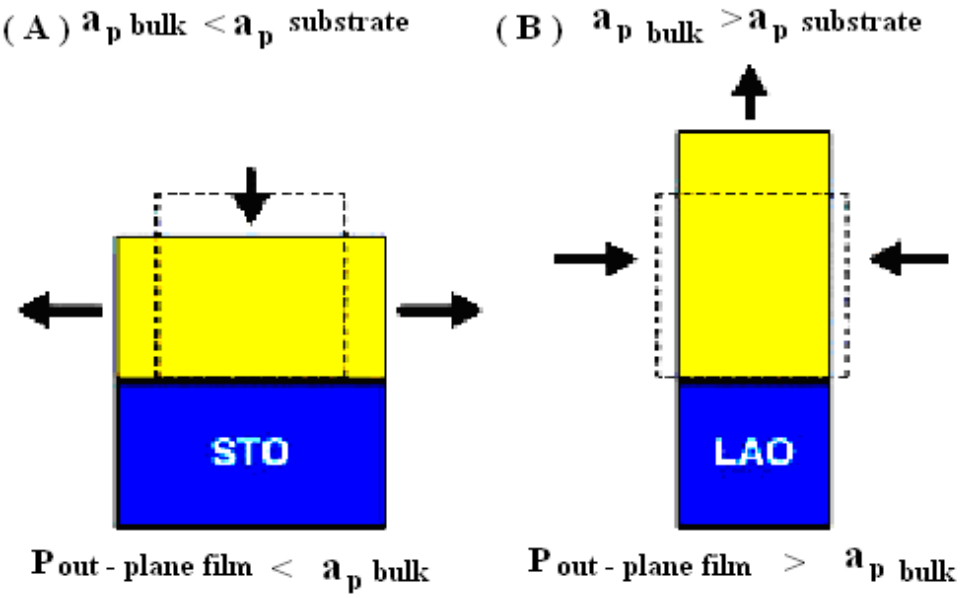

Picture 4.1: Schematic drawings of the lattice distortion in strained epitaxial films (a) under tension or (b) compression.

Figure 4.2 depicts the XRD patterns of pristine and irradiated 50 and 200nm LPBMO film showing the epitaxial single-phase nature of films. The cell parameters of the bulk were used to index the thin film XRD patterns which are oriented in (*101*) direction. From the XRD analysis it can be clearly seen that, in the both the films, there is no phase or structural change observed as an effect of the irradiation with the higher dose of 1×10^{12} ions/cm^2. Also, it may be noted that, with increasing irradiation dose,

an appreciable decrease in the XRD line intensities of the 200nm film is observed which points towards a change in the internal morphology and deteriorating crystalline structure.

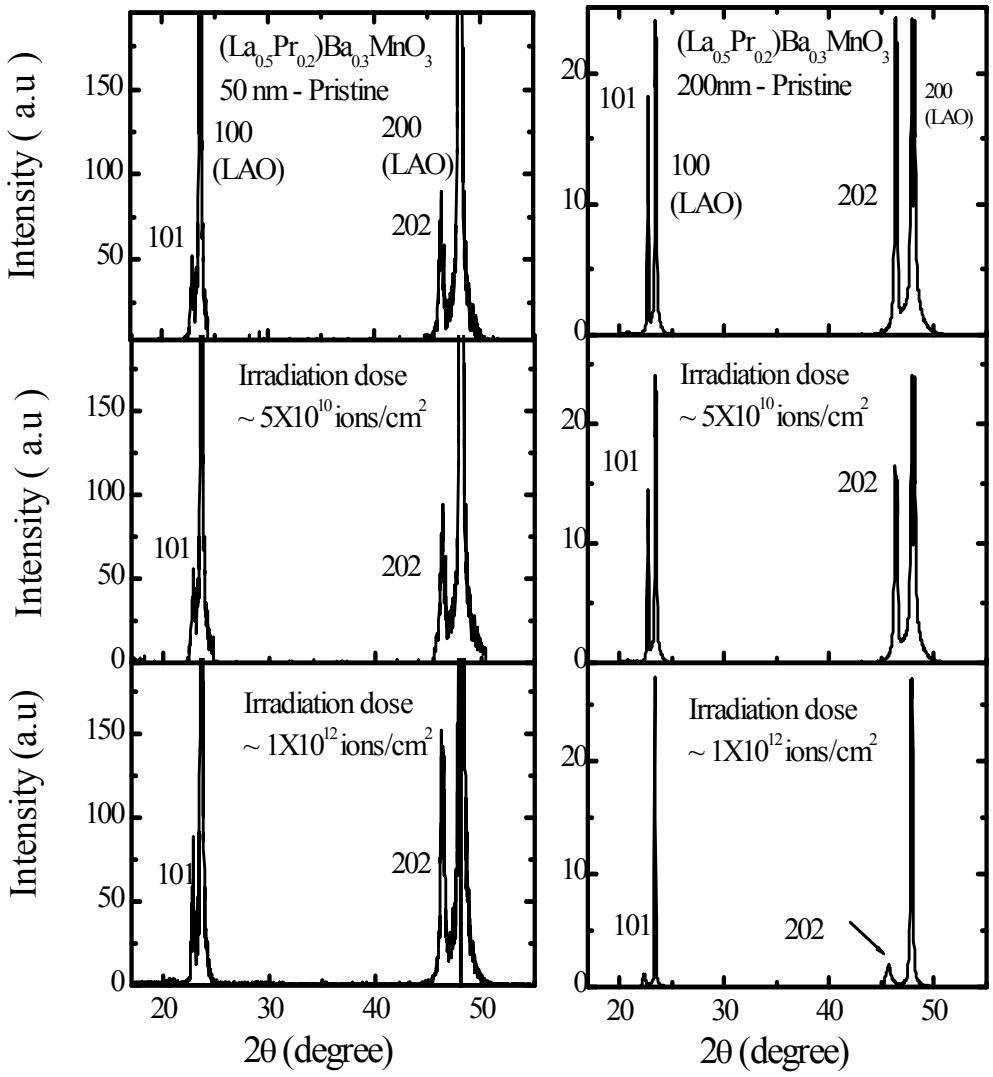

Figure 4.2: XRD patterns (plotted in log scale) for the 50 and 200 nm pristine and irradiated LPBMO thin films.

Table 4.2 lists the calculated values of the film lattice-substrate mismatch for the pristine and irradiated thin films. The pristine 50nm film has higher strain as compared to pristine 200nm film which indicates that as thickness is increase strain is released in the film. In the 200nm LPBMO film, the mismatch ~ -3.29 % observed in pristine film

increases to ~ - 4.57 % in 1×10^{12} ions/cm^2 irradiated film while it increases from ~ - 3.45 % to ~ -3.9 % in 50nm thin film. These values suggest that, on irradiation, the compressive strain increases more effectively in the 200nm film as compared to 50nm film. But this is not true in the case of both the thickness films irradiated with the ion fluence of the 5×10^{11} ions/cm^2, in which, mismatch is released as compared to the pristine film which is anomalous behaviour of strain release as an effect of the irradiation.

Table 4.2: Mismatch calculation of the pristine and irradiated thin films.

Sample	**Irradiation dose**	**Thickness**	**A. Mismatch**
LPBMO	Pristine	50nm	~ -3.45%
	5×10^{10} ions/cm^2		~ -3.50%
	5×10^{11} ions/cm^2		~ - 3.31%
	1×10^{12} ions/cm^2		~ -3.90%
LPBMO	Pristine	200nm	~ -3.29%
	5×10^{10} ions/cm^2		~ -3.30%
	5×10^{11} ions/cm^2		~ -3.20%
	1×10^{12} ions/cm^2		~ -4.57%

4.1.1: (B) Structure and surface morphology

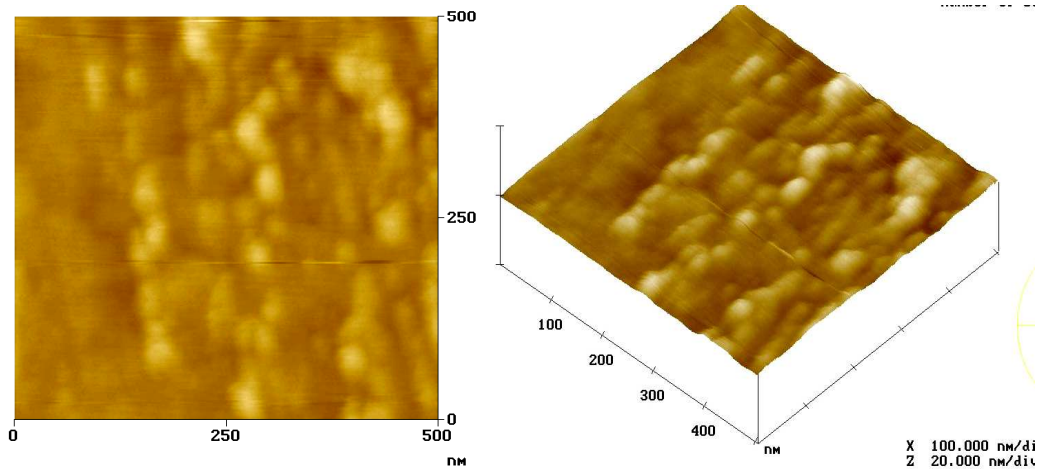

Picture 4.2: Transverse and cross-sectional AFM micrographs of 50 nm LPBMO thin film.

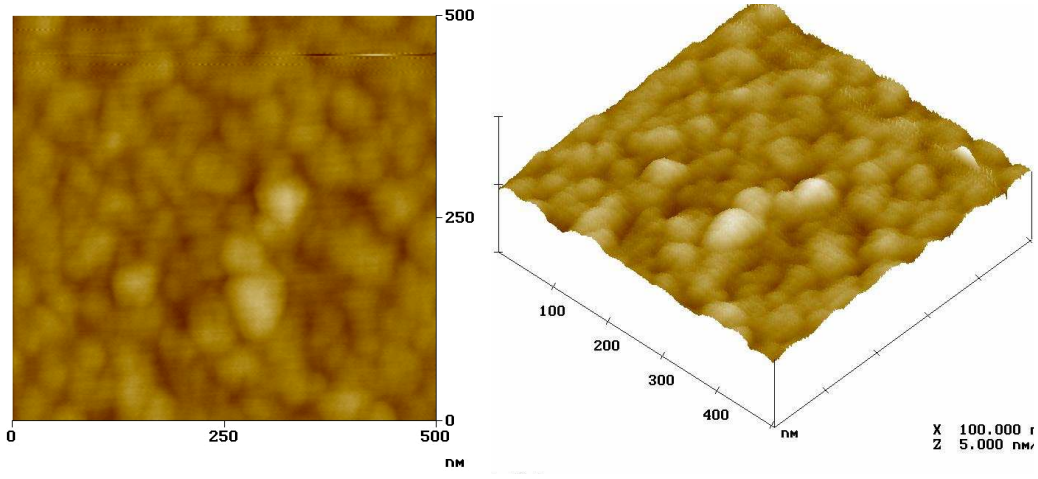

Picture 4.3: Transverse and cross-sectional AFM micrographs of 200 nm LPBMO thin film.

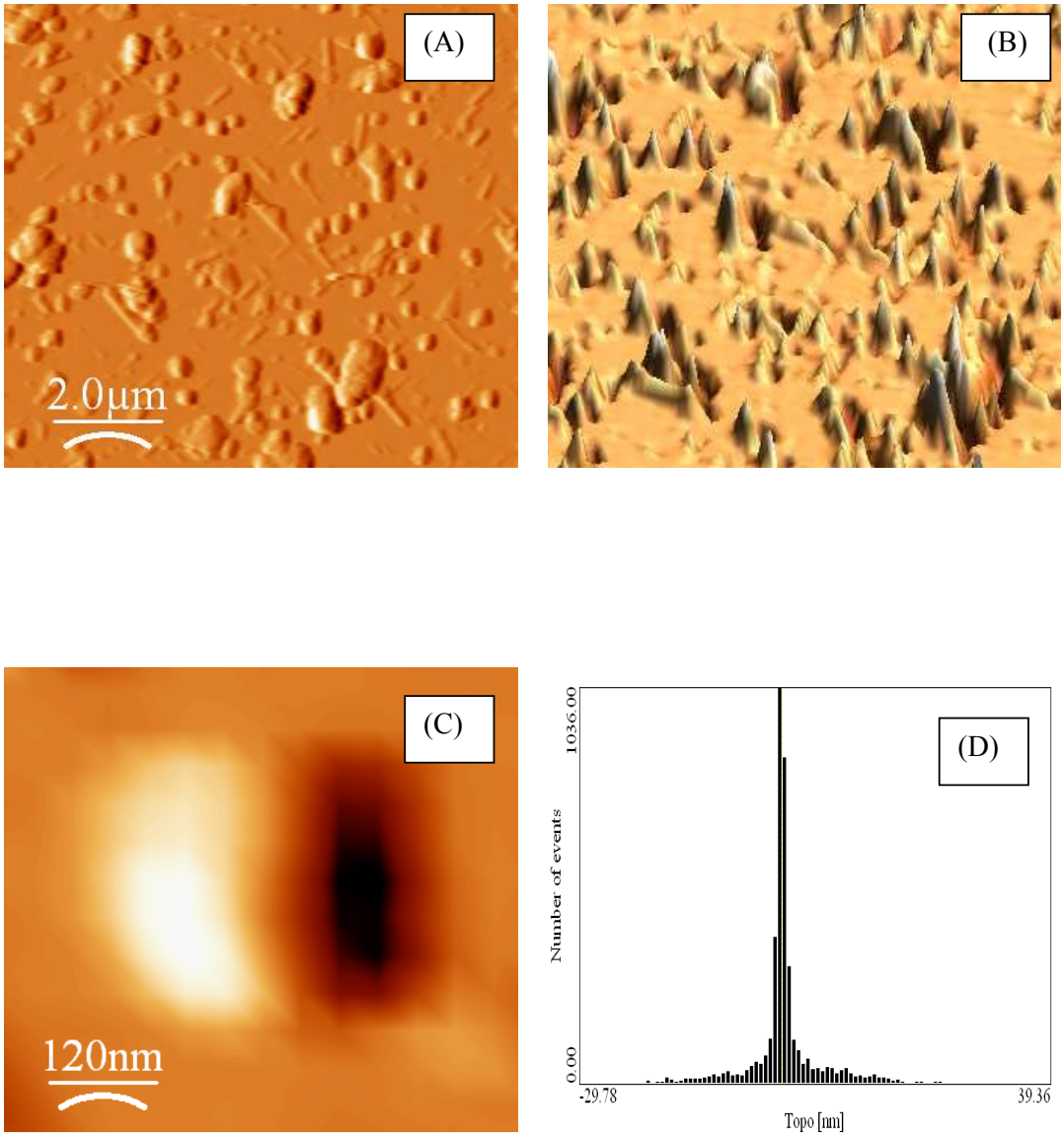

Picture 4.4: AFM pictures of the 50nm LPBMO thin films irradiated with the dose of 1×10^{12} ions/cm^2. (A) 2D AFM micrograph (B) 3D AFM micrograph (C) Enlarged 2D top view of single columnar like defect (D) RMS roughness histogram

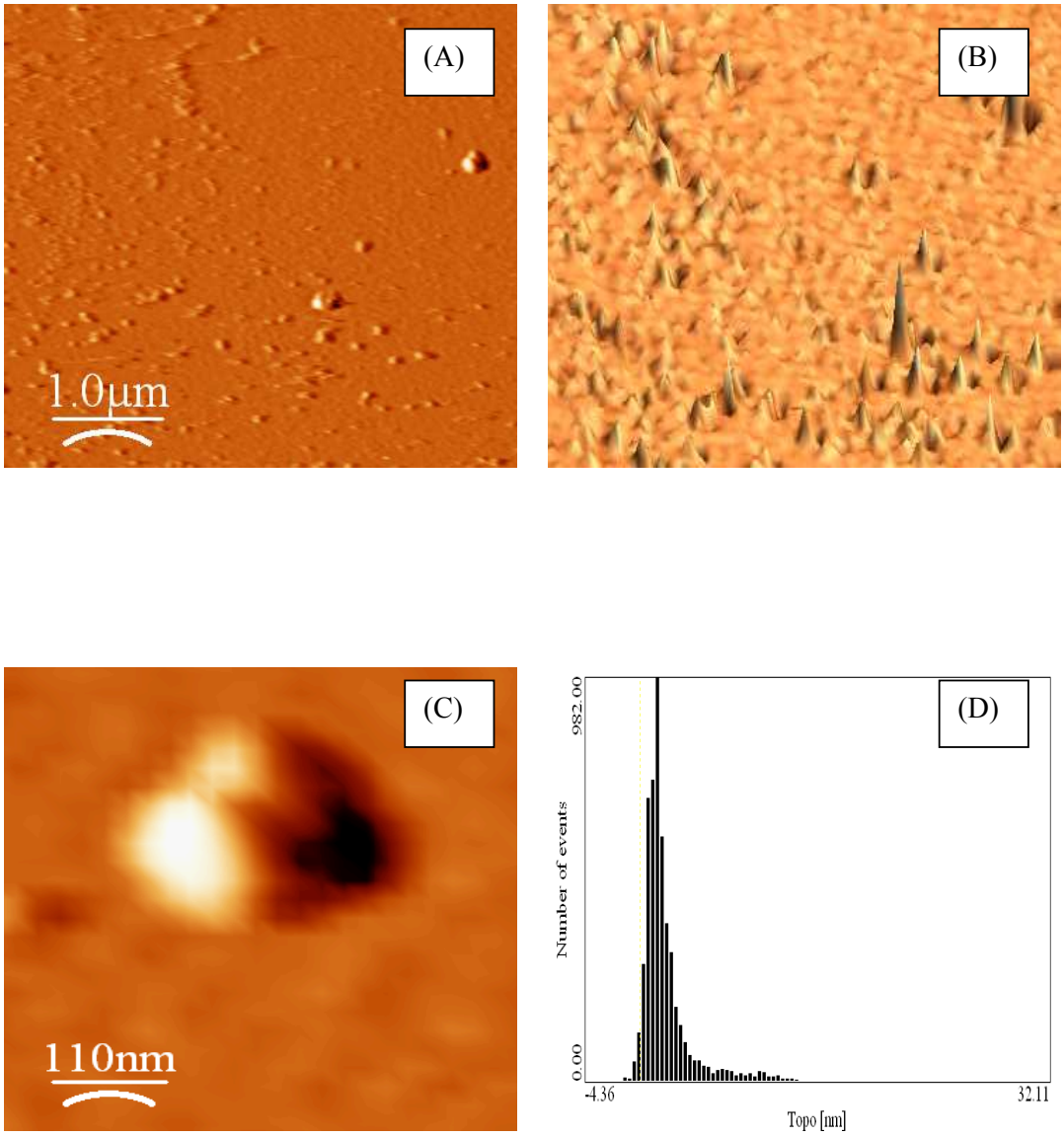

Picture 4.5: AFM pictures of the 200nm LPBMO thin films irradiated with the dose of 1×10^{12} ions/cm^2. (A) 2D AFM micrograph (B) 3D AFM micrograph (C) Enlarged 2D top view of single columnar like defect (D) RMS roughness histogram

The pictures 4.2 & 4.3 show the transverse and cross-sectional views of AFM micrographs of 50nm and 200nm pristine LPBMO films respectively. It can be seen that, the films have smooth surface with a bare roughness of ~ 1 nm. Also the average grain size varies marginally in the range of 50 - 70nm.

However, the surface morphology of irradiated LPBMO films, as studied by AFM micrographs depicts moderate granular surface after irradiation with the higher dose of 1×10^{12} ions/cm^2. Pictures 4.4 & 4.5 shows the AFM micrographs of 50nm and 200nm LPBMO films irradiated with dose of 1×10^{12} ions/cm^2. The RMS roughness is ~ 6.01nm & 3.06 nm for the 50nm and 200nm irradiated thin film, which is higher than the pristine films. It is evident from these pictures that, the Ag^{+15} ion irradiation causes the formation of columnar like defects which can be clearly observed from the 3D image of the photograph having an average diameter of ~ 50 nm (enlarged view of the columnar defect). Thus, the irradiation results in the modification in the surface morphology of both the films.

4.1.2: Electrical resistivity and magnetoresistance

4.1.2(A): Electrical resistivity

Figure 4.3 shows the resistivity vs. temperature plots for the 50nm LPBMO/LAO pristine and films irradiated with different Ag ion doses of 5×10^{10}, 5×10^{11} and 1×10^{12} ions/cm^2, in the temperature range 5-320 K under 0, 5& 9T fields.

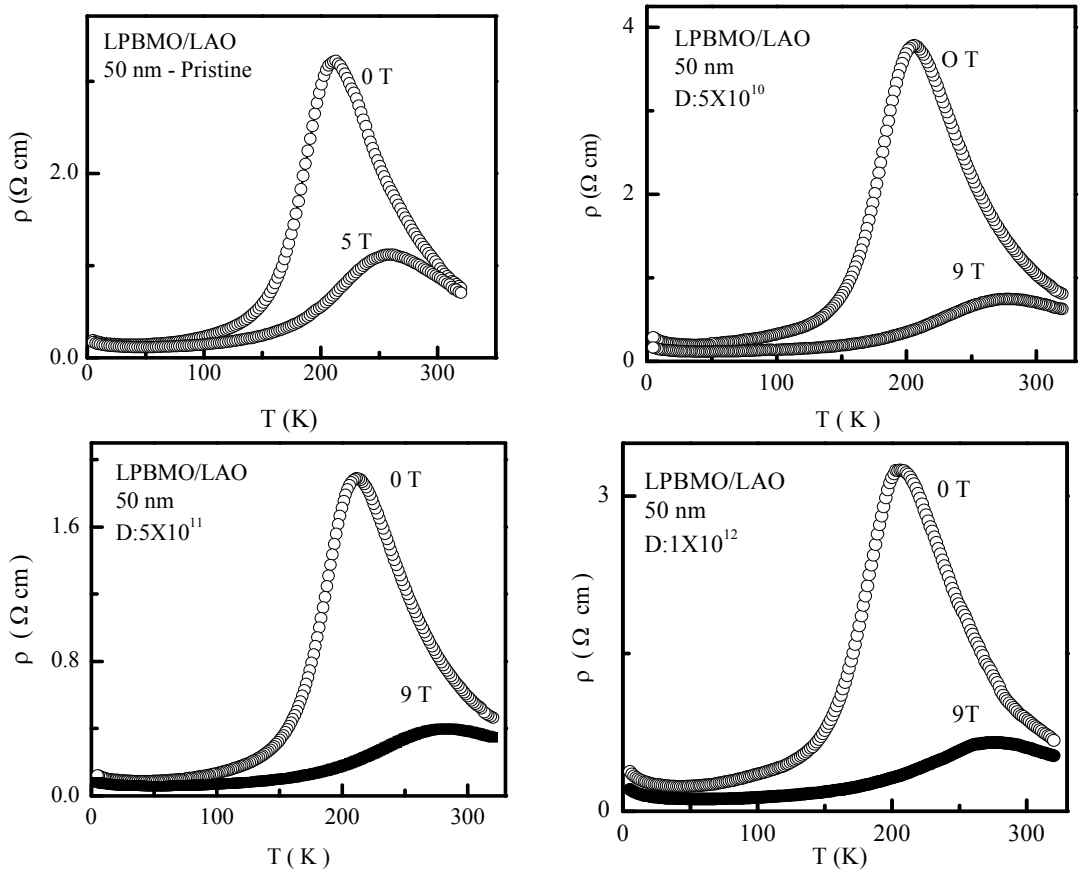

Figure 4.3: Resistivity vs. temperature plots of pristine and irradiated 50nm LPBMO manganite thin film with different ion doses.

It can be seen from the figures that, there is no appreciable change in the T_{IM} of the 50 nm LPBMO films irradiated with different ion doses and the ρ - T does not follow any trend with increasing irradiation dose. The film irradiated with 5×10^{11}ions/cm^2 ions dose exhibits lower resistivity as compared to other films.

Figure 4.4 shows the temperature dependent resistivity behavior of 200nm LPBMO/LAO pristine and Ag-ion irradiated films with 5×10^{10}, 5×10^{11} and 1×10^{12} ions/cm^2 ion fluences, in the temperature range 5-320 K under 0 & 9T fields. It can be seen that, 200nm irradiated LPBMO films do not exhibit any systematic in the version of resistivity with ion doses.

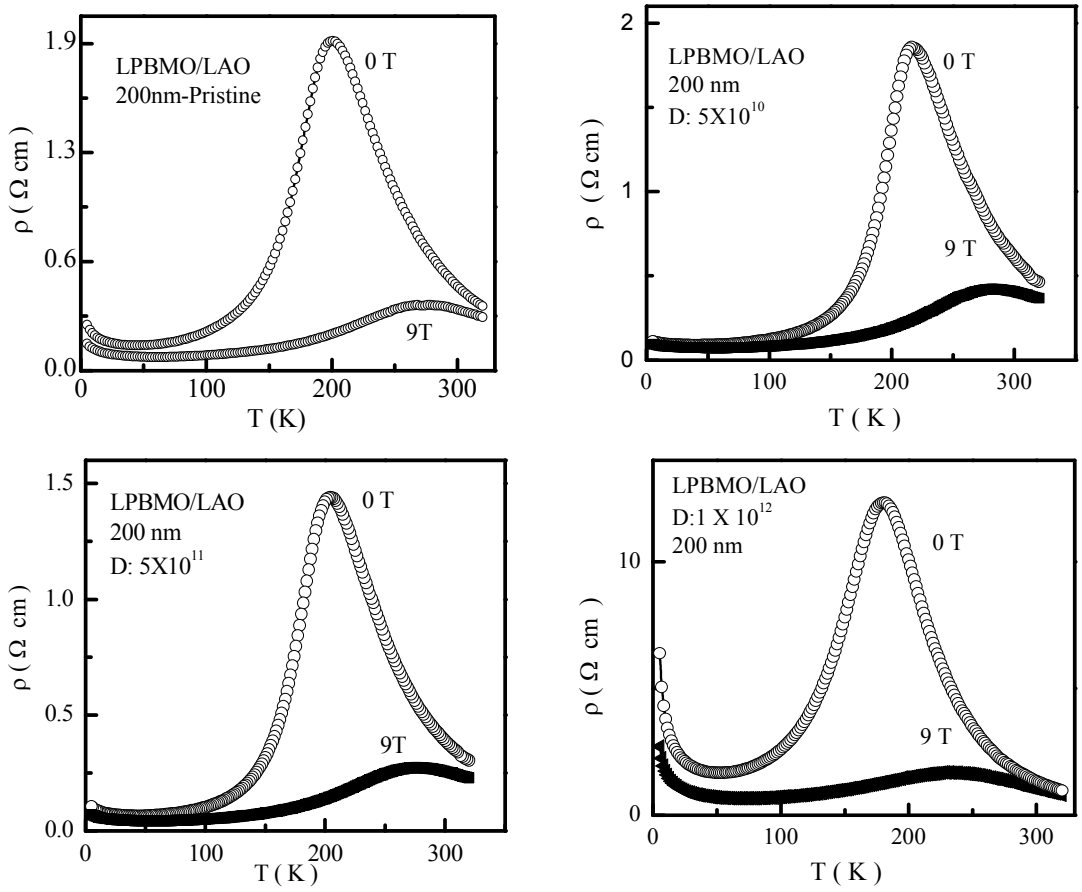

Figure 4.4: Resistivity vs. temperature plots of pristine and irradiated 200 nm LPBMO films with different ion doses.

Thickness dependent irradiation effects with the different irradiation doses and thickness and its comparison with the pristine thin film is shown in the fig. 4.5. It can be seen from the figure that, ρ-T plots of pristine and irradiated 50nm and 200nm LPBMO thin films measured in zero applied field. Before irradiation, 50nm and 200nm films exhibit insulator-metal transition at ~210 K and 200 K, respectively. The resistivity of pristine 50nm film is found to be higher than that of the 200nm film, which may be due to more strain at the interface of the substrate and the film. An interesting noteworthy

feature in resistivity of irradiated 50nm film is that, in the whole temperature range investigated, neither there is any discernible change in resistivity nor any particular trend of the variation of resistivity with increasing irradiation dose (up to ~1×10^{12} ions/cm^2).

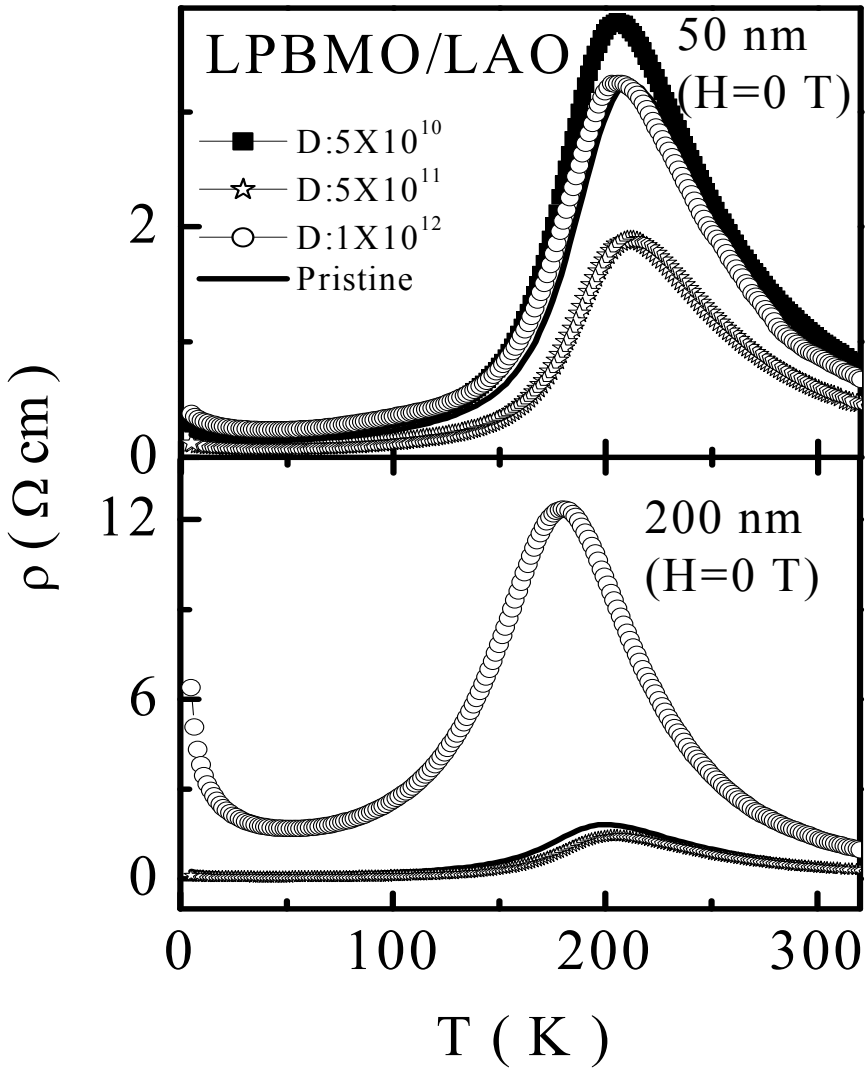

Figure 4.5: Resistivity vs. temperature plots of the 50 nm and 200 nm LPBMO manganite thin film (pristine and irradiated).

However, this is not the case for irradiated 200nm thin film, in which, irradiation dose of the ~1×10^{12} ions/cm^2, causes significant enhancement in the overall resistivity. For instance, the resistivity of this 200nm irradiated film (1×10^{12} ions/cm^2) is larger by ~10 factors at T_P and ~ 25 factors at 5K as compared to that of pristine thin film. Further,

the T_P of 200 nm thin film shifts from ~ 200K for pristine to ~179K for the film irradiated with 1×10^{12} ions/cm^2 dose.

4.1.2(A-1) Irradiation effect on resistivity minimum

In this section studies on the effect of SHI irradiation on the low temperature resistivity minimum (T_{min}) of the 50nm and 200nm LPBMO manganite thin films has been discussed in detail. Upturn in ρ(T) vs. T curves known as the low temperature minimum was observed by the Singh et al. in the $Pr_{0.67}Ca_{0.33}MnO_3$ thin films at ~ 15K in the field of the 4 T [11]. Also Pterov et al. have observed the same phenomenon in granular $La_{0.7}Ca_{0.3}MnO_3$ at around 25K in the zero applied field [12]. But no quantitative analysis of the temperature dependence around the low-temperature minimum was done. The observation of resistance minima at 30 K in $La_{0.7}A_{0.3}MnO_3$ (A=Ca, Sr, Ba) bulk CMR oxides has been explained in term of electron-electron (e-e) interaction and inelastic scattering of electrons [13]. The manganites possess resistivity of ~10-40 mΩcm which is higher than the Mott`s maximum metallic resistivity (~10 mΩcm), justifying the interpretation for the occurrence of resistivity minima in terms of the e-e interaction. However, this study was restricted to zero-magnetic field observation. Observed anomalies in low temperature minima behaviour in LPBMO (bulk and thin film) sample have been investigated in detail by our group in which the role of grain boundary as well as of the magnetic impurity (kondo scattering by a magnetic impurity in a non-magnetic lattice) responsible for the low temperature minima has been ruled out [14]. It has been reported that the low temperature resistivity minima in Ba-based manganites is an intrinsic property which is caused due to the e-e scattering, as a result of columbic interactions. The origin of such a behavior lies in the large size disorder at the A-site, which causes the local structural distortions and is major source of disorder in this low temperature metallic regime.

It is known that the resistivity in the metallic region is due to the various electron-phonon and electron-magnon inelastic scattering processes. The appearance of a semiconducting behavior in the low temperature range (below ~ 50 K) is an anomaly and reproduced by adding e-e elastic scattering term to inelastic scattering term as

$$\rho = \rho_{elastic} + \rho_{inelastic} \quad \textbf{.....(1)}$$

where $\rho_{elastic}$ is the correction to resistivity due to low temperature elastic e-e scattering and $\rho_{inelastic}$ is resistivity term. $\rho_{inelastic}$ increases as temperature increases whereas $\rho_{elastic}$ is dominant at low temperatures. The low temperature correction to the resistivity is given by $\rho_{elastic}$ which is quantified as

$$\rho_{elastic} = \frac{1}{\sigma_0 + BT^{1/2}} \quad \textbf{……..(2)}$$

where σ_0 is the residual conductivity contributed by the temperature-independent scattering processes and B is proportional to the diffusion constant that depicts the depth of the resistivity minimum. However, inelastic scattering, which increases monotonically with temperature, compete with the e-e interaction (which decreases with the temperature as described in the equation of in $\rho_{inelastic}$) and gives rise to the resistivity minimum. Assuming all the temperature dependent scattering processes, like electron - phonon, electron-magnon, and electron-electron which are adequately described by the single power law, inelastic resistivity also can describe as,

$$\rho_{inelastic} = \rho_n T^n \quad \textbf{.....(3)}$$

In this equation ρ_n is the coefficient of T^n that depends upon the contribution of the inelastic scattering. Now, combining eqns (2) & (3), the equation (1) takes the form as

$$\rho = \frac{1}{\sigma_0 + BT^{1/2}} + \rho_n T^n \quad \textbf{.....(4)}$$

The effect of SHI on the modifications in the low temperature resistivity behaviour of presently studied 50 and 200nm LPBMO films subjected to different ion doses has been shown in figs 4.6(a) and (b). It can be clearly seen from the figures that, the irradiation does not have any appreciable effect on low temperature minimum in 50 nm film while in 200 nm LPBMO film the irradiation with 1×10^{12} ions/cm^2 results in a drastic increase in resistivity upturn around 50K. Also it notable that in the both the films irradiated with the ion fluence of the 5×10^{11} ions/cm^2 , resistivity is suppressed in the ferromagnetic region.

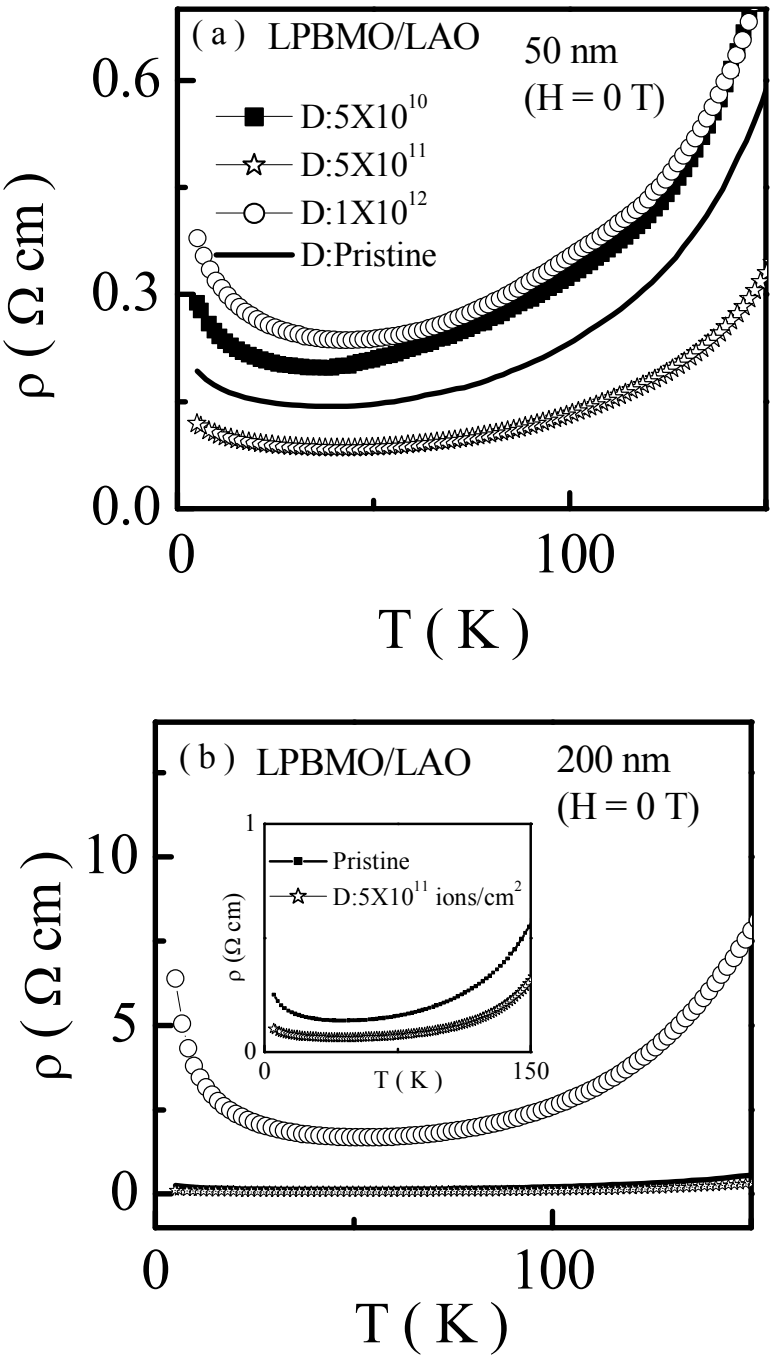

Figure 4.6. Low temperature resistivity of the 50 nm and 200 nm LPBMO manganite thin films (pristine and irradiated).

The 50nm and 200nm films irradiated with intermediate ion dose of 5×10^{11} ions/cm^2 exhibit a suppression in resistivity and resistivity minimum due to the strain release in the film which has been confirmed from the strain calculations (Table 4.2)(inset of fig.4.6: enlarged view of ρ-T pristine & 5×10^{11} ions/cm^2 irradiated film). The irradiation with ion dose ~ 5×10^{10} ions/cm^2 is not sufficient to release the strain in the film resulting in higher resistivity as compared to pristine film. At higher ion dose ~ 1×10^{12} ions/cm^2, the effect of irradiation is more pronounced as compared to strain release effect so that the resistivity becomes higher. To understand the reason for such a ρ-T behaviour, we have fitted the low temperature resistivity data of the pristine and irradiated films into eqn. (4).

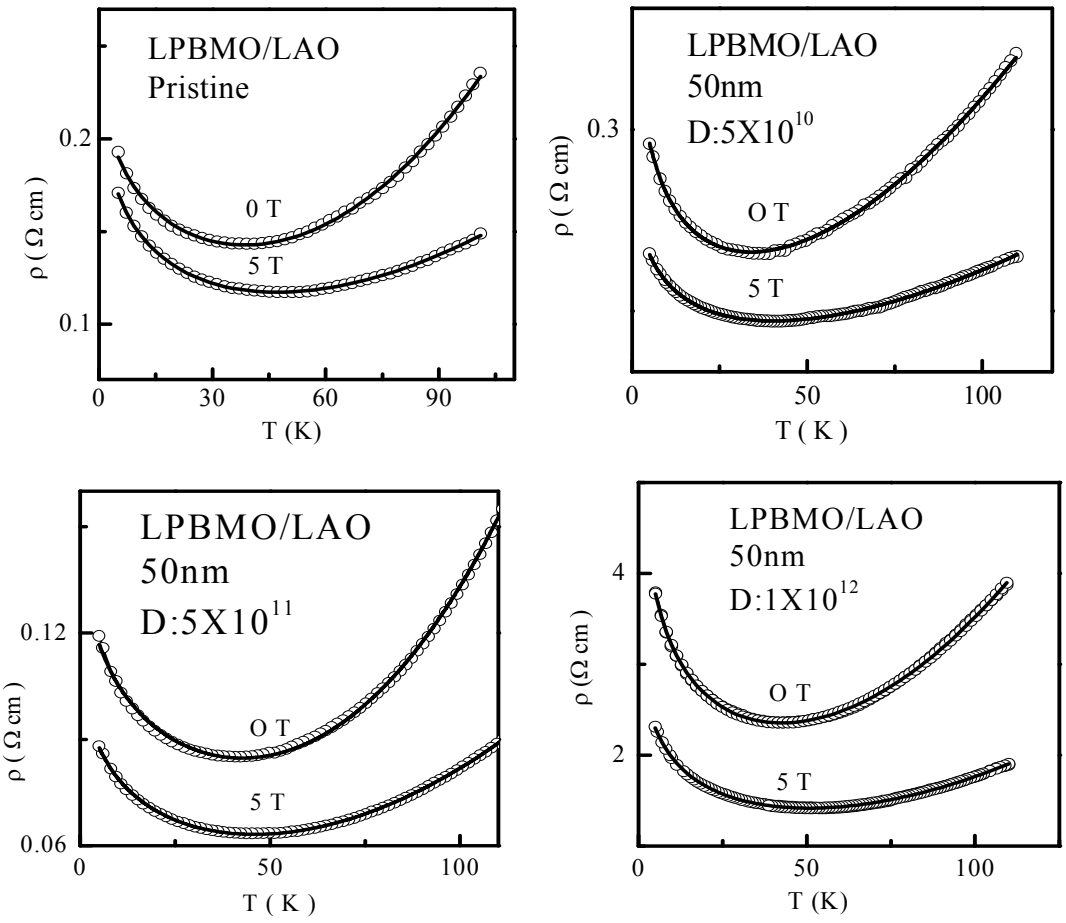

Figure 4.7: Low temperature resistivity fits to eqn.(4)for the pristine and irradiated 50nm LPBMO films with the different ion doses. The symbols are the experimental data points and the solid lines are the theoretical fits.

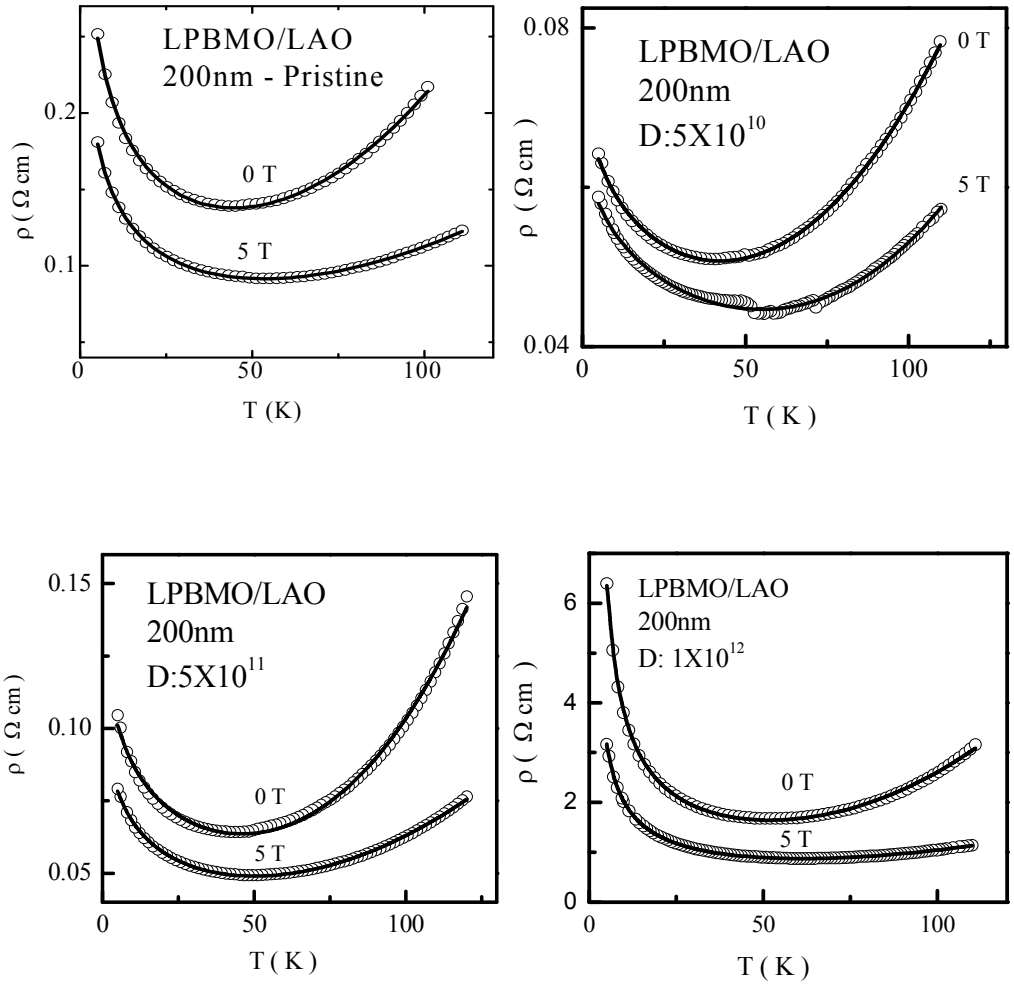

Figure 4.8: Low temperature resistivity fits to eqn.(4) for pristine and irradiated 200nm LPBMO films with the different ion doses. The symbols are the experimental data points and the solid lines are the theoretical fits.

Figures 4.7 and 4.8 shows the plots of low temperature resistivity fittings to the eqn. (4) for the pristine and irradiated 50nm and 200nm films respectively. From these figures, it can be seen that, there is no appreciable change in the low temperature resistivity minima except for intermediate (5×10^{11} ions/cm^2) and higher dose (1×10^{12} ions/cm^2) in which the minima shifts slightly towards higher temperature, which needs more attention. In the 200nm LPBMO film irradiated with 1×10^{12} ions/cm^2, broadening of resistivity minima is more pronounced as compared 50nm thin film irradiated for the same ion dose (Fig.4.8).

Table 4.3: Various fitting parameters of low temperature resistivity minimum fits to the equation $\rho = (\sigma_0 + BT^{1\backslash 2})^{-1} + \rho_n T^n$.

Ion dose	H	T_m (K)	σ_0 (Ω^{1}-cm^{-1})	B ($\Omega^{0.5}$ cm$^{0.5}$)	ρ_n (Ω cm/K^n)	n	χ^2
Sample	**LPBMO 50 nm thin film**						
Pristine	0	39	3.83	0.63	0.00002	2.38	8.80E-7
	5	49	3.93	0.85	0.00009	1.93	84.0E-7
5×10^{10}	0	33	1.90	0.70	0.00007	1.75	0.84E-7
	5	38	3.30	0.80	0.00006	1.59	2.70E-7
5×10^{11}	0	43	6.30	1.02	0.033	2.67	0.06E-7
	5	50	8.30	1.41	0.279	2.12	0.30E-7
1×10^{12}	0	45	1.42	0.54	0.00001	2.09	0.11E-7
	5	53	2.56	0.80	0.00007	2.01	4.52E-7
Sample	**LPBMO 200 nm thin film**						
Pristine	0	45	1.69	1.02	0.41	2.25	1.7E-6
	5	53	2.12	1.52	0.70	1.95	2.0E-7
5×10^{10}	0	43	12.82	1.30	3.5E-7	2.47	5.1E-8
	5	56	14.86	1.29	2.5E-8	2.90	1.4E-7
5×10^{11}	0	45	6.1	1.68	0.011	2.85	0.1E-5
	5	51	7.9	2.21	0.116	2.20	0.1E-6
1×10^{12}	0	52	-0.109	0.117	7.882E-8	2.66	0.00061
	5	63	-0.121	0.200	0.00002	2.16	0.00001

Table - 4.3 lists the values of various parameters derived form the fitting of the eqn. (4), for all the pristine and irradiated LPBMO films studied. The elastic term (first term) in the eqn. (4) dominates at low temperature while the inelastic term dominates at high temperature (~ T_p). Hence low temperature resistivity behavior seems to be arising due to the interplay between elastic and inelastic term which keeps the resistivity to minimum. Figures 4.7 & 4.8 and Table 4.3 clearly indicates that T_m shifts to higher values with increasing field which may be understood in terms of magnetic field induced suppression of inelastic scattering due to suppression of spin fluctuations [14].

From Table 4.3, it can be observed that, for 50nm LPBMO film irradiated with different ion doses, the values of residual conductivity σ_0 and diffusion constant B are maximum at 0 & 5T fields for an ion dose of 5×10^{11} ions/cm^2 compared to pristine and other irradiation doses. Similar behaviour has been reflected in the values of inelastic resistivity parameters (n & ρ_n). Here, it should be mentioned that, the inelastic term in resistivity represents the quality of conductivity in the ferromagnetic metallic (FMM) region below T_C in the manganites. The anomalous suppression of low temperature resistivity in the 50nm films irradiated with 5×10^{11} ions/cm^2 can be explained in terms of the prominent role of inelastic scattering mechanism in the FMM region which is reflected from the increase in the values of n & ρ_n. This observation indicates that, in the film irradiated with an intermediate ion dose (5×10^{11} ions/cm^2), the disorder is reduced due to release of substrate induced strain in the dead layer. The explanation for the increase in the resistivity of the 50nm film irradiated with 5×10^{10} and 1×10^{12} ions/cm^2 dose is as follows. The values of σ_0 and B decreases in the films irradiated with the above mentioned ion doses, as compared to pristine film due to the defects created as a result of irradiation, acting as scattering centers which causes electron localization more effectively which results in the enhancement of resistivity at low temperature.

In the case of 200nm LPBMO film, notable broadening effect in the low temperature minima curve is observed in the film irradiated with 1×10^{12} ions/cm^2 dose which can be understood in terms of the irradiation induced defects in the metallic region resulting into magnetic inhomogeneity in the FMM region which in turn suppresses the role of inelastic term in the low temperature resistivity behaviour.

4.1.2(B): Magnetoresistance

The disparity in the transport properties of pristine and irradiated LPBMO films with different thicknesses is corroborated by MR measurements. The MR vs. H(T) isotherms obtained from the variation of resistivity in varying applied fields at different temperatures for the 50 & 200nm LPBMO films irradiated with 5×10^{10} and 1×10^{12} ions/cm^2 doses are shown in fig.4.9. It can be seen that, the 5×10^{10} ions/cm^2 irradiated film, shows MR ~ 90 % at 195K while at 5K, it becomes <30 %, which indicates the absence of intergrain tunneling MR in thin films. It also signifies the high quality epitaxial single-crystalline structure of the thin films. Observed larger MR in the LPBMO system is due to the large size-disorder which causes the local structural distortion resulting in to random displacement of oxygen from their crystallographic positions.

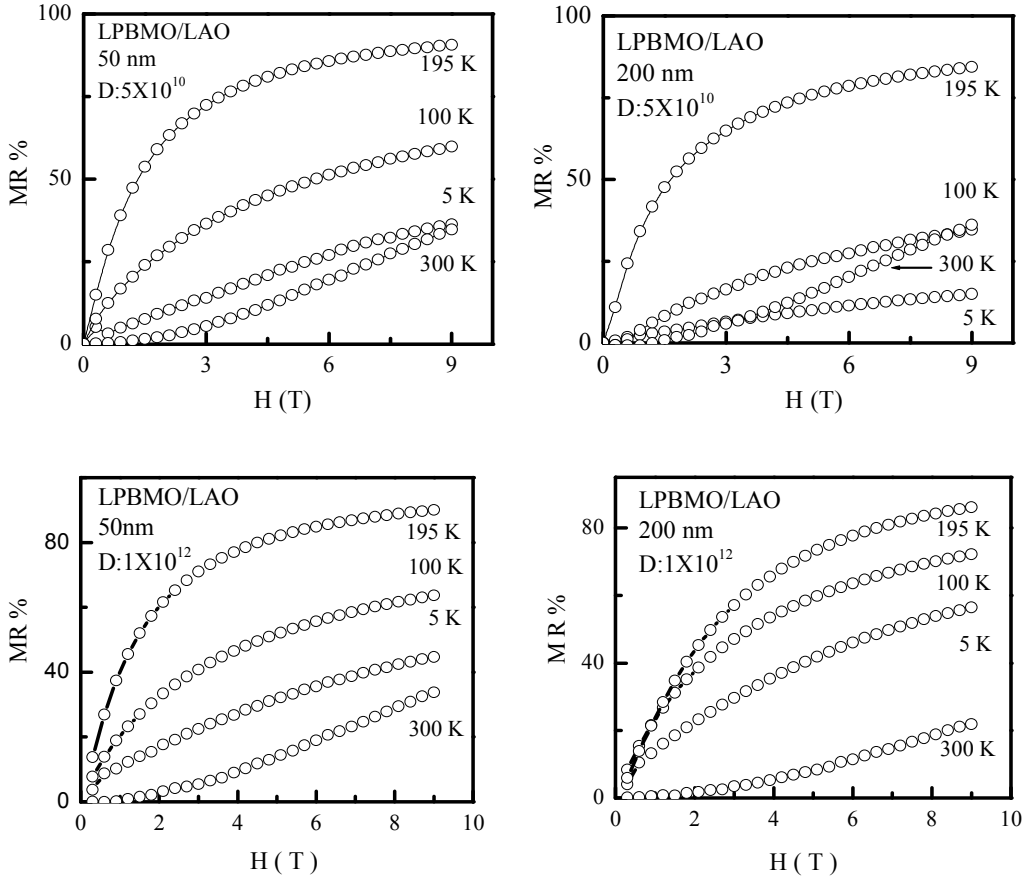

Figure 4.9: MR% vs. H(T) isotherms for the LPBMO 50 nm and 200nm irradiated films.

Figure 4.10 depicts the MR vs. H(T) isotherms at 195K (around T_P) and at 5K(low temperature) for pristine and irradiated LPBMO films. The effect of irradiation on MR, in the vicinity of T_p and at low temperature is not similar in 50 & 200 films. In 50 nm films, with increasing dose, the MR remains unaffected in the vicinity of T_p, while for 200nm film the MR decreases marginally at T_p.

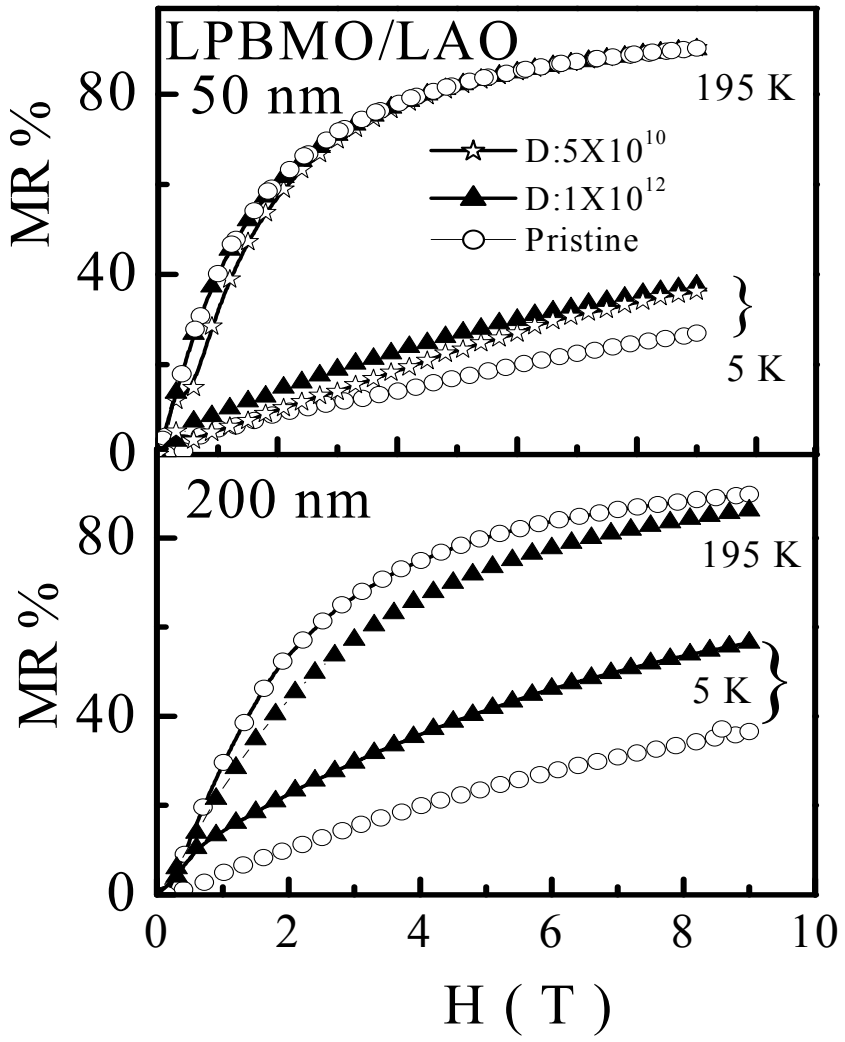

Figure 4.10: MR vs. H(T) isotherms for the LPBMO 50nm and 200nm films (pristine and irradiated).

However, at low temperature (5K), in 200nm film, MR increases from ~30 % for pristine to ~57 % in the film irradiated with a dose of ~ 1×10^{12} ions/cm^2. This increase is large as compared to that in 50nm thin film. This irradiation induced disparity in the

enhancement of MR for the both the films supports our assumption that the irradiation creates more damage resulting into the creation of additional scattering and pinning centers in 200nm films as compared to those in 50nm thin film. As already mentioned, the irradiation increases the compressive strain (Table 4.2) and hence the low temperature MR. Similar observation is reported in the compressively strained ultra thin $Pr_{0.67}Sr_{0.33}MnO_3$ thin film in which strain induced magnetoelastic interactions play a dominant role in the magnetic anisotropy [15, 16].

4.1.3: Thickness dependent irradiation effect

The origin of irradiation induced thickness dependent disparities in the transport properties of pristine and irradiated LPBMO films can be understood by studying the formation of defects due to the passage of swift heavy ions through the thin film and its effect at different thickness in the film. Picture 4.6 shows a simulation (using the SRIM 2003 software), describing this effect in manganite thin films.

It is known that, swift heavy ions create columnar defects while passing through the material and these defects in manganites act as scattering centers for conduction of carriers. Therefore, the detrimental effect of columnar defects tends to increase the resistivity and decrease the I-M transition temperature [4, 17]. Here, it may be mentioned that the damage caused by the energetic ions is thickness dependent. The columnar tracks produced by energetic ions are straight and their diameter is very small for initial small thickness of the film. As the energetic ion keeps loosing energy with increasing thickness, track diameter increases and the linearity of the track is not maintained. With increasing thickness, probability of the scattering and collision of highly charged energetic ions with the matter is large in different directions resulting in the creation of columnar defects having large diameter thereby producing magnetic anisotropy in the well-aligned unit cell and poor conducting channels in the film (picture 4.5). This leads us to infer that the detrimental effect generated by the passage of energetic ions through the film on the resistivity will be less in 50nm thin film as compared to that in 200nm film.

The other factor which accounts for the thickness dependent irradiation effect is based on the effect of SHI on the strain at the film-substrate interface. It is known that, there exists considerable stain due to lattice mismatch between LAO substrate and

manganite thin film having the thickness < 60-70nm [18]. The presently studied 50nm LPBMO thin film on LAO substrate, is therefore, strained while the strain is released in 200nm film, owing to large thickness. When the energetic ions pass though the strained 50nm film, it locally releases the strain at the interface by reducing the structural distortion in the unit cells around its path and results in an enhancement of conductivity of this low thickness film. In contrast, this is not being true for 200nm thin film because it is strain free.

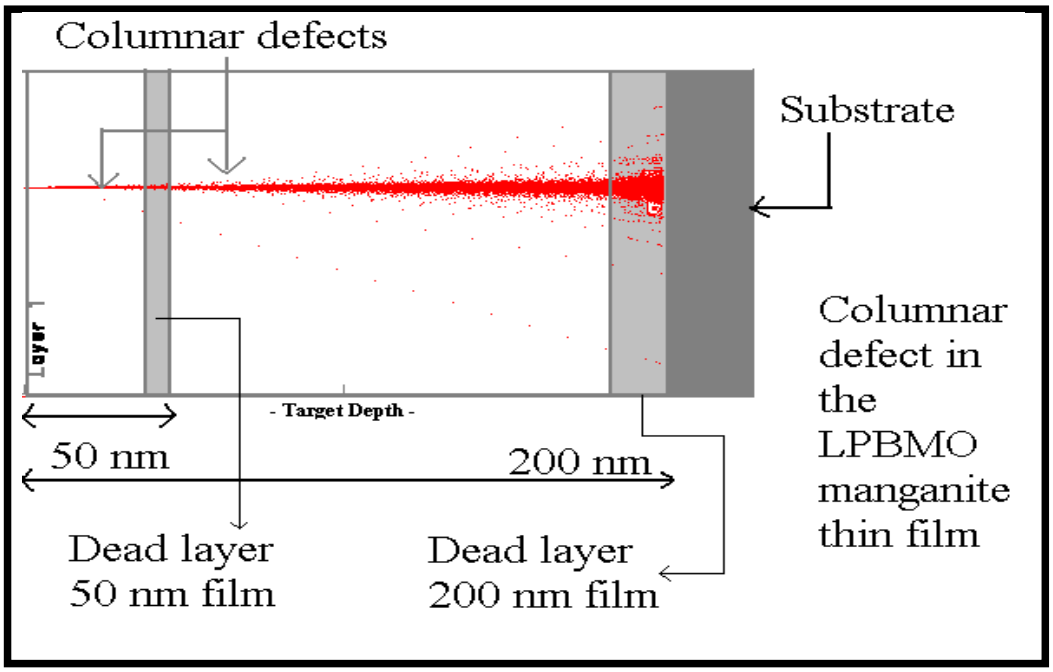

Picture 4.6: Animated path of the 200MeV Ag^{+15} ions while passing through the LPBMO manganite thin films.

4.1.4: Field and temperature sensitivity studies

Field sensitivity study

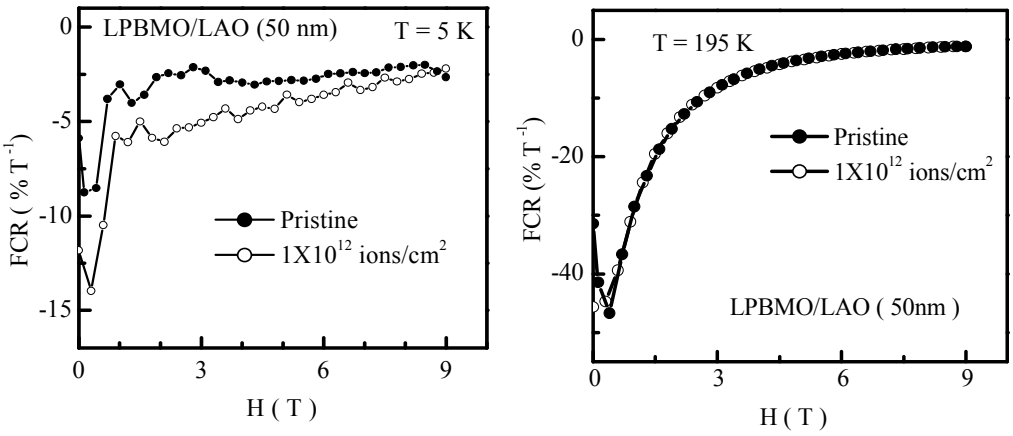

Figure 4.11: Field Coefficient of resistance (FCR) vs. field curves for the pristine and irradiated 50nm LPBMO manganite thin film.

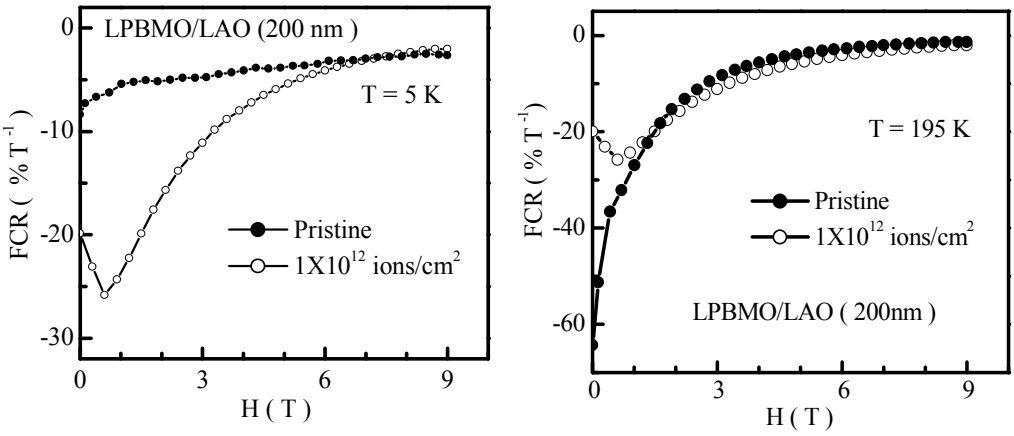

Figure 4.12: Field Coefficient of resistance (FCR) vs. field curves for the pristine and irradiated 200nm LPBMO manganite thin film.

It is well-established fact that, CMR materials exhibit the temperature dependent an antiferromagnetic/ferromagnetic (AF/F) phase transition and the appearance of the FM state is accompanied by quasi-metallic behavior at or near the T_C. Also, the application of magnetic field results into large decrease in the resistivity due to the alignment of the spins in the magnetic domains. This magnetic field sensitivity can be studied by calculating the Field Coefficient of Resistance (FCR), which is quantified

as $FCR(\%) = \frac{1}{R}\frac{dR}{dH} \times 100 T^{-1}$. The FCR values can be determined from the ρ - H plots at the different temperatures.

Figures 4.11 & 4.12 display the field dependence of FCR as a function of magnetic field, at 5K (low temperature) and 195K (at T_P) for pristine and irradiated 50 and 200nm LPBMO thin films. It can be seen that, the FCR is maximum for both the films at a field of ~5 kOe. Similar to the resistivity behaviour, there is no significant difference in the FCR values of pristine and irradiated 50nm thin films while there is a large suppression in the FCR values of 200nm thin film irradiated with an ion dose of $\sim 1\times10^{12}$ ions/cm^2 which is consistent with the irradiation induced enhanced magnetic anisotropy. In the higher dose of 1×10^{12} ions/cm^2, larger density of columnar defects formed, results in channeling effect which causes the magnetic anisotropy in the grains of thin film. This induced magnetic anisotropy reduces on application of the small field and enhanced magnetic field sensitivity of the 200nm thin films.

B. Temperature sensitivity study

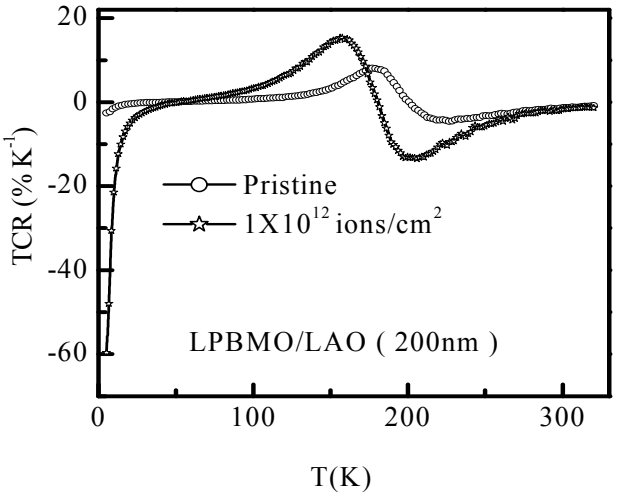

Figure 4.13: TCR vs. Temperature plots for the pristine and irradiated 200nm LPBMO manganite thin film.

Similar to FCR, the temperature sensitivity of both the films have been studied. It is quantified by a term called Temperature Coefficient of Resistance (TCR) as

$\{ TCR(\%) = \frac{1}{R}\frac{dR}{dT} \times 100\, K^{-1} \}$. In contrast to the variation of FCR due to irradiation, there is a significant change in the TCR of 200nm thin film resulting in the enhancement of TCR value to the maximum on both the positive and the negative sides of y-axis (Figure 4.13). The positive and negative TCR values of irradiated 200nm thin film with dose of 1×10^{12} ions/cm^2 are ~ 16 % K^{-1} and ~ -12 % K^{-1}, respectively, which are almost double than that of the 200nm pristine film. This feature is highly useful for the bolometric sensor applications [4, 19].

4.1.5 Conclusions

The thickness dependent irradiation effects on the structural, electronic transport and magnetotransport properties of $La_{0.5}Pr_{0.2}Ba_{0.3}MnO_3$ (LPBMO) thin films have been investigated. As result of the XRD, AFM, resistivity and magnetoresistance measurements on the pristine and Ag^{+15} ion irradiated LPBMO/LAO films having 50 & 200 nm thickness, the following conclusions have been made. From the XRD measurements, it is confirmed that, there is no structural transition or damage in irradiated thin film up to higher doses. The strain values calculated from XRD data suggests, that, on irradiation, the compressive strain increases more effectively in the 200 nm film as compared to 50 nm film. In the case of irradiated film with ion dose of 5×10^{11} ions/cm^2, strain is released due to irradiation. Also it shown that irradiation creates a similar effect on the surface of both the films which can be clearly seen form the AFM pictures of irradiated thin films.

It is shown that, with increasing irradiation dose, there is significant enhancement in resistivity and decrease in T_p of the 200nm film while there is no appreciable change in the properties of 50nm film.

The low temperature resistivity minimum in LPBMO bulk and thin films is due to the e-e scattering arising due to the metallic disorder in the sample. The large size-disorder also plays a major role in structural distortion. This result indicates that in the film irradiated with the intermediated dose (5×10^{11} ions/cm^2), disorder is reduced which is mainly due to higher strain in the dead layer. This may be due to decrease in the surface energy of the dead layer by swift heavy ions irradiation. This is reflected in the increased contribution of the inelastic term in the fitting of the resistivity data. In the

higher irradiation dose, large defects created in the metallic region introduce the magnetic inhomogeneity in the ferromagnetic region which reduces the role of inelastic term. This effect is higher in the larger thickness film in which that broadening effect of irradiation can be seen in the low temperature minima curve of the 200nm film.

The effect of irradiation on MR in the vicinity of T_P and low temperature is not similar for 50 & 200nm films. In the 50nm film, with increasing ion dose, the MR remains unaffected in the vicinity of T_P, while in 200nm film, the MR decrease marginally at T_P. At low temperature, in the 50nm film, the effect of irradiation on MR is very marginal while change in the MR as a result of irradiation is appreciable in the case of the 200nm film.

The above findings are supported by the large change in field sensitivity parameter (FCR) values at low temperatures in 200nm film as compared to 50nm film. TCR value of the irradiated thin film with the higher ion dose increases almost double than the pristine film, the property which can be of importance for bolometric application.

There exist two probable reasons for such effects, namely (i) a larger damage generated by the energetic ions with increasing thickness, which cerates more scattering centers and enhances resistivity and (ii) the presence of columnar like tracks which may cause a local release of strain at the film-substrate interface and increase the conductivity in low thickness films.

REFERENCES

32. A. P. Ramirez
J. Phys.: Condens. Matter **9**, 8171 (1997).

33. J. M. D. Coey and M. Viret
Adv. Phys. **48** 167 (1999).

34. E. Doggoto, T. Hotta and A. Moreo
Physics Report **344** 1 (2001).

35. Ravi Kumar, R. J. Choudhary, S. I. Patil, Shahid Hussain, J. P. Srivastava and S. K. Malik
Appl. Phys. Lett. **86** 222501 (2005).

36. G. Szenes
Phys.Rev.B **51** 8026 (1995).

37. J. F. Ziegler and J. P. Biersack
Program SRIM (2003), http://www.srim.org.

38. D. S. Rana, K. R. Mavani, C. M. Thaker, D. G. Kuberkar, Darshan C. Kundaliya and S. K. Malik
Journal of Mag. and Mag. Matrials **271** 215- 223 (2004).

39. J. Rodriguez_Carvajel
FULLPROF version 3.0 Laboratorie Leon Brillioun, CEA-CNRS, (1995).

40. A-M Haghiri-Gosnet and J-P Renard
J. Phys. D:Appl. Phys. **36** R127-R150 (2003).

41. J. H. Markna, R. N. Parmar, D. G. Kuberkar, Ravi Kumar, D. S. Rana and S. K. Malik
Appl. Phys. Lett. **88** 152503 (2005).

42. S. K. Singh, S. B. Palmer, D. M. Paul and M. K. Lees
Appl. Phys. Lett. **69** 263 (1996)

43. D. K. Petrov, L. Krusin-Elabaum, J. Z. Sun, C. Field and P. R. Duncombe
Appl. Phys. Lett. **75** 995 (1999).

44. A. Tiwari and K.P. Rajeev
Solid State Commun. **111** 33(1999).

45. D. S. Rana, J. H. Markna, R. N. Parmar, D. G. Kuberkar, P. Raychaudhuri, J. John and S.K. Malik
Phys. Rev. B **71** 1 (2005).

46. H. S. Wang and Qi. Li
Appl. Phys. Lett. **72** 1775 (1998).

47. F. Tsui, M. C. Smoak, T. K. Nath and C. B. Eom
Appl. Phys. Lett. **76** 2421 (2000).

48. S. B. Ogale, Y. H. Li, M. Rajeswari, L. Salamanca Riba, R. Ramesh, T. Venkatesan, A. J. Millis, Ravi kumar, G. K. Mehta, Ravi Bathe and S. I. Patil
J. Appl. Phys. Lett. **87** 4210 (2000).

49. J. Z. Sun, D. W. Abraham, R. A. Rao and C. B. Eom
Appl. Phys. Lett.**74** 3017(1999).

50. Young Sun, M. B. Salamon and S. H. Chun
J. Appl. Phys. **92** 3235 (2002).

Chapter - 5

5.1 Studies on LPSMO/Al_2O_3/LPSMO heterostructure

The observation of colossal magnetoresistance (CMR) effect in the $La_{0.67}Ca_{0.33}MnO_3$ (LCMO) manganite thin films sparked the growth and development of spin-electronics based studies in this material. It has also opened up a new direction for research and development in the field of thin film and multilayer structures of LCMO and its variants [1, 2]. The development of new spin-electronic devices such as magnetic random access memories (MRAM) to be used in conjunction with or as replacements for EEPROM (electrically erasable programmable read-only memory), flash memories in computer applications and uncooled infrared imaging systems were possible due to the growth and studies on rare earth doped manganite thin films and multilayers [3, 4]. It is well known that, the physical properties of thin films are governed by the strain induced due to the lattice mismatch occurring between the film and the single crystal substrate. It is therefore of prime interest to control the internal microstructure after deposition in order to understand the changes in both magnetic and electrical properties. Pulsed Laser Deposition (PLD) technique has been abundantly applied for the deposition of the high quality manganite thin films and multilayer. It has played a significant role in advancing the understanding of the physics of thin film structures. There is an appreciable effect of the growth parameters (such as temperature, pressure, and target-to-substrate distance) on both internal microstructure and surface morphology [5-7]. The strain in the manganite films is expected to create the magnetic anisotropy and a dead layer, which modifies the Low Field Magnetoresistance (LFMR) very effectively and can result in to loss of the spin polarization [8].

An improved MR has been observed in granular films, multilayers, spin polarized tunneling junctions and grain boundary devices [9]. Enhancement of MR at low temperature in the $La_{0.67}Ca_{0.33}MnO_3/SrRuO_3$ superlattice was reported which has been explained by the induced magnetic non-uniformity near the interfaces due to disorder [10]. $La_{0.67}Ca_{0.3}MnO_3/SrTiO_3$ multilayers exhibit large magnetoresistance of more than ~ 85% at temperatures below 100K [8]. A. Venimadhav et al fabricated the multilayer consisting of $La_{0.67}Ca_{0.33}MnO_3$ as ferromagnetic layer and $Pr_{0.7}Ca_{0.3}MnO_3$ and $Nd_{0.5}Ca_{0.5}MnO_3$ as the spacer layers and showed that the enhanced magnetoresistance could be attributed to the induced double exchange in the spacer layer which gave rise to

a larger number of conducting carriers [11]. We have used a non-magnetic spin scattering barrier of Al_2O_3 between two ferromagnetic $La_{0.5}Pr_{0.2}Sr_{0.3}MnO_3$ (LPSMO) layers with an aim to improve the electronic and magneto-transport properties of such a heterostructure grown on $SrTiO_3$(STO) single crystal substrate by Pulsed Laser Deposition. We studied the electronic-transport and magneto-transport properties of the LPSMO/Al_2O_3/LPSMO heterostructure wherein Al_2O_3 was expected to act as an insulating spacer layer separating the two parts of the ferromagnetic LPSMO film. The additional scattering centers provided by the insulating barrier could be controlled by the external applied magnetic field, which was supposed to result into an enhanced MR arising due to spin scattering. In addition, we also investigated the field and temperature sensitivity of the heterostructure incorporating the insulting barrier layer. The results of these studies are presented and discussed in this chapter.

5.1.1 Synthesis

The polycrystalline bulk target of $La_{0.5}Pr_{0.2}Sr_{0.3}MnO_3$ (LPSMO) and Al_2O_3 were synthesized using conventional solid-state reaction method. The details of bulk sample preparation have been reported in ref. [12]. Single crystalline LPSMO thin films and LPSMO/Al_2O_3/LPSMO heterostructure have been deposited by Pulsed Laser Deposition (PLD) technique under the similar experimental conditions.

Heterostructure was fabricated using the Al_2O_3 as a spacer layer having thickness of 10 Å and ferromagnetic LPSMO layers having thicknesses of ~500 Å. The Al_2O_3 spacer layer was in the middle of this thickness. We also deposited the LPSMO films having a thickness of ~500 Å under similar growth condition, to compare their characteristics with that of the three layered heterostructure having Al_2O_3 scattering barrier. Third harmonic (355 nm) of a Q-switched Nd: YAG laser having pulse duration of ~ 6 ns and fluence of about 2.1 J/cm^2 at 10 Hz repetition rate was used for the ablation of the LPSMO and Al_2O_3 targets alternately. The ejected plume was deposited on the polished (*100*) $SrTiO_3$ (STO) single crystal substrate positioned at a distance of about 5 cm from the target. The deposition was carried out at the substrate temperature of ~ 740^o C in oxygen ambient at a partial pressure of about 400 mTorr. (Details are given in the chapter 3).

The structure of the samples was analyzed using X-ray diffraction (XRD) and surface morphology was studied using Atomic Force Microscopy (AFM). The resistivity was measured as a function of temperature in range of 5-320K and as a function of magnetic field recorded as 0T - 9T - (-9T) - 0T using PPMS facility at TIFR, Mumbai. Resistivity measurements were performed in the two configurations, namely, CIP (Current In Plane) and CPP (Current Perpendicular to Plane) as shown in fig.5.1.

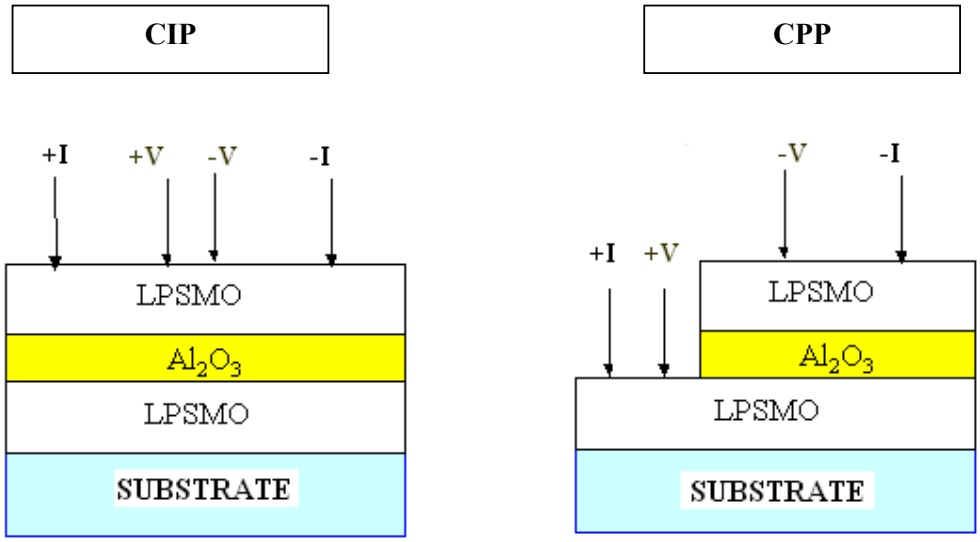

Figure 5.1: Schematic diagram of the heterostructure in the different resistivity configuration namely CIP and CPP.

Structural Studies

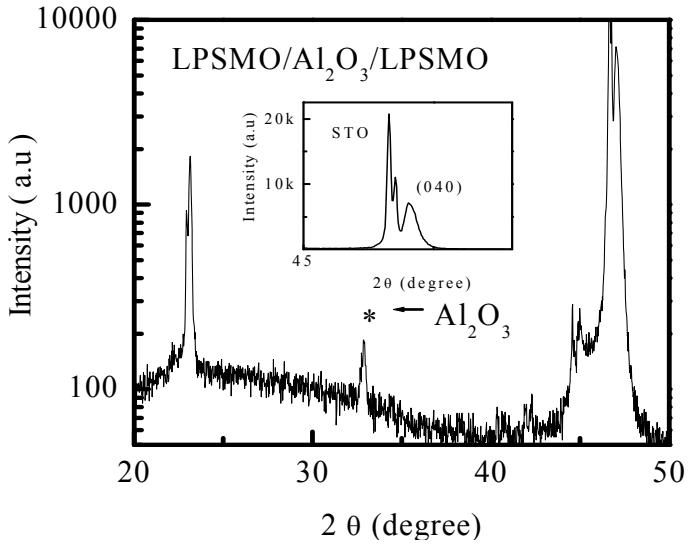

Figure 5.2: A typical XRD pattern of heterostructure. Inset of the figure show the enlarged view of indexed peak of the film.

Figure 5.2 shows the XRD patterns of heterostructure studied while inset figure shows the enlarged view of the indexed LPSMO peaks in the heterostructure. From the XRD pattern, it can be seen that, LPSMO layer exhibit the epitaxy in the (*0k0*) direction while Al_2O_3 peak is shown as asterisk in the XRD profile. From the XRD it is confirmed that Al_2O_3 is present in the LPSMO superlattice.

Surface Morphology

In order to explore the surface morphology of LPSMO film and the presence of Al_2O_3 barrier on it, we have obtained the AFM photograph of the LPSMO film and Al_2O_3/LPSMO bilayer on STO substrate, which has been shown in the pictures 5.1 and 5.2 as 3D images in the different scan size. Deposited Al_2O_3 has very small thickness of 10 Å, so in order to confirm whether it is deposited as a layer or as a barrier on the LPSMO layer like as percolative surface, we first deposited the LPSMO layer on the STO substrate and took an AFM photograph and after depositing Al_2O_3 we again took the AFM photograph of the insulting Al_2O_3 layer. From both the AFM pictures (5.1 & 5.2), it can be clearly seen that, the deposition of Al_2O_3 material results into the filling up of coarser LPSMO film surface, which is evident from the improvement in surface roughness of the Al_2O_3/LPSMO/STO bilayer as compared to LPSMO/STO film.

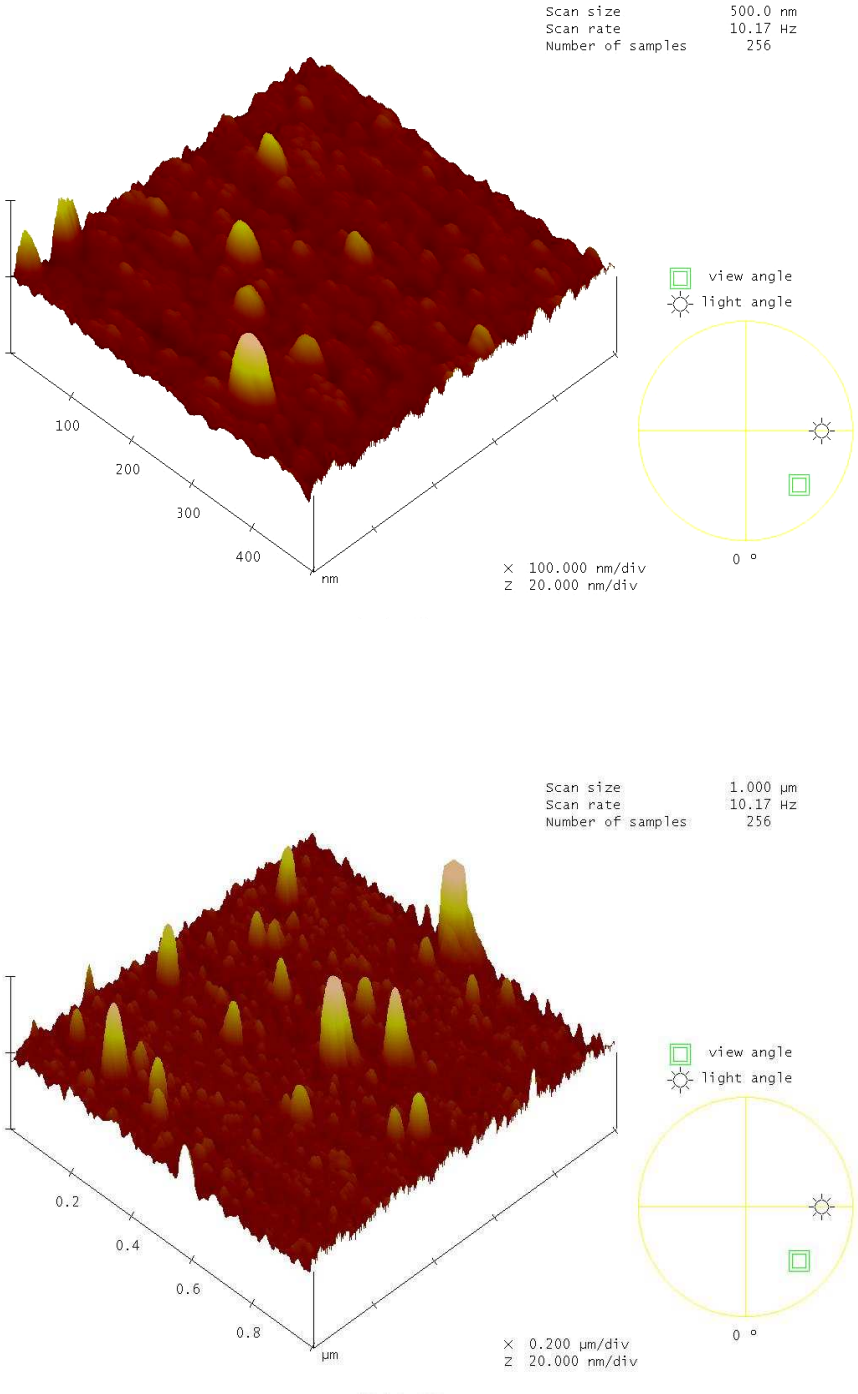

Picture 5.1: 3D AFM images of the LPSMO 50nm layer in the heterostructure with different scan size of 500nm and 1.00µm.

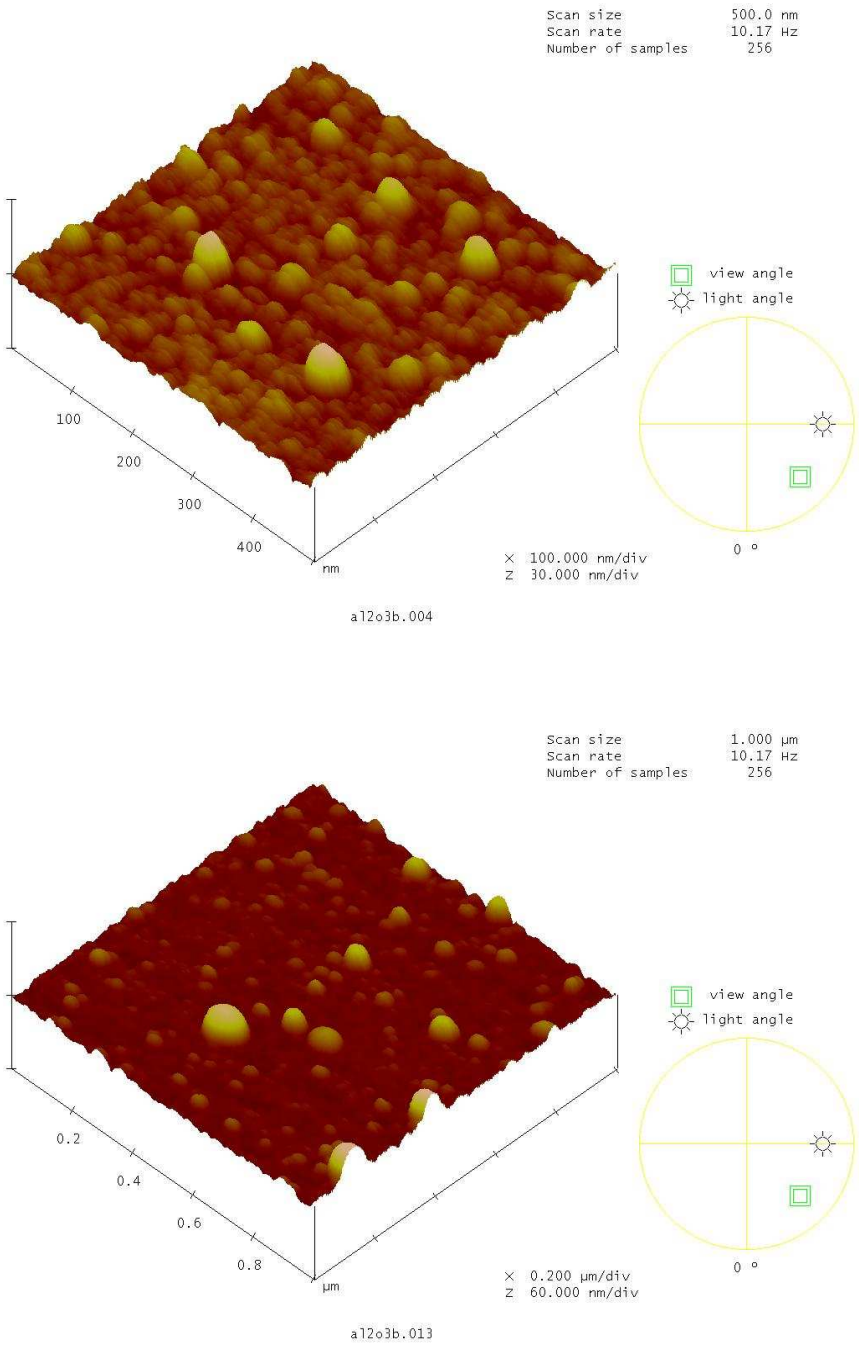

Picture 5.2: 3D AFM images of the Al_2O_3 insulating barrier on the LPSMO layer in the heterostructure with different scan size of 500nm and 1.00µm.

5.1.2 Electrical Resistivity (CIP & CPP Mode), Magnetoresistance and I-V Characteristics Studies

Electrical Resistivity (CIP & CPP Mode)

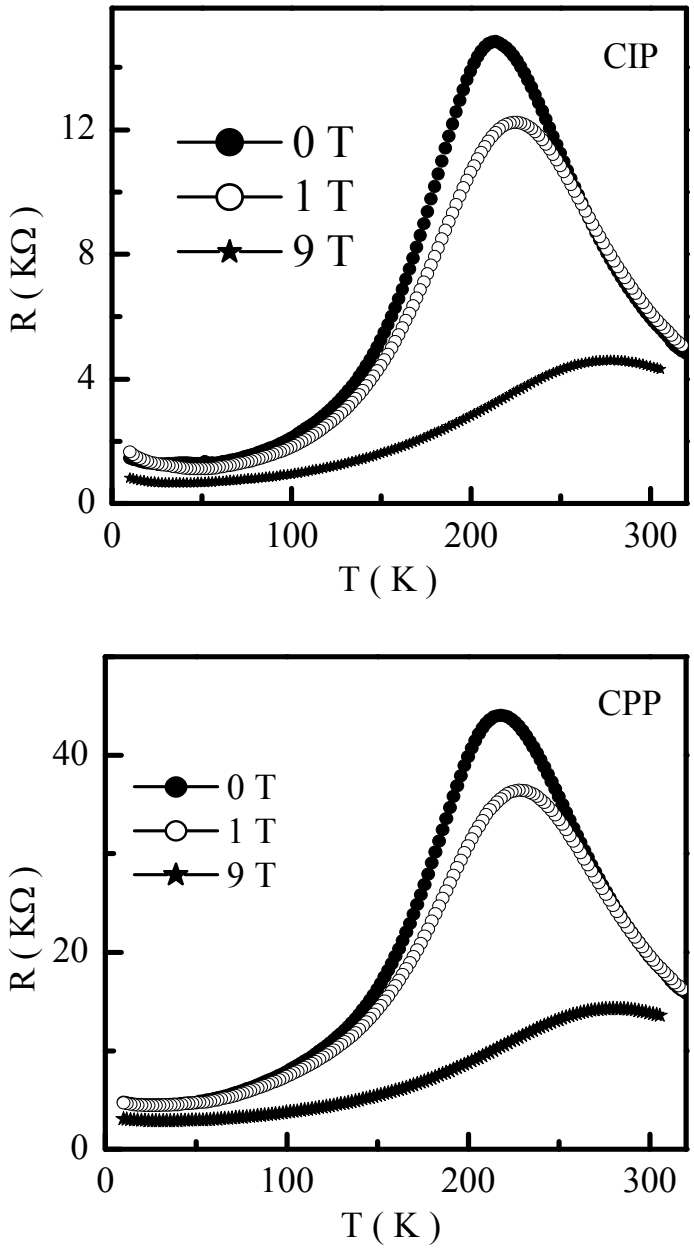

Figure 5.3: Temperature dependence of resistance of the heterostructures in 0-5T applied fields in the CIP and CPP mode.

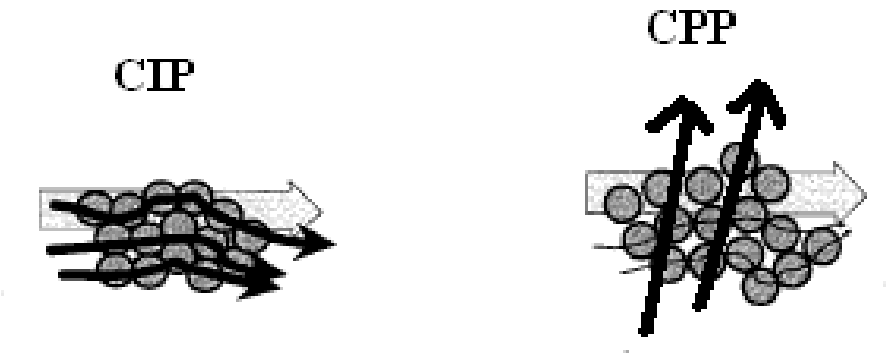

Figure 5.4: Schematic presentation of the conduction of the current in the magnetic domain (grain boundary) in the CIP and CPP mode in the heterostructures.

Figure 5.3 shows the temperature dependence of resistance behavior of the LPSMO/Al_2O_3/LPSMO heterostructure in the two different measuring configurations namely CIP and CPP mode, in applied fields of 0, 1 & 9T. It can be seen that heterostructure exhibit the T_{IM} at 212 K with peak resistance (R_p) ~ 15 KΩ in the CIP mode while T_{IM} is ~ 215 K and R_p ~ 44 K in CPP mode. In both the configurations there is not much change in the T_{IM} but a large difference in the peak resistance value is observed which is due to different electron conduction mechanisms. In the CIP mode current passes through, in the plane, while in the CPP mode current passes through the plane perpendicular to film which is shown in the fig.5.4. The direction of the current is shown by the arrow. As compared to the LPSMO film which exhibits the T_{IM} ~ 298K and R_p ~ 7.5 KΩ (chapter III, page no.11), the LPSMO/Al_2O_3/LPSMO heterostructure has low T_{IM} (~ 212K) and larger peak resistance. The observed decrease in the T_{IM} in the heterostructure can be attributed to the stresses developed such as the film-substrate lattice mismatch and heteroepitaxy of the multilayer and STO substrate [13]. The enhancement in the R_p in the heterostructure is mainly due to the Al_2O_3 insulating barrier, which contributes to the spin dependent scattering thereby resulting in an increase in the peak resistance. Also, in the CIP mode, the R-T curve shows an upturn in the resistance at temperature below 50 K, the reason of which has to understood in case of multilayered structures.

5.1.2.2 Magnetoresistance

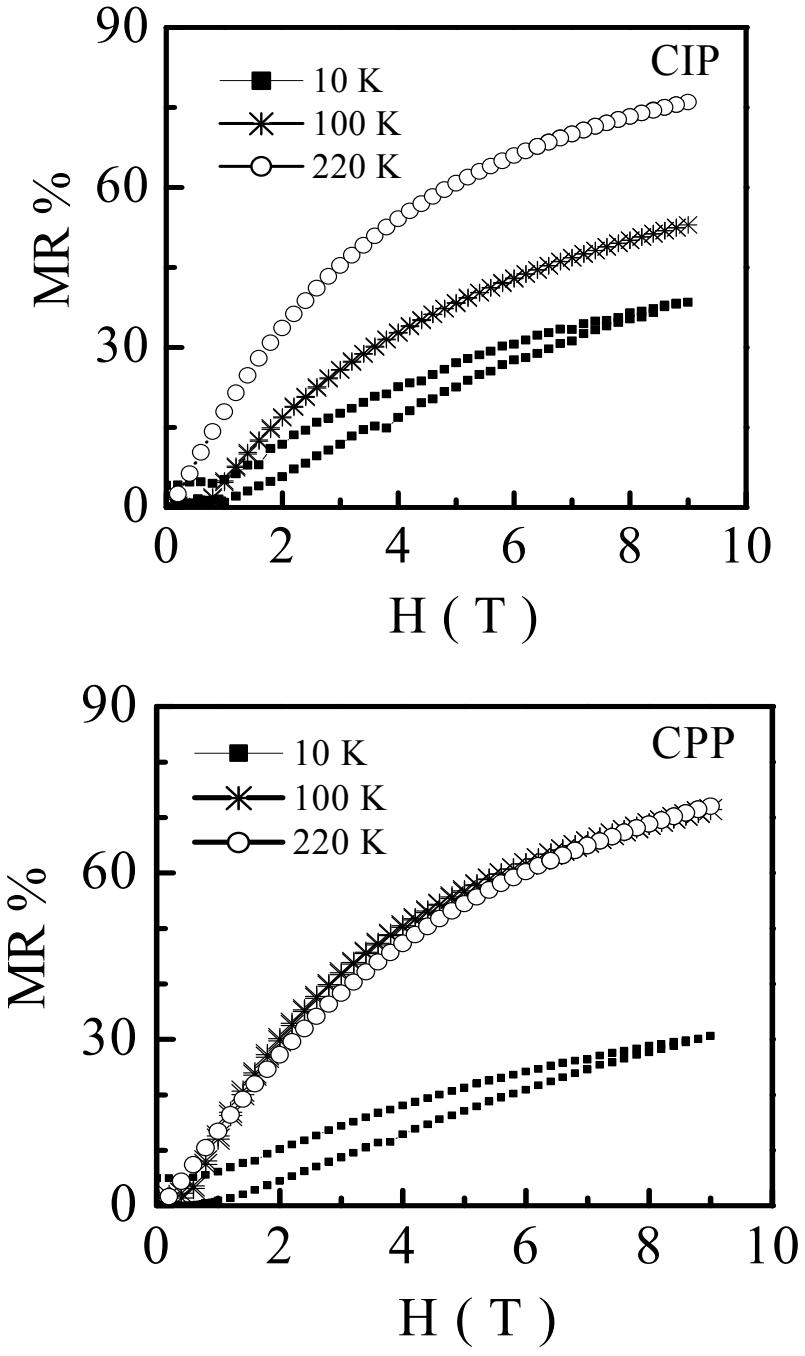

Figure 5.5: MR % vs H(T) isotherms of heterostructure in CIP and CPP mode.

We have performed electrical transport measurements on the heterostructure in the CIP and CPP mode at various temperatures in the range of 5- 320K in fields up to 9T field. The difference in the transport behaviour of the heterostructure is corroborated by MR measurements [magnetoresistance calculated as MR (%) = $(\rho_0 - \rho_H)/\rho_0 \times 100)$]. Figure 5.5 shows the MR vs. H isotherms at different temperatures for LPSMO/Al_2O_3/LPSMO heterostructure in the CIP and CPP mode, clearly depicting the following features of the MR behaviour.

Heterostructure exhibits high MR ~ 77 % and 72 % in high applied field near the T_{IM} (220K) for the CIP and CPP modes respectively. The observation of large high field magnetoresistance (HFMR) of ~77 % in this heterostructure as compared to that of LPSMO film (MR~51%) at temperatures close to their T_{IM} values, can be attributed to the spin fluctuations at the Al_2O_3 barrier between the two LPSMO layers, which are controlled by the application of magnetic field resulting in an enhancement of MR in the heterostructure. In the heterostructure, at low temperature, MR shows a hysterisis behavior indicting a percolative transport in the ferromagnetic layer via insulting Al_2O_3 barrier. This percolative transport is responsible of the high value of the MR (~ 39 %) at low temperature (10K) [14,15].

Figures 5.6. (A) & (B) shows the MR vs. T (K) plots for LPSMO/Al_2O_3/LPSMO heterostructure in the CIP and CPP mode under 1 and 9T fields. In heterostructure high MR ~ 27 % & 24 % is observed near the T_{IM} in 1 Tesla applied field while MR ~ 78 % and 80 % in 9 Tesla applied field for the CIP and CPP mode respectively. In CPP mode, below T_{IM}, under 1T field, the MR decreases with the temperature while in CIP mode, at lower temperature, there is a MR ~ 20% (up to 50K) which may due to the intergrain spin scattering at magnetic domains. Also, in CIP mode the electron transport is in parallel direction while in CPP mode it is in perpendicular direction.

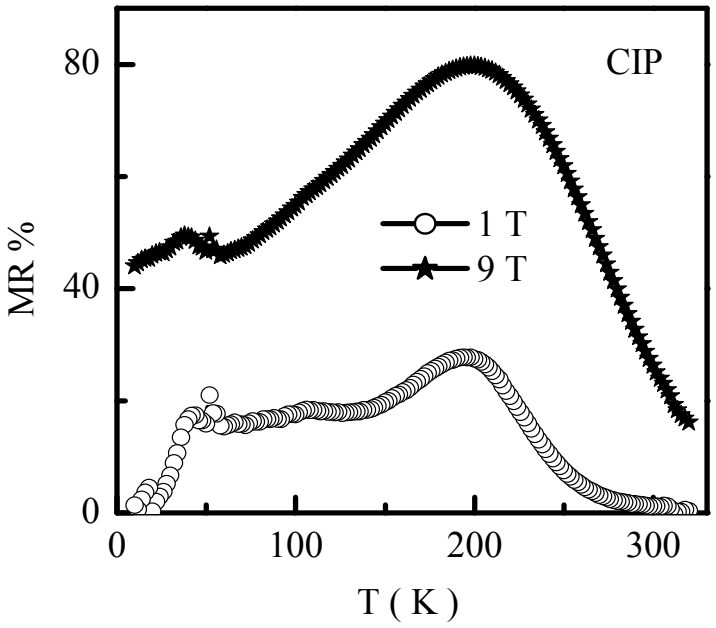

Figure 5.6 (A): MR % versus temperature for heterostructure in CIP mode in 1 and 9 Tesla magnetic fields.

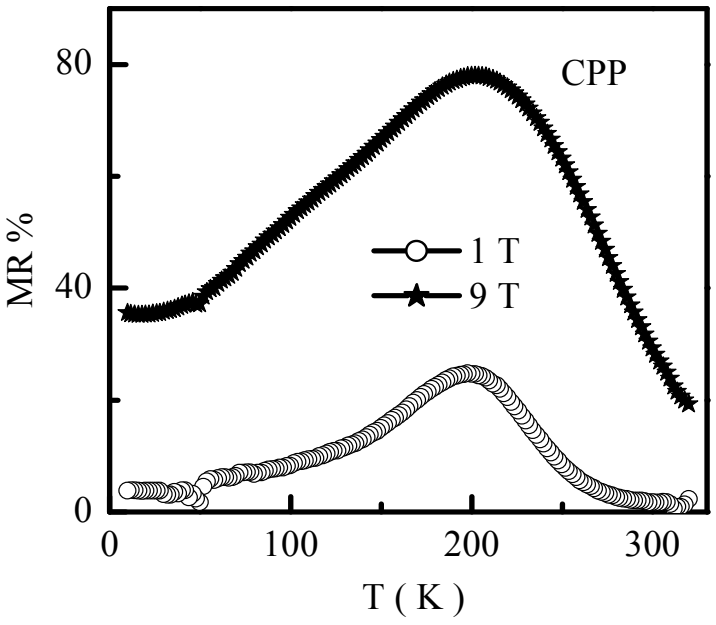

Figure 5.6. (B): MR % versus temperature for heterostructure in CPP mode in 1 and 9 Tesla magnetic fields.

I-V Characteristics Studies

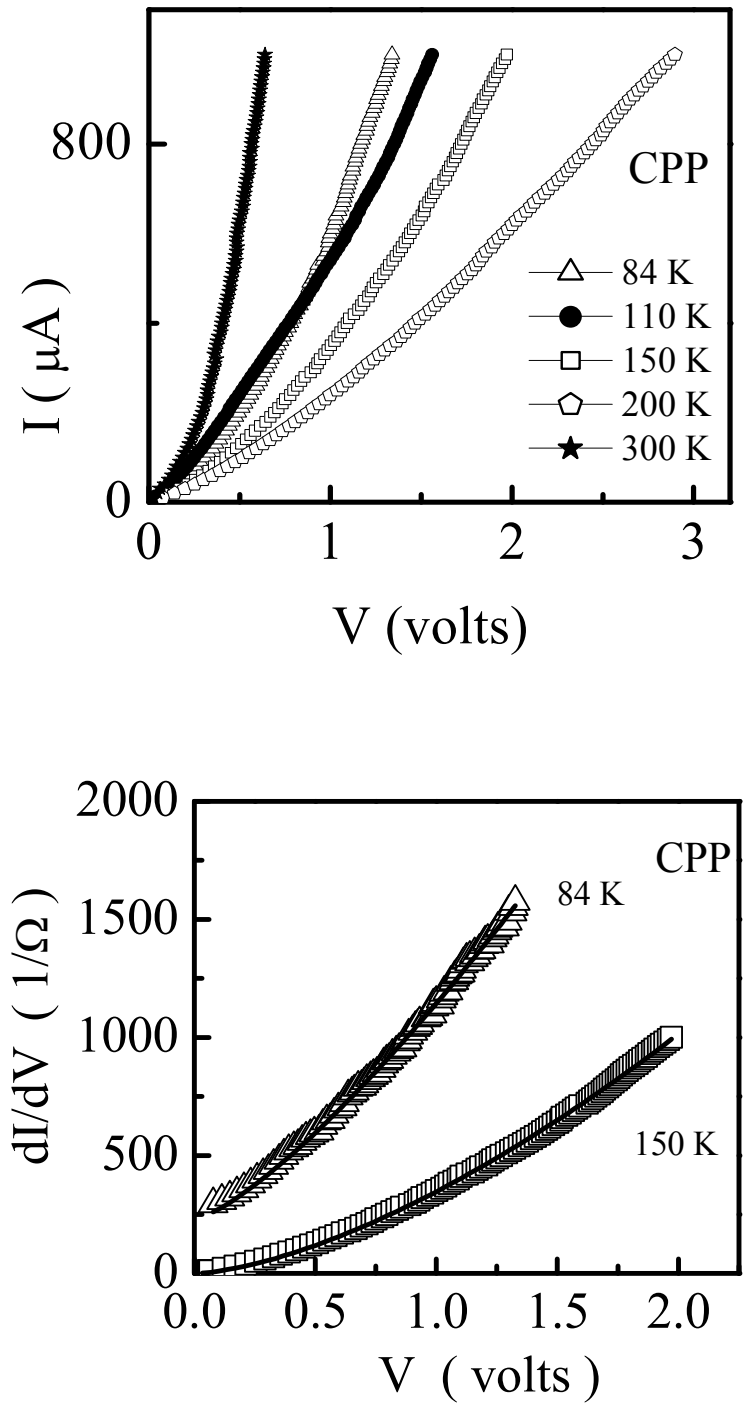

Figure 5.7: I-V characteristics and conduction vs. of voltage plots fitted in Simmon`s model for the heterostructures in the CPP mode.

To understand the effect of insulting Al_2O_3 barrier on the electronic transport of LPSMO/Al_2O_3/LPSMO heterostructure, we have studied the current-voltage (I-V) characteristics of this system using stranded four-probe technique which shows similar behavior for both negative and positive applied voltages. It has been observed that, the heterostructure exhibits a non-linear I-V behavior (Fig. 5.7), which may be due to either by distorted metallic oxide like behavior, quasiparticle tunneling via pairs of localized states or spin-flip scattering at the grain boundary [16-18]. To confirm the cause of non-linearity in the I-V behavior of heterostructure, we have fitted the conductance versus voltage curves at different temperatures for the heterostructure in the Simmon's model given by $dI/dV = a + bV^n$; where a, b and n are constants depending on magnetic field and temperature (Fig.5.7) [19]. The values of n at temperatures below T_{IM} (84 K and 150K) are grater than 1.4, which indicates that the spin-flip mechanism at the Al_2O_3 barrier is responsible for the non-linearity in I-V characteristics [18].

5.1.3 Oxygen annealing effects

The heterostructure studied shows the lower T_{IM} than the parent LPSMO thin film, which is due to large strain developed due to heteroepitaxy. To remove this strain, heterostructure was annealed at 1000 ºC for the 24 hrs in O_2 atmosphere. Figure 5.8 shows the R-T behavior of the oxygen annealed LPSMO/Al_2O_3/LPSMO heterostructure in CIP and CPP mode under 0, 1 & 5T fields in the temperature range of 2-320K. Figure 5.8 shows that, heterostructure exhibits T_{IM} at 280K with peak resistance (R_p) ~ 2.8 KΩ in the CIP mode, while T_{IM} ~ 288K and R_p ~ 4K is observed in CPP mode. Thus the oxygen annealed heterostructure show higher T_{IM} and large suppression in R_P in the vicinity of RT as compared to as deposited heterostructure which may be due to strain release at interface of the each layer or excess oxygen which favours the Zener double exchange mechanism. If we compare the nature of the insulator to metal transition, without oxygen annealing, the heterostructure show a large resistance broadning effect at T_{IM} while after oxygen annealing this effect is removed and transition becomes sharp.

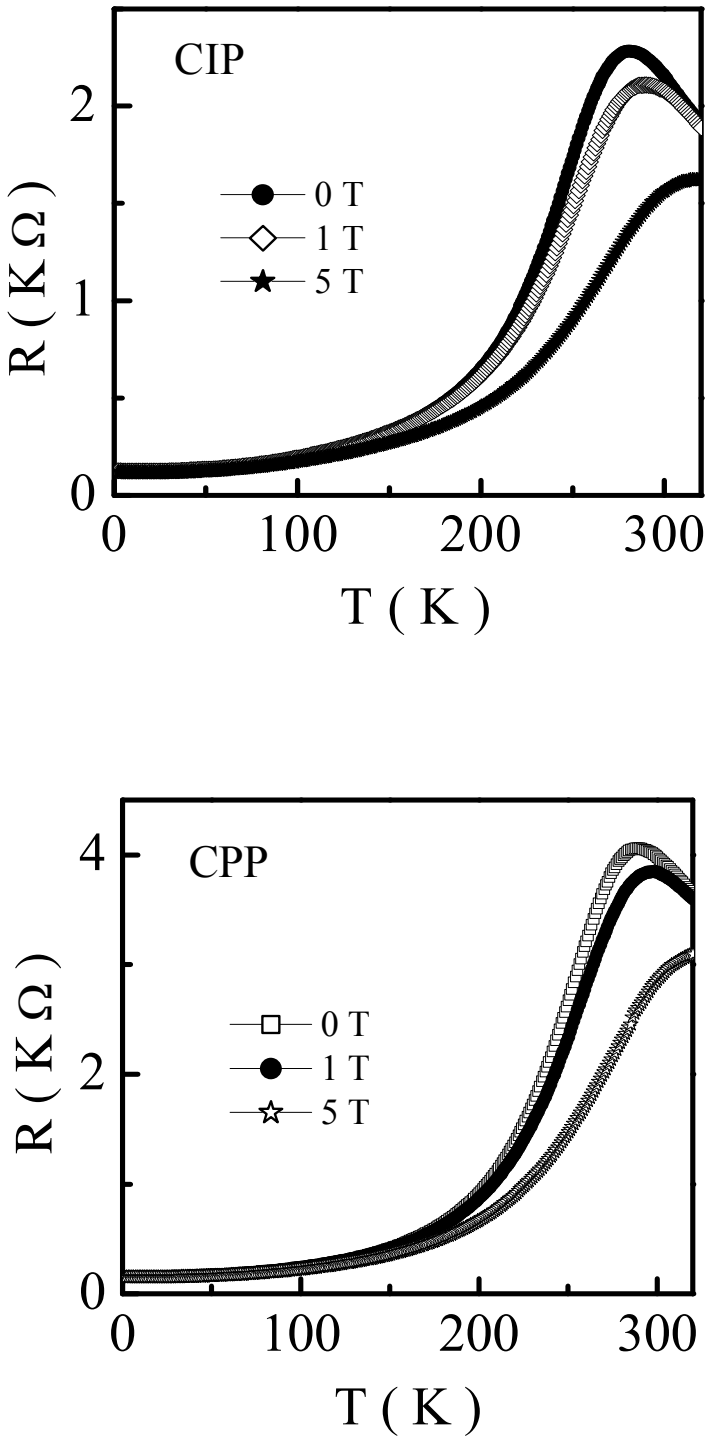

Figure 5.8: R vs. T (K) plots of the oxygen-annealed heterostructures in applied fields in the CIP and CPP mode.

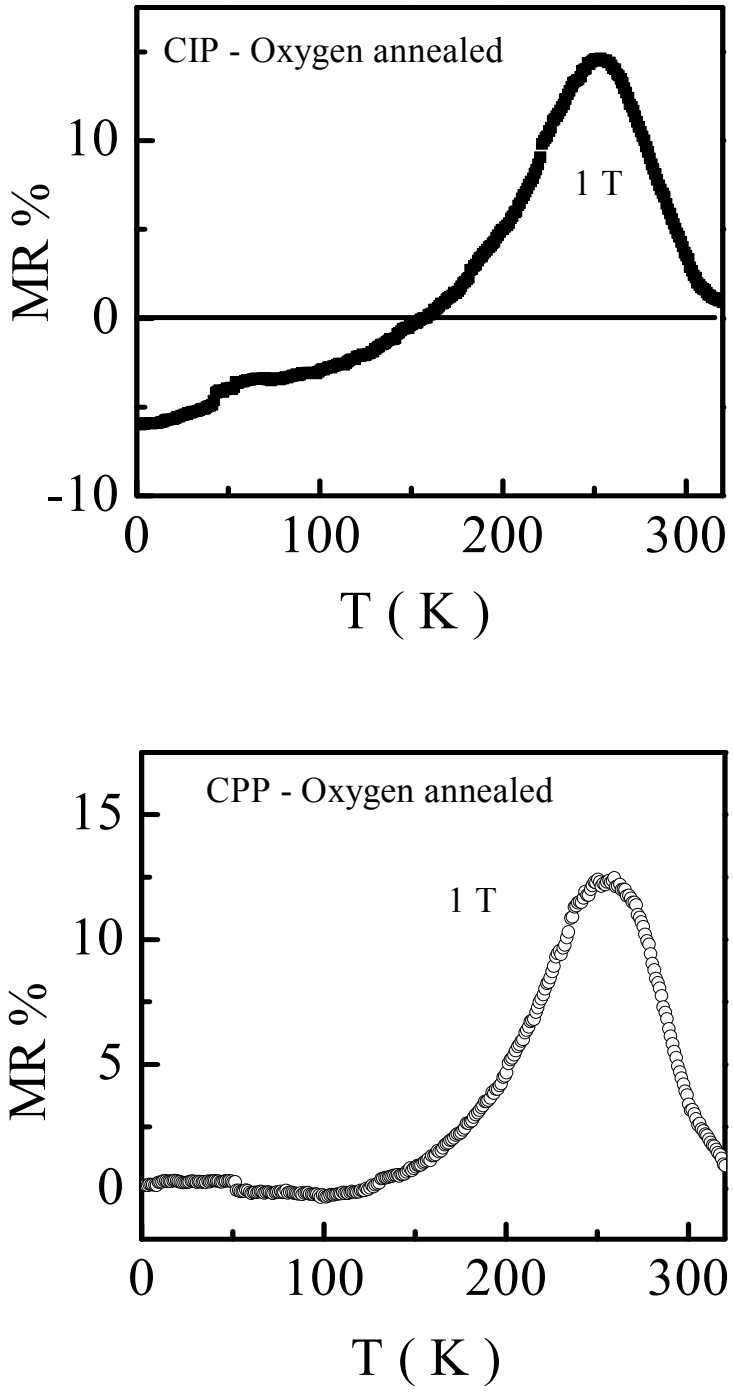

Figure 5.9: Magnetoresistance vs. temperature plots of the oxygen-annealed heterostructures in 0-5T applied field in the CIP and CPP mode.

Figure 5.9 shows the MR vs. T plots for LPSMO/Al_2O_3/LPSMO heterostructure in the CIP and CPP mode in 1 Tesla applied field. A high MR ~ 14 % and 13 % is exhibited near T_{IM} (251K) in 1 Tesla field in CIP and CPP mode for oxygen annealed heterostructure. Comparison of MR values of oxygen-annealed heterostructure with the as grown heterostructure (Fig.5.6) clearly shows that MR decreases on annealing. The observed anomalous behavior of the negative MR at low temperature below the 100 K in the heterostructure in the CIP mode is not well understood as it is not a common feature in the manganites. It can be possibly due to the quantum interference effects (QIE) reported in [20]. A major problem in dealing with ultra thin manganite thin films is the presence of the dead layer, with suppressed conducting and /or magnetic properties at the interface between the film and the substrate [21]. It can be proposed that, the observed negative MR may be possibly due to QIE related to weak localization. Moreover, the scattering by magnetic impurities and by impurities with spin-orbit coupling has been demonstrated to strongly influence the sign of the MR, rendering even more difficulty in disentanglement of the different contributions to QIE in CMR manganites. In the case of heterostructure there are many parameters such as strain, insulating impurity and heteroepitaxy, which are responsible for such behavior of MR at low temperature which favours the QIE.

5.1.4 Temperature and Field Sensitivity

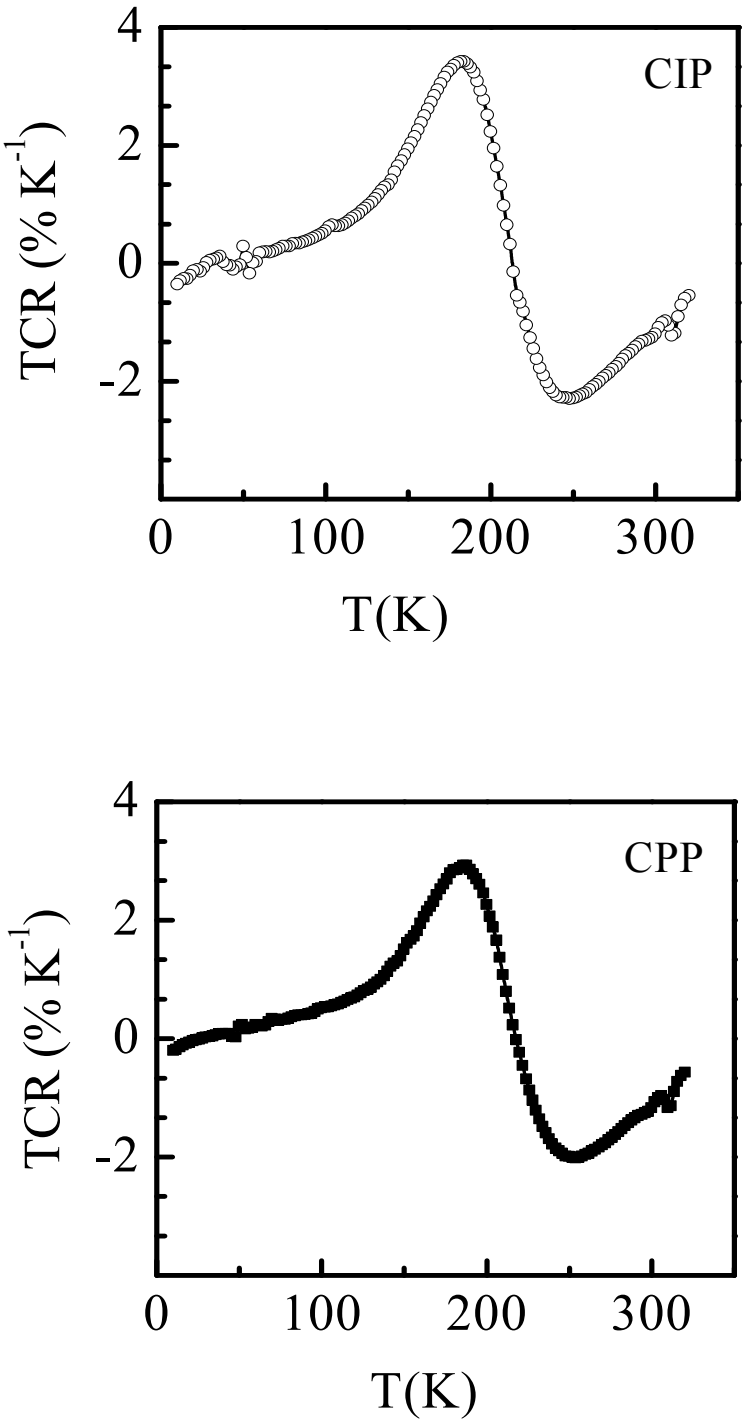

Figure 5.10: TCR vs. T plots of the heterostructures in the CIP and CPP mode.

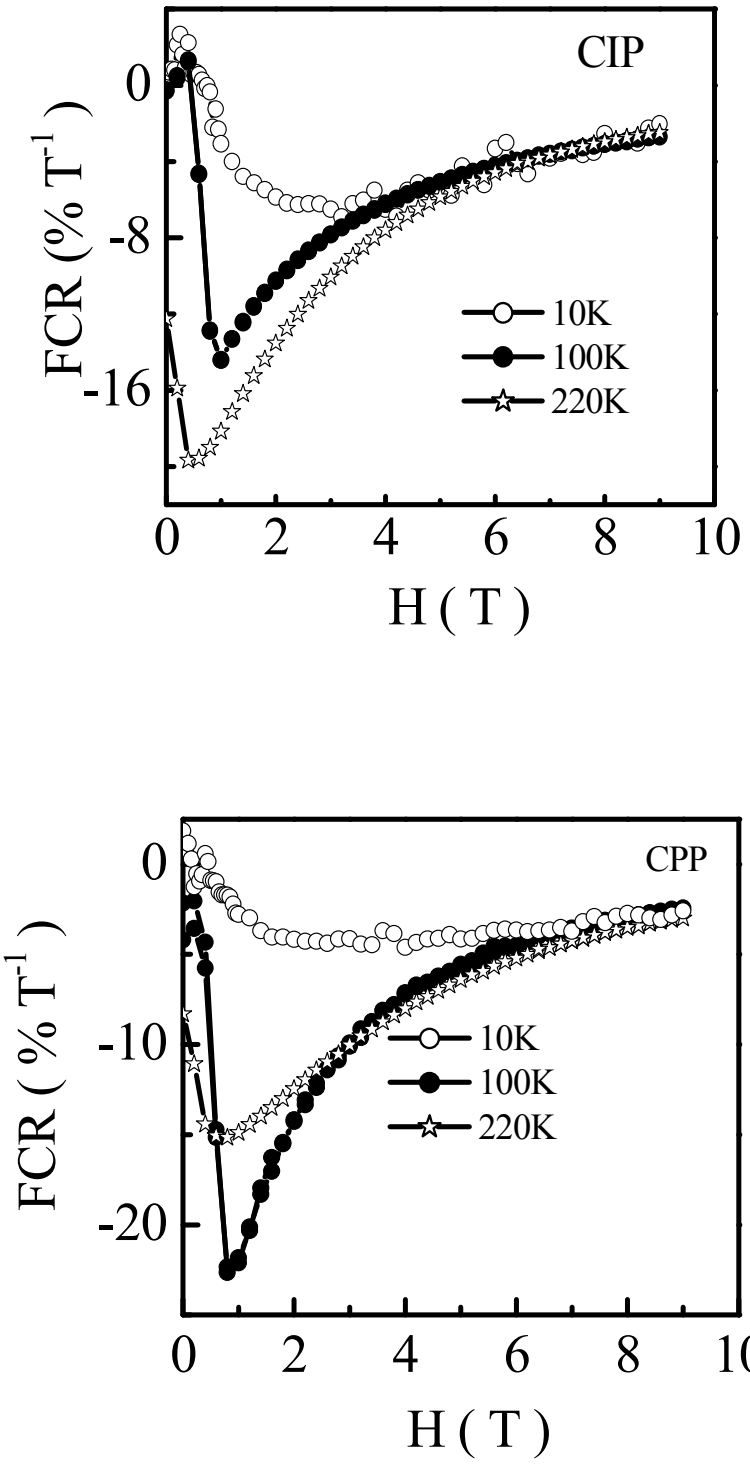

Figure 5.11: FCR vs. H (T) plots of the heterostructures in the CIP and CPP mode.

We have studied the temperature sensitivity of heterostructure, which has been quantified by Temperature Coefficient of Resistance (TCR). Figure 5.10 shows the variation of TCR with the temperature for LPSMO/Al_2O_3/LPSMO heterostructure in the CIP and CPP mode. The maximum positive TCR values are ~3.47 % K^{-1} and 2.8 % K^{-1} determined in the CIP and CPP mode. The value of maximum positive TCR ~1.51 % K^{-1} at 273 K observed the LPSMO film [chapter III, fig.3.12. (A)] becomes more than double in the heterostructure at 180 K. At room temperature, heterostructure exhibits the negative TCR value ~ -1.2 K^{-1} and -1.09 K^{-1} in the CIP and CPP mode respectively, the feature highly useful for the uncooled infrared image sensing (bolometric sensor) application [3, 4]. High $-T_c$ superconductors exhibit high TCR values but are not suitable for the uncooled bolometric applications because of their lower operating temperatures [21]. It is important to mention that commercially available bolometers based on semi-conducting YBCO or VO_X have room temperature TCR value varying from ~ 1.5 K^{-1} to 3 K^{-1}. YBCO type of cooled bolometer need to cool down to 92 K or lower while the VO_X is very difficult to synthesis with the desirable properties.

The magnetic field sensitivity of the heterostructure has been be studied by calculating the Field Coefficient of Resistance as (FCR). From the application point of view, as field sensor, it is desirable to have a large field sensitivity, which should shift, with the applied field. Figure 5.11 displays the variation in FCR with magnetic field for heterostructure at different temperatures. It can be seen that, the maximum FCR ~ -20 % at 220K in ~ 0.5 Tesla field for heterostructure in the CIP mode becomes ~ -22 % at 100K in ~ 0.7 Tesla. Observed large FCR in the heterostructures is mainly due to insulating Al_2O_3 barrier, which provides the spin dependent scattering centers, which can be controlled by applied magnetic field.

5.1.5 Conclusions

In the present study, we have grown the heterostructure of the LPSMO/Al_2O_3/LPSMO for improved electronic transport and magnetotransport properties. In the heterostructure, Al_2O_3 insulating material was deposited in between the two LPSMO ferromagnetic layers. XRD pattern shows the epitaxial growth in the (*0k0*) direction and also confirm the presence of the Al_2O_3 insulating material in the heterostructure. From the AFM study, it is clearly seen that deposited Al_2O_3 fills up the

coarser surface of the LPSMO layer. The resistance of the heterostructure was measured in both CIP & CPP modes. R-T plots of the heterostructure shows a decrease in the T_{IM} and increase in the peak resistivity by large factor as compared to parent LPSMO films which may attributed to large strain and heteroepitaxy effect, due to the number of layers in the heterostructure. Also resistance in the CPP mode is higher as compared of the resistance in the CIP mode due to different transport mechanisms involved. Observation of the large MR in the heterostructure is due to sandwiched insulting Al_2O_3 barrier between the two ferromagnetic LPSMO layers, which provides the spin scattering centers controlled by the external applied field. The appearance of hysterisis in the MR at low temperature in the heterostructure can be interpreted as due to the percolative transport via insulating barrier.

From the MR vs. T plots, it has been observed that, in the CIP mode, after the $T_{IM,}$ MR remains constant with decreasing temperature which is due to intergrain spin scattering in the manganite domain. This effect is not observed in the CPP mode due to the transport mechanism in the perpendicular direction in the magnetic domain. The I-V characteristic studies show non-liner I-V behaviour due to the spin-flip mechanism at the Al_2O_3 barrier. Also, the effect of the oxygen annealing on the MR behaviour of the heterostructure has been studied. After oxygen annealing, T_{IM} shifts towards the RT with the decrease in the MR%. As an effect of oxygen annealing, negative MR (CIP mode) is observed in the heterostructure at low temperature (below 100K) which is anomalous observation in the manganites. We feel that this effect can be explained by considering the Quantum Interface Effect which needs further investigation.

TCR value increases by a factor of two in the heterostructure as compared to the parent LPSMO thin film. Field sensitivity ~ -20 % in low applied field (0.5 T) in the multilayer is highly useful in its application as field sensor. From the present study, it is notable that spin scattering through the insulating barrier tailors the transport and magnetotransport properties of the LPSMO/Al_2O_3/LPSMO heterostructure.

5.2 Comparative study of PLD and CSD grown LCMO thin films

Interest in the studies on manganite thin films has achieved new heights after the first observation of CMR behaviour in the $La_{0.67}Ba_{0.33}MnO_3$ thin films [2]. The physical properties exhibited by these materials prompts the possibility of using them in the magnetic field sensor, magnetic read head, bolometric sensor and other applications. In all of these applications, it is necessary that manganite material should be in the thin film form..

There are several techniques reported for the synthesis of the manganite thin films out of which Pulsed Laser Deposition (PLD), Chemical Solution Deposition (CSD) and Chemical Vapor Deposition (CSD) are more commonly used. In the PLD technique, the deposition conditions such as oxygen pressure, deposition temperature, fluence size and substrate to target distance drastically affects the physical properties of the film. Also, for the PLD grown thin films, in situ or ex situ oxygen annealing is necessary to obtain the films with optimized T_{IM}, T_C and magnetoresistive properties [22-23]. The main advantages of CSD method of manganite thin film deposition are: it is very easy to synthesize epitaxial and polycrystalline manganite thin films in short time using CSD rout, it is easy to grow the film on large area with lower cost and quality of film can be improved by homogeneous growth of the material [24, 25].

In this section, we report the comparison of physical properties of the 200nm LCMO films synthesized using PLD and CSD methods. The results obtained on the effect of grain size and strain (lattice mismatch) on the transport and magnetotransport properties of both the films are discussed in detail.

Synthesis

Polycrystalline bulk target sample of $La_{0.7}Ca_{0.3}MnO_3$ (LCMO) was synthesized using standard ceramic method. The LCMO thin film with 200nm thickness was deposited on a single crystal (*h00*) oriented LAO substrate by PLD using KrF excimer Laser. The deposition parameters were: substrate to target distance ~ 4.2 cm, substrate heating temperature ~ 830 ^oC and partial oxygen pressure ~ 400 mTorr. Another LCMO film was grown on single crystalline LAO substrate using CSD technique. The mixing, stirring and heating of appropriate stoichiometric quantities of the appropriate metal

acetates in a distilled water and acetic acid resulted in a clear solution of the constituents used for deposition. Deposition of thin films using automated spin coater was then followed by heating and annealing at 1000 °C in an oxygen environment.

XRD and AFM measurements were carried out on these films for structural and microstructural properties. Electrical resistivity and magnetoresistance measurement with and without field were performed using d.c four probe technique (PPMS, Quantum Design).

5.2.1 Structure and surface morphology

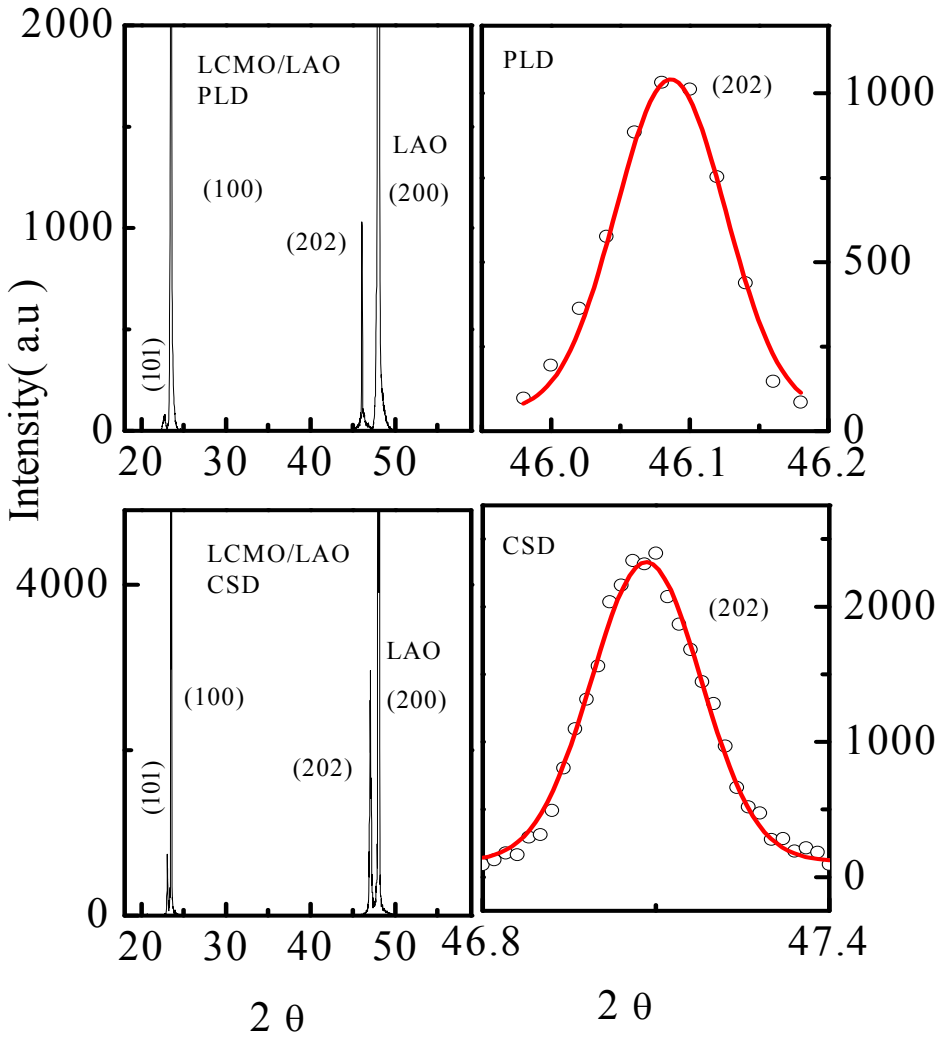

Figure 5.12: Typical XRD patterns of 200nm LCMO/LAO films grown by PLD and CSD methods.

Figure 5.12 depicts the XRD patterns of the CSD and PLD thin films showing a single-phase orthorhombic structure. The cell parameters of the bulk, a = 5.570(1) nm, b =7.736(1) nm and c =5.497(1) nm, were used to index the thin film XRD patterns. The films were found to be oriented in (*hol*) direction and are highly epitaxial. The lattice mismatch, δ, along the interface is calculated using the formula $\delta = \frac{d_{substrate} - d_{thin\ film}}{d_{substrate}} \times 100$. In the case of PLD grown film, the mismatch is ~ -3.798 % and for the CSD grown film, the mismatch is ~ -0.0179 % (Compressive strain). The value of grain size calculated using the Scherrer's formula for CSD grown film is ~ 150nm and for the PLD grown film it is ~ 400nm (figure 5.12 and Table 5.1). Also FWHM of the indexed (*202*) peak of the CSD grown film is small as compared to PLD grown film, which shows the good quality of CSD grown film without strain in it.

The surface morphology of both the LCMO films is studied using AFM measurement. The pictures 5.3 and 5.4 shows the surface topology of the LCMO/LAO thin films grown by the CSD and PLD methods respectively having grain size ~ 70nm in the CSD grown thin film while ~ 150nm in the PLD grown thin film. In the same figure, surface roughness histogram is also shown indicating RMS roughness ~ 9.3nm in the CSD grown film and ~ 17nm in PLD grown film. The comparison of the grain size and other properties of both the films is done in the Table 5.1.

Table 5.1: Comparison of grin size, T_{IM} and resistivity and FWHM of the 200nm LCMO/LAO thin film grown by PLD and CSD methods.

Sample LCMO	T_{IM} (K)	ρ at 10K (Ωcm)	ρ_{Peak} (Ωcm)	FWHM	Grain size (XRD)	Grain size (AFM)
PLD	239	0.0256	0.523	2.3nm	400nm	150nm
CSD	249	0.0004	0.077	0.99nm	170nm	70nm

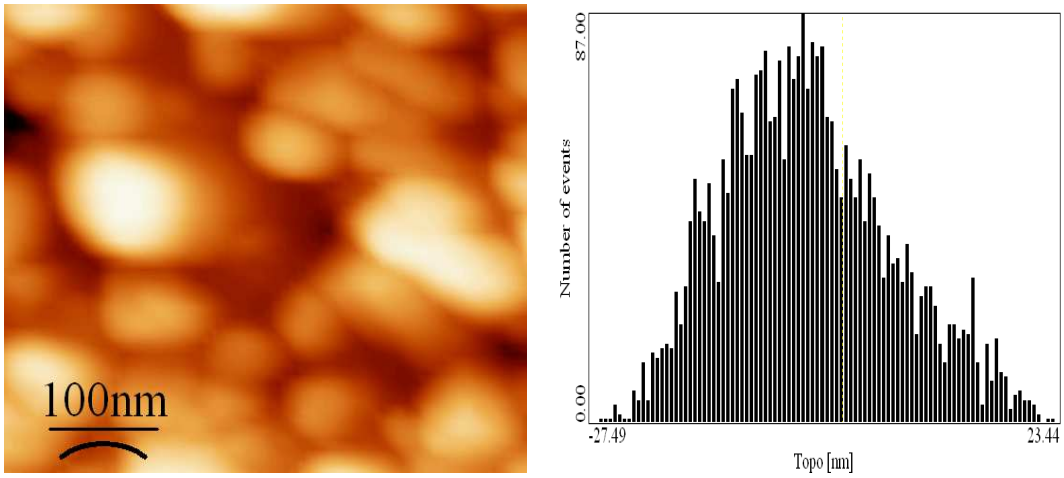

Picture 5.3: 2D AFM image and histogram for the roughness analysis of the 200nm LCMO/LAO thin film grown by the CSD technique.

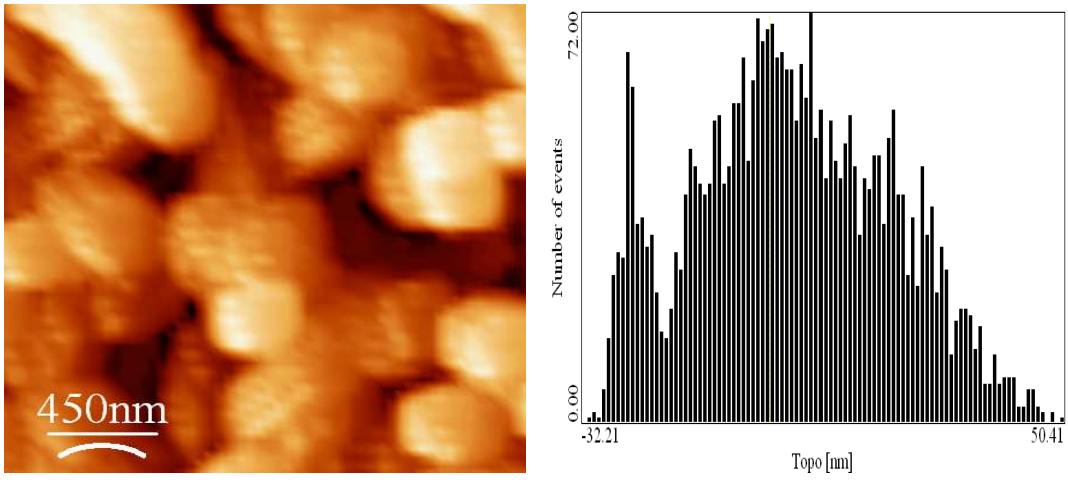

Picture 5.4: 2D AFM image and histogram for the roughness analysis of the 200nm LCMO/LAO thin film grown by the PLD technique.

5.2.2: Comparison of properties

5.2.2.(A):Electronic Transport

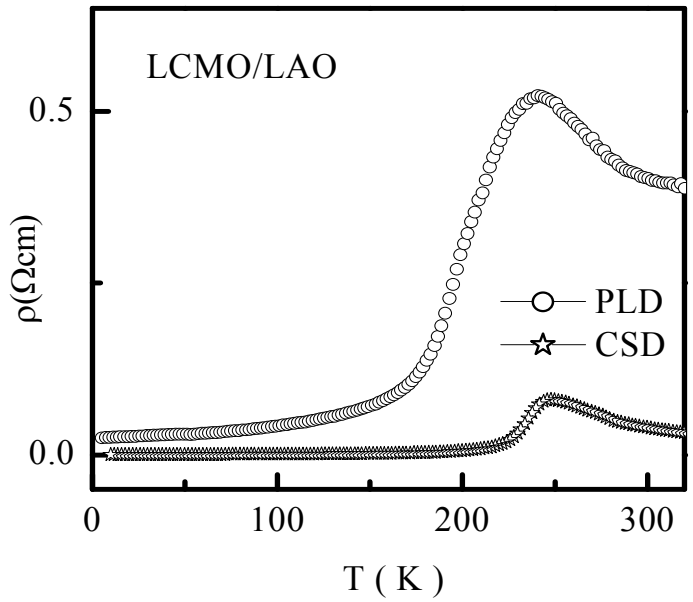

Figure 5.13: Resistivity vs. temperature plots of the 200nm LCMO/LAO thin films grown by PLD and CSD methods in 0T applied field.

Figure 5.13 shows the ρ-T plots of the PLD and CSD grown 200nm LCMO films in 0T applied field in the temperature range of 5-320K. It can be seen from the figure that, PLD and CSD grown films shows the T_{IM} ~ 239K and 249K, respectively. Both the films exhibit higher T_{IM} vales as compared to their polycrystalline bulk counterparts (T_{IM} ~ 211K) (not shown here) indicating that both the films are deposited with the optimal growth parameters. It is seen that resistivity of CSD grown film is lower than the PLD grown thin film. Resistivity of film depends principally on the factors such as substrate effect, grain boundary, grain size and growth parameter. In the present case, both the films were deposited on LAO substrate while grain size and grain boundary effects are dependent on the growth technique. To investigate further on the transport properties of both the films the ρ-T data was fitted in the magnon scattering law in the metallic region and in different VRH models in the semi-conducting region.

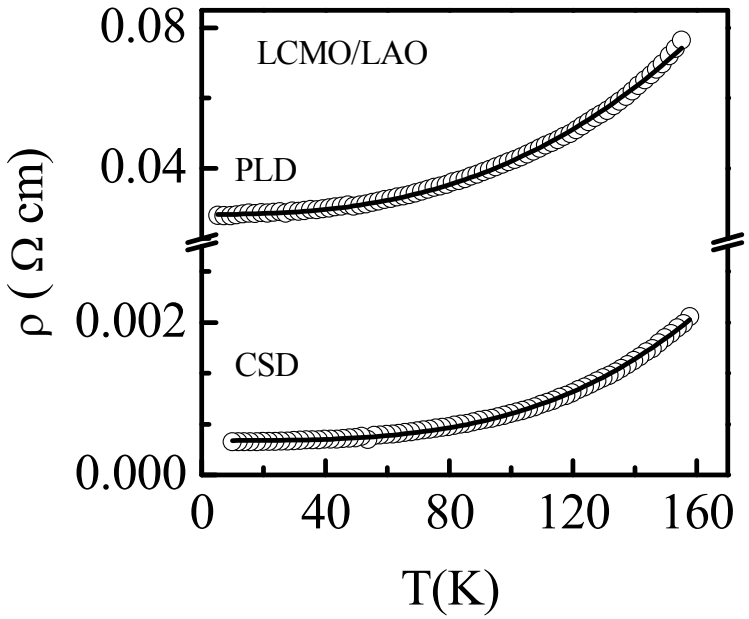

Figure 5.14: Low-temperature resistivity fits to magnon-scattering law with 0 T applied field for 200nm LCMO/LAO thin films grown by PLD and CSD methods. The symbols are the experimental data point and the solid curves are the theoretical fits.

Table 5.2: Magnetic field, coefficients of the fit to equation (1), and the normalized χ^2 for 200nm LCMO/LAO thin films grown by PLD and CSD methods.

Sample LCMO	H (T)	ρ_0 (mΩ cm)	B X10^{-9}	n	χ^2 X 10^{-9}
PLD	0	0.02690	93.29	2.6	500.9
CSD	0	0.00045	0.086	3.3	0.205

Figure 5.14 shows the curves of low temperature resistivity fits to magnon scattering law for the 200nm LCMO/LAO thin films grown the PLD and CSD methods. In metallic region, both the films obey the magnon scattering law

$$\rho(T)= \rho_0 + BT^n \ldots\ldots\ldots\ldots\ldots (1),$$

where B is electron-magnon coefficient of their corresponding scattering mechanism, ρ_0 is residual resistivity of the sample which is a contribution of various defects, domains,

grain boundaries and other temperature – independent scattering processes [26, 27]. From the fig. 5.14 and Table 5.2 it can be seen that, CSD made film has higher n value and small residual resistivity as compared to PLD grown film indicating better connectivity between grains in CSD grown films having minimal strain effect of the substrate as compared to the PLD grown film.

In CSD grown film, ρ_0 is extremely small as compared to Mott`s maximum metallic resistivity (10 mΩ), while in the PLD grown film, ρ_0 is comparatively higher than CSD grown film, which indicates towards the effect of dead layer in these films. The effect of dead layer is more pronounced in PLD grown film which is reflected in the higher resistivity values.

In the Semi conducting region we have fitted the ρ-T curves in to different VRH models with small polaron effect $\rho = AT \exp(E_a/KT)$ [Fig. 5.15 (a & c)] and $\rho = \rho_0 \exp(T_0/T)^{1/4}$ [Fig.5.15 (b & d)] [28-30]. It can be seen from the figures that, in the semi conducting region resistivity obey the small polarons hopping model (Emin-Holstein theory) while VRH model fails for the PLD and CSD grown thin films. The calculated value of activation energy (E_a) and the resistivity coefficient (B) from Emin-Holstein equation are given in the Table 5.3. In the PLD grown film, B value is higher than the CSD made film, which shows the impact of the different growth techniques. In the PLD made thin film dead layer is responsible for the higher resistivity. On the other hand activation energy is lower in the PLD grown thin film which is due to the large grain size in the PLD grown film as compared to CSD grown film.

Table 5.3: Comparison of activation energy and resistivity coefficient (B) of the 200nm LCMO/LAO thin films grown by PLD and CSD methods.

Sample LCMO	T_{IM} (K)	E_a (ev)	B ($10^{-6}\Omega$ cm /K)
PLD	239	0.0524	180
CSD	249	0.118	1.23

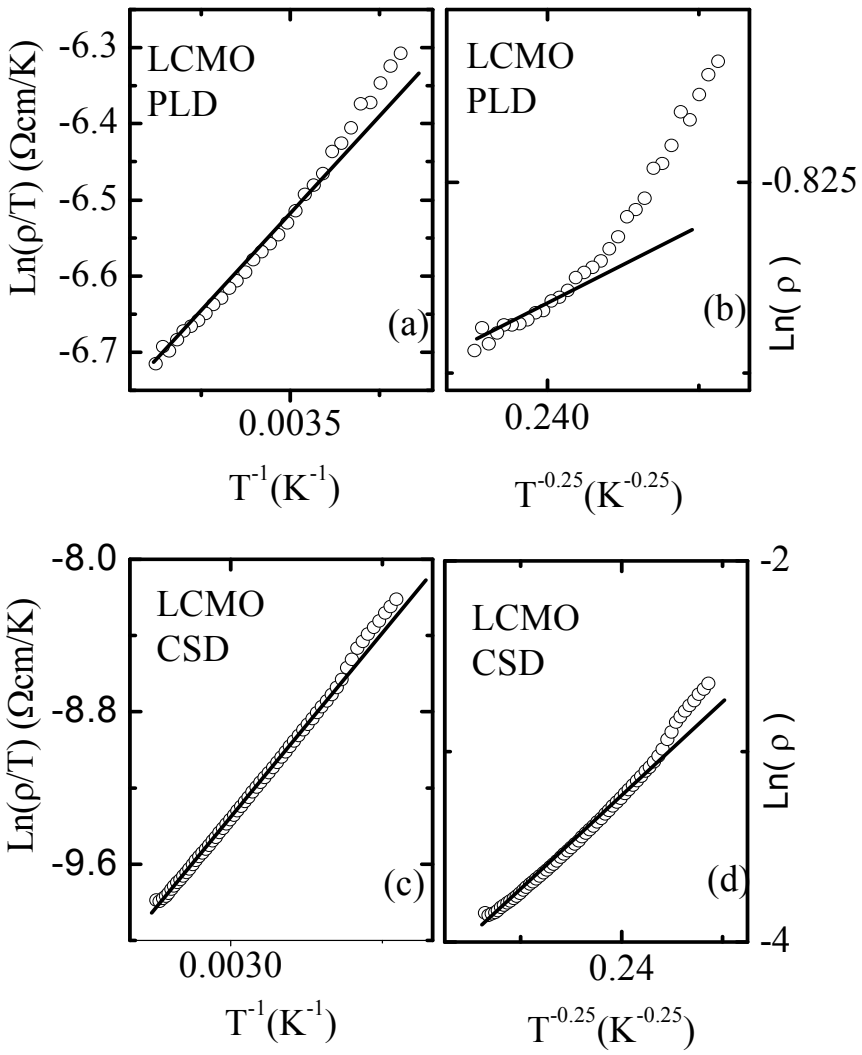

Figure 5. 15: Resistivity fits in the semi-conducting region to the plolarons hopping model (a & c) and to VRH model (b & d) for 200nm LCMO/LAO thin films grown by PLD and CSD methods. The symbols are the experimental data points and the solid curves are the theoretical fits.

Temperature dependent resistivity sensitivity of both the film has been studied by their deterring TCR values which show large disparity on positive and negative sides of Y-axis. In the CSD grown film maximum positive TCR value is ~10 % K^{-1} at 235K while in the PLD grown film has maximum TCR value is ~ 2.7 % K^{-1} at 194K. This feature is highly useful for the bolometric sensor applications.

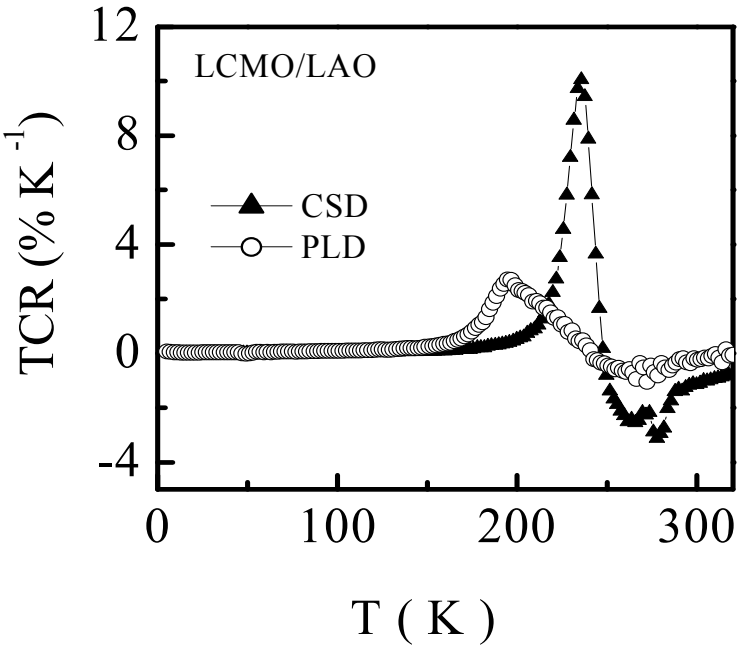

Figure 5.16: Temperature coefficient of resistance of the LCMO/LAO films grown by PLD & CSD techniques.

5.2.2.(B):Magnetotransport properties

Figure.5.17. (A) & (B) shows the MR vs. H(T) isotherms of the PLD and CSD grown LCMO films taken at different temperatures. Maximum MR ~ 90 % is observed in the PLD grown film at 200K while the CSD grown film posses maximum MR ~ 91 % at 240K (near T_{IM})

Both films have negligible low field magnetoresistance (LFMR), which indicates toward that there is no grain boundary effect and MR is due to spin fluctuations at the Mn-O-Mn bond. To observe the effect of strain on the MR behavior of these films, we have plotted the MR vs. H (T) data of 100K in fig.5.18. At 100 K, CSD grown thin film posses MR $\leq$ 3 % while the PLD grown film exhibit MR ~ 43 % which is due to magnetic anisotropy generated by the substrate in the PLD grown film. It shows that, the strain plays an important role in the modification in MR behaviour of theses film.

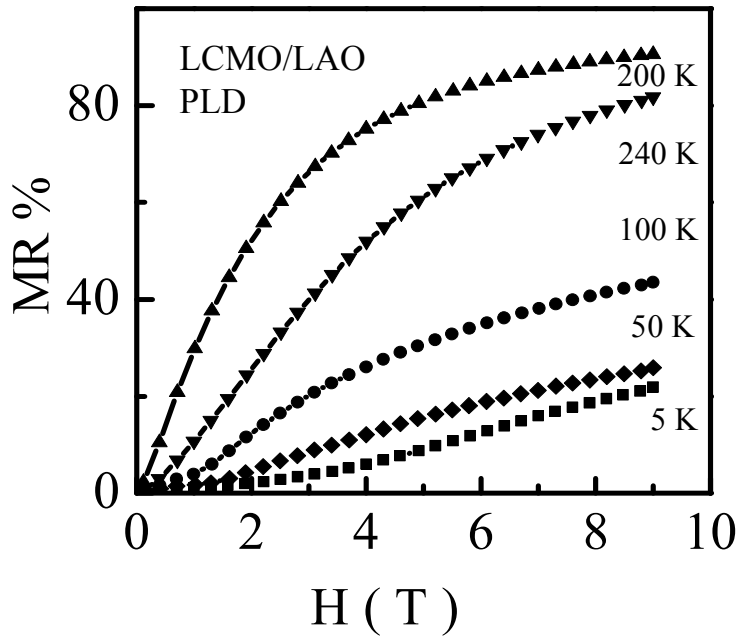

Figure 5.17.(A): MR% vs. H(T) plots for the 200nm LCMO film grown by the PLD technique at different temperatures.

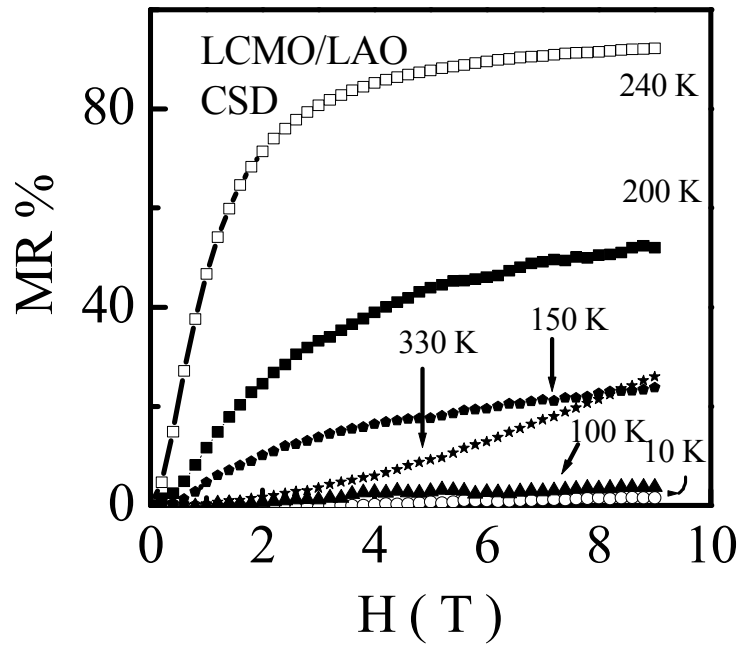

Figure 5.17.(B): MR% vs. H(T) plots for the 200nm CSD grown LCMO film.

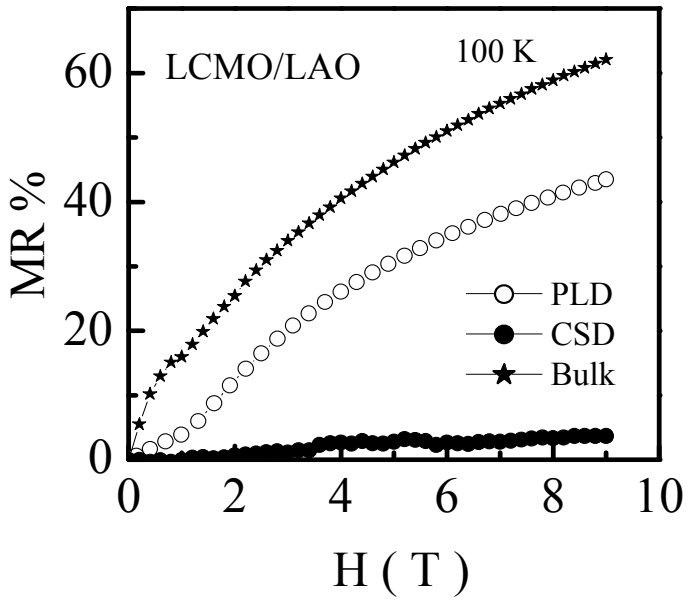

Figure 5.18 : MR % vs. H(T) plots for the bulk LCMO target and 200nm PLD and CSD grown films at 100 K.

Both the PLD and CSD grown films are epitaxial and having different grain sizes and strain effects. From XRD studies, it is seen that CSD film is almost strain free while PLD grown film has large strain due to the ablation process at the substrate.

5.2.3 Conclusions

In this part of the chapter, we have compared the physical properties of the LCMO thin films grown by PLD and CSD techniques. XRD patterns of both the films show that the films are oriented in (*hol*) direction and posses epitaxial nature. Calculated mismatch between the film and substrate shows that, CSD grown film is almost strain free as compared to PLD grown film. It is also seen that, grain size of the CSD grown film is smaller as compared to the PLD grown LCMO film which is confirmed from the AFM measurement. Also RMS roughness is larger in the PLD grown films. From the ρ-T studies it is clearly seen that, CSD grown LCMO film show the better transport properties as compared to that PLD grown film. From the fitting of the resistivity data in the insulating & FM metallic region it is seen that, activation energy is lower in PLD

grown film due to large grain size present while the residual resistivity is very less in CSD grown film which indicates better grain connectivity.

MR vs. H (T) plots show very high MR ~ 90% at temperatures close to T_{IM} in both the films. At 100K, PLD grown films exhibit large MR as compared to CSD grown films showing the effect of strain in the PLD grown film. High value of TCR in the CSD grown film shows good quality of film and its possible use in the bolometric application.

Thus, it can be concluded that the film growth technique has an appreciable effect on the physical properties of the manganite material grown on identical substrates. It is observed that, CSD grown LCMO film posses better physical properties as compared to PLD grown film.

REFRENCES

51. S. Jin, T. H. Tiefel, M. McCormack, R. A. Fastnatcht, R. Ramesh and L.H. Chen
Science **264** 413 (1994).

52. R. Von Helmolt, J. Wecker, B. Holtzapfel, L. Schultz and K. Samwer
Phys. Rev. Lett. **71** 2331 (1993).

53. A. Gary Prinz
Science **282** 1660 (1998).

54. A. Goyal, M. Rajeshwari, R. Shreekala, S. E. Lofland, S. M. Bhagat,
T. Boettcher, C. Kwon, R. Ramesh and T. Venkatesan
Appl. Phys. Lett. **71** 2535 (1997).

55. A-M Haghiri-Gosnet, J. Wolfman, B. Mercey, Ch. Simon, Ph. Lecoeur,
M. Korzenski, H. Hervieu, R Desfeur and G Baldinozzi
J. Appl. Phys. **88** 4257 (2000).

56. Mikhal Strikovski and Jr.John H. Miller
Appl. Phys.Lett.**73** 1733 (1998).

57. A. Gupta and J. Sun
J. Magn. Magn. Mater. **200** 24 (1999).

58. J-H Park, E. Vescovo, H-J Kim, C Kwon, R. Ramesh and T. Venkatesan
Phys. Rev. Lett**. 81** 1953 (1998).

59. C. Kwon, K. -C. Kim, M. C. Ronson. J. Y. Gu, M. Rajeswari, T. Venkatesan and R. Ramesh
J. Appl. Phys. **81** 4950 (1997).

60. G. Q. Gong, A. Guptha , G. Xiao, P. Lecoeur and T. R. McGuire
Phys. Rev. B **54** 3742 (1996).

61. A. Venimadhav, M. S. Hegde, V. Prasad and S. V. Subramanyam
J. Phys.D: Appl. Phys. **33** 2921 (2000).

62. D. S. Rana, K. R. Mavani, C. M. Thaker, D. G. Kuberkar, Darshan C. Kundaliya and S. K. Malik
J. of Magn. Magn. Mater. **271** 215 (2004).

63. H.-U.Habermeier
Physica B **321** 9 (2002).

64. M. Uehara, S. Mori, C. H. Chen and S. W. Cheong
Nature **399** 560 (1999).

65. N. D. Mathur, G. Burnell, S. P. Issac, T. J. Jackson, B. S. Teo, J. L. MacManus-Driscoll, L. F. Cohen, J. E. Evetts and M. G. Blamire
Nature **387** 266 (1997).

66. A. K. Raychaudhury
Adv. Phy. **44** 21 (1995).

67. L. I. Glazman and A. K. Matveev
Sov. Phys. JEPT 67, 1276 (1998).

68. F. Guinea
Phys. Rev. B **58** 9212 (1998).

69. J. G. Simmons
J. Appl. Phys. **34** 1793 (1963).

70. M. Ziese
Phys. Rev. B **68** 132411 (2003).

71. C. Chen, X. Yi, X. Zhao and B. Xiong
Sensor and Actuators, A **90** 212 (2001).

72. J. Y. Gu, K. H. Kim, T. W. Noh and K. S. J. Suh
Appl. Phys. **78** 6151 (1995).

73. J. Q. Guo, H. Takeda,N. S. Kazama, K. Fukamichi and M. J. Tachiki
Appl. Phys. **81** 7445 (1995).

24. J. Li, J. H. Liu, H. P. Li, H. C. Fang and C. K. Ong
J. Magn, Magan, Mater. **202** 285 (1999).

25. G. C. Xiong , Q. Li, H. L. Ju, S. M. Bhagat, S. E. Lofland, R. L. Greene and T. Venkatesan
Appl. Phys. Lett **67** 3031 (1995).

26. M. Koubaa, A-M. Haghiri-Gosnet, R. Desfeux, P. H. Lecoeur, W. Prellier and B. Mercey
J. Appl. Phys. **93** 5227 (2003).

27. A. E. Berkowitz, J. R. Mitchell, M. J. Carey, A. P.Young, S. Zhang, F. E. Spada, F. T. Parker, A. Hutten and G.Thomas
Phys. Rev. Lett. **68** 3745 (1992)

28. D. Emin and T. Holstein
Phys. Rev. B **58** 11519 (1998).

29. J. M. D. Coey, M. Viret, L. Ramo and K. Ounadiela
Phys. Rev. Lett. **75** 3910 (1995).

30. M. Viret, L.Ranno and J. M.D. Coey
J. Appl. Phys. **81** 4964 (1997).

SCOPE OF FUTUTE RESEARCH ON MANGANITES

There are several questions and issues on pertaining to the studies on mixed valent manganites which needs further attention of the condensed matter physicists. To list few of them

- The evidence of charge ordering in the half-doped manganites having nanoclusters above T_C should be confirmed.
- X-ray and Neutron scattering studies, on the $(LaPr)_{1-x}Ca_xMnO_3$ mixed valent manganite system, are needed to be performed in order to understand the charge-ordered nano-clusters.
- The presence of glassy state in some manganites similar to standard spin glass behaviour has to be explored in detail and whether phase separation phenomenon is responsible for such a behavior has been studied.
- There is need of understanding the cause for low temperature minima in resistivity of few manganites.
- Various thin films and multilayered structures of manganites should be grown and tested for field and temperature sensing applications at room temperature under low applied fields.
- From the technological point of view, many important issues are still unexplored such as, the phase diagram in 3D of two orbitals model may lead to several interesting surprises such as presence of stripe phases, the percolative charge transport, competition between different spin ordering phases etc.
- On application side, it is necessary to develop new manganite based heterostructured devices suitable for the application in read heads, non-volatile MRAM, magnetic tunneling junction (MJT) having better advantage than the conventional devices.

List of Publications in International/National Journals

1. Resistivity minimum at low temperature in the manganite compound $(La_{0.5}Pr_{0.2})Ba_{0.3}MnO_3$

   J. H. Markna, D. S. Rana, R. N. Parmar, C. M. Thaker, , J. A. Bhalodia, D. G. Kuberkar, P. Raychaudhuri, J. John and S. K. Malik
   Solid State Physics (India), 49, 824 (2004).

2. Low Temperature Neutron Diffraction Studies on Superconductors of the type $La_{2-x}Dy_xCa_{2x}Ba_2Cu_{4+2x}O_z$
   Rohini N. Parmar, **J. H. Markna**, D. S. Rana, C.M.Thakar, N.A.Shah, S. Rayaprol, D. G. Kuberkar, Keka R. Chakraborty, P. S. R. Krishna and M. Ramnadham

   Solid State Physics (India), 49, 822 (2004).

3. Low temperature transport anomaly in the magnetoresistive compound $(La_{0.5}Pr_{0.2})Ba_{0.3}MnO_3$
   D. S. Rana, **J. H. Markna**, R. N. Parmar, D. G. Kuberkar, P. Raychaudhuri, J. John and S. K. Malik
   Phys. Rev. B, 71, 212404 (2005).

4. Electronic transport and magnetism in $(La_{0.7-2x}Eu_x)(Ca_{0.3}Sr_x)MnO_3$ compounds
   D. S. Rana, C. M. Thaker, K. R. Mavani, **J.H. Markna**, R. N. Parmar, N.A.Shah, D. G. Kuberkar and S.K. Malik
   Hyperfine Interactions, 10, 1007 (2005).

5. Growth-parameter-dependent magnetoresistance in pulsed-laser-deposited $(La_{0.5}Pr_{0.2})Ba_{0.3}MnO_3$ thin films
   K. R. Mavani, D. S. Rana, **J. H. Markna**, R. N. Parmar, and D. G. Kuberkar P. Misra, L. M. Kukreja, D. C. Kundaliya and S. K. Malik
   J. Appl. Phys. 98, 086111 (2005).

6. ***I-V studies on $La_{0.7}(Ca/Sr)_{0.3}MnO_3$ manganite thin films grown by Chemical Solution Deposition (CSD) method***
   P. S. Vachhani, R. N. Parmar**,** P. S. Solanki, J. Raval, **J. H. Markna**, N. A. Shah, J. A. Bhalodia, D. S. Rana† and D.G.Kuberkar
   Solid State Physics (India), 50, 517 (2005).

7. Low Temperature Bond Valence Sum study of $La_{1.7}Dy_{0.3}Ca_{0.6}Ba_2Cu_{4.6}O_z$ oxide superconductors
R. N. Parmar**, J. H. Markana**, C. M. Thakar, S. Rayaprol, J.A.Bhalodia, N.A. Shah, D. G. Kuberkar, Keka R. Chakraborty, P. S. R. Krishna and M. Ramnadham
Solid State Phenomena, 111, 163 (2006).

8. Thickness dependent Shift Heavy Ion Irradiation effect on Electronic Transport of $(La_{0.5}Pr_{0.2})Ba_{0.3}MnO_3$ Thin Films
J. H. Markna, R. N. Parmar,D. G. Kuberkar, Ravi Kumar, D. S. Rana and S. K. Malik
Appl. Phys. Lett. 88, 152503 (2006).

9. Swift heavy ion irradiation induced enhancement in resistivity of $La_{0.7}Ba_{0.3}MnO_3$ thin films synthesized by chemical solution deposition
R. N. Parmar**, J. H. Markana**, D. S. Rana, Vivas G. Bagve, D. G. Kuberkar, Ravi Kumar and S. K. Malik
Appl. Phys. Lett. 89, 202506 (2006).

10. Effects of Swift Heavy Ions Irradiation on Epitaxial $La_{0.5}Pr_{0.2}Sr_{0.3}MnO_3$ Thin Films grown by Pulsed Laser Deposition
J. H. Markna, R. N. Parmar, D. G. Kuberkar, Ravi Kumar, P. Misra, L. M. Kukreja, D. S. Rana and S.K. Malik
NIMB B 2006 (Under revision).

11. Enhancement in TCR of $La_{0.5}Pr_{0.2}Ba_{0.3}MnO_3$ manganite thin film by Swift heavy ion irradiation
P.S. Vachhani, R.R. Doshi, R.N. Parmar, **J.H. Markna**, J.A. Bhalodia, Ravi Kumar and D.G. Kuberkar
Solid State Physics (India), accepted (2006).

12. Grain size dependent transport and magnetoresistance behavior of CSD grown nanostructured $La_{0.7}Sr_{0.3}MnO_3$ manganite films
R. N. Parmar**, J. H. Markna**, P. S. Solanki, P. S. Vachhani and D. G. Kuberkar
Communicated to J. Nanoscience & Nanotechnology (2006).

13. Strain induced non-linear conduction in epitaxial $La_{0.7}A_{0.3}MnO_3$ manganite thin films
P. S. Vachhani, P. S. Solanki, **J. H. Markna**, R. N. Parmar, J. A. Bhalodia and D. G. Kuberkar
Communicated to Indian Journal of Engineering and Materials Science 2006.

14. Role of structural displacements in $La_{2-x}Dy_XCa_{2x}Ba_2Cu_{4+2x}O_z$ (x = 0.3, 0.5) Superconductor: A temperature dependent Neutron Diffraction study
R. N. Parmar**, J. H. Markana**, S. Rayaprol, D. G. Kuberkar, Keka R. Chakraborty, P. S. R. Krishna and M. Ramnadham
To be communicated.

15. Electronic transport and magnetotransport properties of LPSMO/Al_2O_3/LPSMO Multilayer
J. H. Markna, P. S. Vachhani, R. N. Parmar, D. G. Kuberkar, Ravi Kumar, P. Misra, L. M. Kukreja, D. S. Rana and S.K. Malik
To be communicated.

16. Effect of Structural Disorder on Electrical and Magnetotransport of $La_{0.5}Pr_{0.2}R_{0.3}MnO_3$ (R = Sr, Ba) Manganites Thin Films
J. H. Markna, R. N. Parmar, D. G. Kuberkar, P. Misra,L. M. Kukreja, K. R. Mavani, D. S. Rana and S. K. Malik
To be Communicated.

17. Strain induced modification in the properties of CSD and PLD grown LCMO manganite thin film: comparative study
J. H. Markna, R. N. Parmar, R. R. Doshi, J. A. Bhalodia and D. G. Kuberkar,
J. of Surface Science (Submitted).

18. Electronic transport and magnetoresistance of the Pulsed Laser Deposited epitaxial thin films of half-metallic $La_{0.5}Pr_{0.2}Sr_{0.3}MnO_3$ manganite
J. H. Markna, R. N. Parmar, D. G. Kuberkar, P. Misra, L. M. Kukreja, D. S. Rana and S.K. Malik
To be Communicated.

List of Publications in International/National/Conferences/Symposia/Workshop

POSTER PRESENTATIONS

1. "Electrical and magnetotransport properties of LPD grown manganite thin films"
   J. H. Markna, D. S. Rana, K. R. Mavani, S. K. Malik, R. N. Parmar, D. G. Kuberkar, P. Misra and L. M. Kukreja

   "3rd Gujarat Congress Research Student Meet" (GCRSM held at Vallabhvidhyanagar. January 1st, 2004.

2. "Superconductivity in new La-based mixed oxide compound"
   R. N. Parmar, S. Rayprol, K. R. Mavni, J. John, R. Pinto, D. S. Rana, C. M. Thaker, **J. H. Markna**, D. G. Kuberkar, Keka R. Chakraborty, P. S. R. Krishna and M. Ramanadham

   ***"3rd Gujarat Congress Research Student Meet"* (GCRSM) held at Vallabhvidhyanagar. January 1st, 2004.**

3. "Magnetism and magnetoresistance in $(La_{0.7-2x}Eu_x)(Ca_{0.3}Sr_x)MnO_3$; $0.005 \leq x \leq 0.25$ compounds"
   D. S. Rana, C. M. Thaker, K. R. Mavani, **J. H. Markna,** R. N. Parmar, D. G. Kuberkar M. Stone, P. Schiffer and S.K. Malik
   "*International Workshop on Nanomaterials & Magnetic Semiconductors*" (IWNMS) organized by M.S. University, Baroda. February 8-14, 2004.

4. "Effect of size disorder on the electronic transport and magnetic properties in $(La_{0.5}Pr_{0.2})(Ca_{0.3-x}Ba_x)MnO_3$; $0.00 \leq x \leq 0.3(0.1)$ compounds"
   C. M. Thaker, D. S. Rana, K. R. Mavani, **J. H. Markna**, R. N. Parmar, N. A. Shah, D. G. Kuberkar Darshan C. Kundaliya and S.K. Malik
   "*International Workshop on Nanomaterials & Magnetic Semiconductors*" (IWNMS) organized by M.S. University, Baroda. February 8-14, 2004.

5. "***Resistivity minimum at low temperature in manganite compound $La_{0.5}Pr_{0.2}Ba_{0.3}MnO_3$"***
   J. H. Markna, D. S. Rana, R. N. Parmar, C. M. Thaker, J. A. Bhalodia, D. G. Kuberkar P. Raychaudhuri, J. John and S.K. Malik
   "*DAE Solid State Physics Symposia-2004*" organized by Department of Atomic Energy, BARC, Mumbai at Amritsar. December 26 - 30, 2004.

6. "Low temperature neutron diffraction studies on superconductors of the type $La_{2-x}Dy_xCa_{2x}Ba_2Cu_{4+2x}O_z$"
Rohini Parmar, **J. H. Markna**, D.S. Rana, C.M. Thakar, D. G. Kuberkar, N. A. Shah, S. Rayaprol, Keka R. Chakraborty, P.S.R.Krishna and M.Ramnadham
"*DAE Solid State Physics Symposia-2004*" organized by Department of Atomic Energy, BARC, Mumbai at Amritsar. December 26 - 30, 2004.

7. "Effect of SHI irradiation on low temperature resistivity of LPBMO manganite thin films"
J. H. Markna, C. M. Thaker, D. S. Rana, R. N. Parmar, J. A. Bhalodia D. G. Kuberkar**,** P. Raychaudhuri, J. John, N. A. Kulkarni, R. J. Chaoudhary, Ravi Kumar and S. K. Malik
"International INDOJERMAN Workshop on Synthesis and Modification of Nano-Structured Materials by Energetic Ions Beams", New Delhi, Feb 2005.

8. "Anomaly in the transport properties in the irradiated $La_{0.5}Pr_{0.2}Sr_{0.3}MnO_3$ epitaxial thin film"
J. H. Markna, R. N. Parmar, R. R. Doshi, C. M. Thaker, J. A. Bhalodia D. G. Kuberkar, P. Misra, L. M. Kukreja, D. S. Rana and S.K. Malik
"*DAE Solid State Physics Symposia-2005*" organized by Department of Atomic Energy, Mumbai at Department of Atomic Energy, BARC, Mumbai.

9. "I-V studies on $La_{0.7}(Ca/Sr)_{0.3}MnO_3$ manganite thin films grown by Chemical Solution Deposition (CSD) method"
P. S. Vachhani, R. N. Parmar, P. S. Solanki, J. Raval, **J. H. Markna**, N. A. Shah, J. A. Bhalodia, D. S. Rana† and D.G. Kuberkar
"*DAE Solid State Physics Symposia-2005*" organized by Department of Atomic Energy, Mumbai at Department of Atomic Energy, BARC, Mumbai.

10. "Studies on $La_{0.5}Pr_{0.2}Sr_{0.3}MnO_3$ epitaxial thin films: an application point of view"
J. H. Markna, R. N. Parmar, P. S. Vachhani, C. M. Thaker, J. A. Bhalodia, D. G. Kuberkar, P. Misra, L. M. Kukreja, D. S. Rana and S. K. Malik
DAE-BRNS 3rd National Symposium on "*Pulsed Laser Deposition of Thin Films and Nano-structured materials PLD-2005*", Tirupati. October 7-9, 2005.

ORAL PRESENTATIONS

1."**Current Trends in Materials Research**" organized under UGC - SAP program at Department of Physics, Saurashtra University, Rajkot. February 28, 2005.

2."**National Workshop on Thin film Technologies & Applications**" (NAWOTTA)
organized by PSG arts & Science College association with MRSI, at Coimbatore. July 9-12, 2004.

PARTICIPATED

1.**"All India Refresher Course in Experimental Physics"** organized by Indian Academy of Science (IAS), Bangalore in association with Department of Physics, Saurashtra University, Rajkot, November 03-15, 2003.

2. **" School on Ion Beams in Materials Sciences"**
Institute of Physics (IOP), Bhubeneswar, October 4-9, 2004.

3. **"National Workshops on Advanced Methods for Materials Characterization"** (NWMS) organized by Materials Research Society of India (MRSI) at BARC., Trombay, Mumbai, October 11 - 15, 2004.